

論文 / 著書情報  
Article / Book Information

題目(和文)	
Title(English)	Study of Functional-Circuit Integration to Waveguide Slot Array Antennas in the Millimeter-Wave Band
著者(和文)	Xin XU
Author(English)	Xin XU
出典(和文)	学位:博士(学術), 学位授与機関:東京工業大学, 報告番号:甲第10677号, 授与年月日:2017年9月20日, 学位の種別:課程博士, 審査員:廣川 二郎,水本 哲弥,阪口 啓,西方 敦博,庄司 雄哉,小西 善彦
Citation(English)	Degree:Doctor (Academic), Conferring organization: Tokyo Institute of Technology, Report number:甲第10677号, Conferred date:2017/9/20, Degree Type:Course doctor, Examiner:,,,,,
学位種別(和文)	博士論文
Type(English)	Doctoral Thesis

Doctoral Dissertation

**Study of Functional-Circuit  
Integration to Waveguide  
Slot Array Antennas  
in the Millimeter-Wave Band**

September, 2017

Under the Supervision of

**Professor Jiro Hirokawa**

Presented by

**Xin Xu**

Department of Electrical and Electronic Engineering

Tokyo Institute of Technology

# Acknowledgements

*No man is an island.*

John Donne

I owe much gratitude to Prof. Jiro Hirokawa and Prof. Makoto Ando for their support, encouragement, guidance, supervision and unfailing professionalism in the face of every aspect throughout my Ph.D. study. It is a privilege to have known and worked with them, and I thank them for seeing me through to the end.

I also thank my dissertation committee, Prof. Tetsuya Mizumoto, Prof. Kei Sakaguchi, Prof. Nishikata Atsuhiko, Prof. Yuya Shoji and Prof. Yoshihiko Konoshi. Many thanks for their instructive suggestions and comments, which have greatly improved the quality of this dissertation.

I would like to thank the former and current lab members, particularly to Prof. Kimio Sakurai, Mrs. Keiko Nagao and Mr. Kim Donghun, for their countless help and assistance. Being as a colleague with all of you is really a pleasure for me.

I am grateful to Prof. Kiyomichi Araki, Prof. Kenichi Okada, Prof. Fumio Watanabe, Prof. Yasutake Hirachi and other scholars/researchers, who have provided helpful advice to me.

I am indebted to Prof. Angelo Freni and Dr. Agnese Mazzinghi from University of Florence, Italy, for being the best host during my three-month research visit in their group, and also for their continuous guidance. I also thank Dr. Nicola Bartolomei and Mr. Riccardo Ozzola for all the unforgettable moments we have shared together, and I hope our friendship never ends.

Distance couldn't stop my family from loving and guiding me, always keeping me in their thoughts and prayers. I thank for their generously and

genuinely supplied patience, encouragement, love, and never-ending support through what often seemed like a never-ending process in my life.

A lot of work is solitary during the Ph.D. study, but I was never alone. Thank you all so much, I would never made it this far without you.



# Contents

<b>Chapter 1 Introduction .....</b>	<b>1</b>
1.1 Millimeter-Wave Wireless Communication.....	1
1.2 Waveguide Slot Array Antennas in the Millimeter-Wave Band.....	2
1.3 Objective of this Thesis.....	5
1.4 Outline of this Thesis .....	8
References.....	10
Figures and Tables.....	16
<b>Chapter 2 Seamless Integration of Filtering Functionalities .....</b>	<b>20</b>
2.1 Introductory Remarks .....	20
2.2 Design and Characterization of the Filters .....	21
2.2.1 The Cavity Resonator .....	21
2.2.2 Design of the Bandpass Filter.....	24
2.2.3 Design of the Bandstop Filter .....	26
2.3 Integration of Filters into a $16 \times 16$ -Element Slot Array Antenna.....	31
2.3.1 Integration Strategy.....	31
2.3.2 Fabrication and Experiments .....	34
2.4 Concluding Remarks .....	37
References.....	38
Figures and Tables.....	40
<b>Chapter 3 Incorporation of Monopulse Processing Capability .....</b>	<b>57</b>
3.1 Introductory Remarks .....	57
3.2 Antenna Configuration and Operation Mechanism .....	57
3.3 Design of the Building Blocks .....	59
3.3.1 Radiating Element.....	59
3.3.2 Corporate-Feed Circuit .....	60
3.3.3 Comparator.....	61
3.4 Antenna Implementation and Simulated Results .....	64
3.5 Experimental Results .....	65
3.5.1 Reflection and Isolation .....	66
3.5.2 Realized Gain, Directivity, and Loss Evaluation .....	66
3.5.3 Radiation Pattern .....	67
3.6 Concluding Remarks .....	69
References.....	70

<b>Figures and Tables</b> .....	71
<b>Chapter 4 Simultaneous Generation of Multiple OAM-Modes</b> .....	89
<b>4.1 Introductory Remarks</b> .....	89
<b>4.2 Antenna Structure and Operation Mechanism</b> .....	89
<b>4.3 Antenna Design</b> .....	90
<b>4.3.1 OAM Beam-Switching Circuit</b> .....	90
<b>4.3.2 Feeding Circuit for RLSA</b> .....	91
<b>4.3.3 RLSA</b> .....	93
<b>4.4 Simulated Results</b> .....	97
<b>4.4.1 Reflection and Isolation</b> .....	97
<b>4.4.2 Directivity and Cross-polarization of Port 1</b> .....	98
<b>4.4.3 Field Distribution</b> .....	98
<b>4.5 Concluding Remarks</b> .....	98
<b>References</b> .....	100
<b>Figures and Tables</b> .....	101
<b>Chapter 5 Conclusions</b> .....	117
<b>5.1 Summary of Preceding Chapters</b> .....	117
<b>5.2 Future Prospects</b> .....	119
<b>List of Publications</b> .....	121
1. <b>Journal Papers</b> .....	121
2. <b>International Conferences</b> .....	121
3. <b>Technical Reports on Antennas and Propagation, IEICE Japan</b> .....	122
4. <b>National Convention Records of IEICE Japan</b> .....	122

# Chapter 1 Introduction

## 1.1 Millimeter-Wave Wireless Communication

Currently, the conventional microwave band below 10 GHz has been heavily utilized and is going to reach its saturation point because of the ever-growing demand of booming wireless applications that require gigabit per second (Gbps) and higher data speeds [1.1–6].

Millimeter wave generally corresponds to the radio spectrum between 30 to 300 GHz. Compared to bandwidth-limited lower microwave frequency band, the millimeter-wave band is well known to hold diverse advantages and unique features in wireless communications, just list a few of them:

(1) The radio spectrum in millimeter-wave band is rather undeveloped and larger bandwidths are still available.

(2) The availability of large bandwidths in millimeter-wave band can enhance the spatial resolution as well as the data speed.

(3) The atmospheric attenuation and scattering associated with various kinds of molecular effects in millimeter-wave band can make the re-use of the frequency spectrum more efficient especially in short communication distances.

(4) The limited communication range and the narrow beam widths in millimeter-wave band can enhance the security and privacy.

(5) The system size is greatly reduced in millimeter-wave band so that the systems with complicated physical architectures can be implementable using advanced packaging technique.

In academia and industry, recent strong enthusiasms in high data-rate wireless transmission links and high capacity communication systems have greatly stimulated the research in millimeter-wave techniques in the area such as fixed access, machine-to-machine interconnectivity, collision

avoidance, imaging systems, 5G communication and so on [1.7–13].

In many countries the V-band (57–66-GHz band) and E-band (71–76- and 81–86-GHz bands) have been allocated for the purpose of Gbps wireless services in the public domain [1.14, 15].

Due to the high atmospheric oxygen absorption in 60-GHz band (about 15 dB/km at 60 GHz), the V-band is suitable for short-range point-to-point and point-to-multipoint applications such as indoor wireless local area network (LAN), wireless personal area network (WPAN), gigabit access transponder equipment (GATE) and so on. Different from the V-band, the atmospheric oxygen absorption above 70 GHz drops significantly to less than 1 dB/km and rises again after 100 GHz due to the molecular effects. This phenomenon makes the E-band very suitable for long-distance wireless communication with robust weather resilience and fewer interference concerns over several miles.

## **1.2 Waveguide Slot Array Antennas in the Millimeter-Wave Band**

Array antennas are critical components in the successful development of millimeter-wave systems, especially in the case of point-to-point communications. This is mainly due to the concerns in terms of the noise performance and the power budget of systems [1.16, 17]. The noise characteristics of systems are mainly determined by the first building blocks, which are closely related to the antenna loss. The power budget of the system can be tuned by the gain of antenna.

The choice of an appropriate transmission line is a fundamental issue when determining antenna loss and efficiency. The array antenna based on traditional transmission lines such as microstrip and triplate lines generally suffer from remarkable radiation losses. This problem becomes more notable

for high-gain applications in the millimeter-wave band. For example, in 60-GHz band, the efficiency of microstrip or triplate line array antennas with 35-dBi gain is roughly estimated to be lower than 30% [1.18].

Waveguide has the potential in terms of low loss and slimness, and the waveguide slot array antennas are leading candidates for millimeter-wave high-gain applications. In the last decades, various kinds of highly-efficient and mass-producible waveguide slot array antennas in the millimeter-wave band have been pioneered at Tokyo Institute of Technology (Tokyo Tech.) [1.19–30].

Fig. 1.1 shows the structures of five types of millimeter-wave waveguide slot array antennas developed at Tokyo Tech.:

- (1) Co-phase-feed single-mode waveguide slot array antenna.
- (2) Alternating-phase-feed single-mode waveguide slot array antenna.
- (3) Radial line slot antenna (RLSA).
- (4) Post-wall waveguide slot array antenna.
- (5) Plate-laminated hollow-waveguide slot array antenna.

A single-mode waveguide slot array antenna consists of only two components, i.e. a slotted plate and a base plate. In the co-phase-feed case, the electrical contact between the narrow walls on the bottom plate and the slotted plate should be perfect. Contrarily, in the alternating-phase-feed case, the aforementioned electrical contact is not necessary, resulting in the loss and cost reductions. It is reported that a 35.9-dBi realized gain with a 75.6% antenna efficiency at 22.15 GHz [1.21], and a 34.8-dBi realized gain with a 57.0% antenna efficiency at 76.5 GHz can be achieved. The main issues in such kind of antenna are the mass productivity and the bandwidth.

A RLSA antenna is based on a parallel-plate oversized-waveguide with a TEM-wave operation. It dispenses with side-wall to reduce the transmission loss. The feeding circuits can be coaxial cable or standard waveguide. It has been commercially mass-produced for 12-GHz direct-

broadcast satellite (DBS) reception in Japan [1.19]. In millimeter-wave band, it is reported that a 32-dBi realized gain with a 52% antenna efficiency in 60-GHz band can be achieved [1.24].

A post-wall waveguide slot array antenna is fabricated using a grounded dielectric substrate where the densely arrayed metalized via-holes are drilled in order to replace the conducting narrow walls. It can be fabricated using the commercially available print circuit board (PCB) technique at a low cost [1.23]. To broaden the antenna bandwidth by eliminating the long-line effect, multi-layered PCB [1.31] and low-temperature co-fired ceramics (LTCC) [1.32] fabrication techniques have been used to realize the corporate-feed circuit. However, the dielectric loss in high-gain millimeter-wave applications is still troublesome [1.33].

A plate-laminated hollow-waveguide slot array antenna features high efficiency, high gain and wideband operation in the millimeter-wave and the sub-millimeter bands. It is fabricated by a unique technique called diffusion bonding of laminated thin metal plates. It is a commercially available fabrication technique which allows dispensing with additional tuning and assembly processes after the bonding. It has advantageous features such as high accuracy, re-productibility, reliability, and suitability for mass-production and could provide waveguide fabrication and packaging solutions for millimeter-wave and sub-millimeter-wave applications. The surface roughness and the electrical contact among the plates in fabrication can be very good. It is reported that a 32.9-dBi realized gain with an 86.6% antenna efficiency at 78.5 GHz [1.28], a 38-dBi realized gain with an antenna efficiency over 60% in 120-GHz band [1.29] can be achieved. Further, a constant antenna efficiency is achieved over a broad bandwidth.

### 1.3 Objective of this Thesis

To cope with the various kinds of booming millimeter-wave wireless applications, this study makes efforts on the functional-circuit integration to waveguide slot array antennas in the millimeter-wave band.

*(1) Integration of filtering functionalities for E-band point-to-point communication applications.*

In 71–86-GHz band, a variety of services, including fixed-satellite, mobile-satellite, broadcasting-satellite, radio astronomy, amateur radio, vehicle radars and so on are allocated on a primary basis in portions of the bands below 71 GHz, between 76–81 GHz, and above 86 GHz [1.34]. These possible instances of harmful interference to E-band application should be prevented and minimized by means of filtering-functionality integration.

Fig. 1.2 shows an integration scenario where the antenna array and the filtering circuit are interconnected in a straightforward way [1.35]. Such integration increases size, cost and system complexity, as well as it deteriorates the system performance including the efficiency.

Fig. 1.3 shows another integration scenario where the radiation and the filtering functionalities are co-synthesized [1.36]. However, such technique is not applicable for the case in [1.28]. This is because the radiating elements in [1.28] are fully corporate-feed and work well over the entire 71–86-GHz band. An elimination of the detuning of the radiating elements can preserve the radiation characteristics.

Therefore, high performance E-band filters which also hold compatible geometrical features should be developed with an optimal integration scenario with the array antenna.

*(2) Incorporation of monopulse processing capability for E-band monopulse tracking applications.*

Monopulse is an established technique capable of processing fast and accurate solutions to determine electronically the direction of arrival of echoes and target locations with precise angle estimates in radar systems [1.37, 38]. For an ultra-high range-resolution, much more bandwidth, commonly 20% larger is required [1.39, 40]. The demand of this larger bandwidth has traditionally been delivered with lower frequency bands such as the ultra-wideband channel (3.1–10.6 GHz), the Ka-band (22–29 GHz), and others. However, serious issues arise in the usage of these very crowded and heavily-utilized lower frequency bands due to the harmful interference from co-existing in- or adjacent-bands, as well as the low data throughput with maximum data rates of only hundreds of Mbps. Traditional monopulse array antennas have narrow operation bandwidth of a few percent only. Also, the antenna efficiency and the null depth are not so good because of the difficulty in multi-layer hollow-waveguide fabrication. By far, no waveguide antenna solution can be found in the open literature for millimeter-wave ultra-wideband monopulse tracking applications, where a bandwidth of larger than 20% is required.

Fig. 1.4 shows two typical monopulse array antennas in the literature [1.42, 43]. The feeding network and comparator are key components in determining the bandwidth of antenna monopulse capability. A corporate-feed network [1.42, 47] is devoted to wideband operation as long-line effects [1.41, 43–46] can be fully eliminated so that each radiating unit can be fed uniformly regardless of the frequency. In comparison to a single-layer counter-part implemented by a 3-dB coupler associated with a  $90^\circ$  phase shifter [1.41–44], a comparator implemented by  $180^\circ$  hybrids [1.45–47] can maintain a better amplitude/phase balance in a wider bandwidth. In [1.42], the corporate-feed architecture is adopted, but the phase/amplitude deviation of the comparator will still limit the bandwidth of monopulse capability.

The waveguide structure has the potential to offer low loss and



slimness and is the leading candidate for millimeter-wave applications. Use of multi-layer waveguide architecture is indispensable to realize a 180° hybrid and the corporate-feed network associated with radiating elements above it, and it also enables a compact size with reduced transmission losses in the interconnection between the comparator and the feeding circuit. However, fabricating and manufacturing these complicated and sophisticated three-dimensional components in the millimeter-wave band using traditional machining is prohibitively expensive and time-consuming. Additionally, a reliable and re-producible assembly of the components into a final mass-produced product at a competitive cost is still a challenge as the electrical performance in the millimeter-wave band is highly sensitive to the assembly quality. A bulky profile after assembly also poses considerable disadvantages in integration into a compact front-end sub-system.

Therefore, a design strategy of waveguide slot array antenna associated with a low-cost and mass-productive fabrication technique should be proposed for millimeter-wave ultra-wideband monopulse tracking applications.

*(3) Simultaneous generation of multiple orbital angular momentum (OAM) modes for V-band OAM-multiplexing applications.*

By adopting large array antennas, 60 GHz-band gigabit wireless access systems, which operate in the radiating near-field region have been successfully demonstrated [1.30]. An electromagnetic wave carries an angular momentum that can be decomposed in spin angular momentum (SAM) and OAM. The former is linked to the polarization, while the latter is linked to the helical transverse phase structure  $\exp(il\varphi)$  of the wave, where  $\varphi$  is the transverse azimuthal angle and  $l$  is an unbounded integer, that indicates the OAM-mode state. Theoretically infinite OAM modes, orthogonal with each other, can propagate in an unbounded medium. This property has

driven the recent advances in ultra-high capacity communication systems and stimulated the research in data-transmission links using OAM multiplexing [1.48]. Due to the beam divergence, currently the OAM modes are mainly interested for short-range applications.

Fig. 1.5 shows the structure of a typical array antenna structure for OAM applications, where all the radiating elements are arranged on a circle [1.49]. Progressive phase is applied on the adjacent radiating elements. However, it is not practical for high-gain applications because the feeding circuit would be extremely complicated.

Therefore, a light, low-cost and flat panel array antenna solution which can simultaneously launch multiple OAM-modes through a single aperture, should be proposed. In addition, when the antenna size is fixed, the investigation on the enhancement of transmission distance in OAM multiplexing should also be carried out.

## 1.4 Outline of this Thesis

Fig. 1.6 shows the flowchart of this thesis. The remaining chapters are organized as follows:

Chapter 2 presents the plate-laminated waveguide filters in diffusion bonding technology and shows their uses in the integration with a corporate-feed slot array antenna for E-band ultra-high capacity point-to-point communications. After characterization of a single cavity resonator, a bandpass filter and a bandstop filter both centered at 78.5 GHz are developed. Then the proposed filters are fully integrated into a corporate-feed circuit of a  $16 \times 16$ -element slot array antenna without an interconnection circuit.

Chapter 3 presents the design and characterization of an E-band  $16 \times 16$ -slot monopulse array antenna with full-corporate-feed fabricated by diffusion bonding of laminated copper plates. The antenna is multi-layered,

and consists of vertically-interconnected radiating elements, a corporate-feed circuit and a comparator. It has four input ports for different excitations. Sum and difference beams in different cut-planes for monopulse operation can be generated.

Chapter 4 presents a RLSA, which is fed by an OAM beam-switching circuit, for V-band OAM multiplexing applications. The OAM beam-switching circuit is based on a post-wall waveguide structure and it feeds the RLSA through four open posts. The OAM beam-switching circuit can launch different progressive phase states in the RLSA parallel plate waveguide (PPW). The simulated results show that, at the design frequency, the proposed antenna can generate three OAM-mode states:  $l = 0$ ,  $-1$  and  $+1$ .

Chapter 5 presents the conclusions and the future prospects of this thesis.

## References

- [1.1] Federal Communications Commission, “Millimeter wave propagation: spectrum management implications,” Office of Engineering and Technology, bulletin number 70, July 1997.
- [1.2] B. Clerckx, A. Lozano, S. Sesia, C. van Rensburg, and C. B. Papadias, “3GPP LTE and LTE-Advanced,” *EURASIP J. Wireless Commun. Netw.*, vol. 2009, no. 1, Sep. 2009.
- [1.3] D. Lockie and D. Peck, “High-data-rate millimeter-wave radios,” *IEEE Microw. Mag.*, vol. 10, no. 5, pp. 75–83, Aug. 2009.
- [1.4] J. Wells, *Multi-Gigabit Microwave and Millimeter-Wave Wireless Communications*. Boston, MA, USA: Artech House, 2010.
- [1.5] UMTS Forum, “Mobile traffic forecasts: 2010–2020 report,” vol. 44, 2011.
- [1.6] Cisco, “Cisco visual network index: Global mobile traffic forecast update,” 2013.
- [1.7] J. Wenger, “Automotive radar – Status and perspectives,” in *Proc. IEEE Compound Simicond. Integr. Circuit Symp. (CSIC)*, pp. 21–25, Oct. 2005.
- [1.8] R. Appleby and R. N. Anderton, “Millimeter-wave and submillimeter-wave imaging for security and surveillance,” *Proc. of IEEE*, vol. 95, no. 8, pp. 1683–1690, Aug. 2007.
- [1.9] Z. Pi and F. Khan, “An introduction to millimeter-wave mobile broadband systems,” *IEEE Commun. Mag.*, vol. 49, no. 6, pp. 101–107, June 2011.
- [1.10] G. Wu, S. Talwar, K. Johnsson, N. Himayat, and K. D. Johnson, “M2M: From mobile to embedded internet,” *IEEE Commun. Mag.*, vol. 49, no. 4, pp. 36–43, Apr. 2011.

- [1.11] T. S. Rappaport, J. N. Murdock, and F. Gutierrez, "State of the art in 60-GHz integrated circuits and systems for wireless communications," *Proc. of IEEE*, vol. 99, no. 8, pp. 1390–1436, Aug. 2011.
- [1.12] T. S. Rappaport, S. Sun, R. Mayzus, H. Zhao, Y. Azar, K. Wang, G. N. Wong, J. K. Schulz, M. Samimi, and F. Gutierrez, "Millimeter wave mobile communications for 5G cellular: It will work!" *IEEE Access*, vol. 1, pp. 335–349, May 2013.
- [1.13] Z. Pi, J. Choi, and R. W. Heath Jr, "Millimeter-wave Gbps broadband evolution towards 5G: Fixed access and backhaul," *IEEE Commun. Mag.*, vol. 54, no. 4, pp. 138–144, Apr. 2016.
- [1.14] R. Daniels, J. Murdock, T. S. Rappaport, and R. Heath, "60 GHz wireless: Up close and personal," *IEEE Microw. Mag.*, vol. 11, no. 7, pp. 44–50, Dec. 2010.
- [1.15] Allocation and service rules for the 71–76 GHz, 81–86 GHz and 92–95 GHz bands, Federal Communication Commission, FCC-03-248, Nov. 2003 [Online]. Available: [https://apps.fcc.gov/edocs\\_public/attachement/FCC-03-248A1.pdf](https://apps.fcc.gov/edocs_public/attachement/FCC-03-248A1.pdf)
- [1.16] S. Rajagopal, S. Abu-Surra, Z. Pi, and F. Khan, "Antenna array design for multi-Gbps mmwave mobile broadband communication," in *Proc. IEEE Global Telecommun. Conf.*, pp. 1–6, Dec. 2011.
- [1.17] K. Solbach and R. Schneider, "Review of antenna technology for millimeter-wave automotive sensors," in *Proc. Euro. Microw. Conf.*, pp. 139–142, Oct. 1999.
- [1.18] H. Iizuka, K. Sakakibara, T. Watanabe, K. Sato, and K. Nishikawa, "Millimeter-wave microstrip array antenna with high efficiency for automotive radar systems," *R&D Review of Toyota CRDL*, vol. 37, no. 2, pp. 7–12, 2002.

- [1.19] M. Ando, K. Sakurai, N. Goto, K. Arimura, and Y. Ito, "A radial line slot antenna for 12 GHz satellite TV reception," *IEEE Trans. Antennas Propag.*, vol. 33, pp. 1347–1353, Dec. 1985.
- [1.20] M. Takahashi, J. Takada, M. Ando, and N. Goto, "A slot design for uniform aperture field distribution in single-layered radial line slot antennas," *IEEE Trans. Antennas Propag.*, vol. 39, pp. 954–959, July 1991.
- [1.21] K. Sakakibara, J. Hirokawa, M. Ando, and N. Goto, "Single-layer slotted waveguide arrays for millimeter wave applications," *IEICE Trans. Commun.*, vol. E79-B, no. 12, pp. 1765–1772, Dec. 1996.
- [1.22] M. Ando, J. Hirokawa, T. Yamamoto, A. Akiyama, Y. Kimura, and N. Goto, "Novel single-layer waveguides for high-efficiency millimeter wave arrays," *IEEE Trans. Microw. Theory Techn.*, vol. 46, no. 6, pp. 792–799, Jun. 1998.
- [1.23] J. Hirokawa and M. Ando, "Single-layer feed waveguide consisting of posts for plane TEM wave excitation in parallel plates," *IEEE Trans. Antennas Propag.*, vol. 46, no. 5, pp. 625–630, May 1998.
- [1.24] A. Akiyama, T. Yamamoto, J. Hirokawa, M. Ando, E. Takeda, and Y. Arai, "High gain radial line slot antennas for millimeter wave applications," *IEE Proc. Microw. Antennas Propag.*, vol. 147, no. 2, pp. 134–138, Apr. 2000.
- [1.25] Y. Kimura, T. Hirano, J. Hirokawa, and M. Ando, "Alternating-phase fed single-layer slotted waveguide arrays with chokes dispensing with narrow wall contacts," *IEE Proc. Microw. Antennas Propag.*, vol. 148, no. 6, pp. 295–301, Oct. 2001.
- [1.26] J. Hirokawa, M. Zhang, and M. Ando, "Millimeter waveguide fabrication to reduce transmission loss by diffusion bonding, light-curing resin or dielectric partially-filling," in *Proc. Asia-Pacific Microw. Conf.*, pp. 1–4, Dec. 2008.

- [1.27] M. Ando and J. Hirokawa, "Planar waveguide antennas for millimeter-wave systems," *ICMTCE2009*, Nov. 2009.
- [1.28] T. Tomura., J. Hirokawa, T. Hirano, and M. Ando, "A 45° linearly polarized hollow-waveguide  $16 \times 16$ -slot array antenna covering 71–86 GHz band," *IEEE Trans. Antennas Propag.*, vol. 62, no. 10, pp. 5061–5067, Oct. 2014.
- [1.29] D. J. Kim, J. Hirokawa, M. Ando, J. Takeuchi, and A. Hirata, " $64 \times 64$ -element and  $32 \times 32$ -element slot array antennas using double-layer hollow-waveguide corporate-feed in the 120-GHz band," *IEEE Trans. Antennas Propag.*, vol. 62, no. 3, pp. 1507–1512, Mar. 2014.
- [1.30] M. Zhang, K. Tokosaki, J. Hirokawa, M. Ando, T. Taniguchi and M. Noda, "A 60 GHz-band compact-range gigabit wireless access system using large array antennas," *IEEE Trans. Antennas Propag.*, vol. 63, no. 8, pp. 3432–3440, Aug. 2015.
- [1.31] J. Wu, Y. J. Cheng, and Y. Fan, "A wideband high-gain high-efficiency hybrid integrated plate array antenna for V-band inter-satellite links," *IEEE Trans. Antennas Propag.*, vol. 63, no. 4, pp. 1225–1233, Apr. 2015.
- [1.32] J. F. Xu, Z. N. Chen, X. Qing, and W. Hong, "140-GHz planar broadband LTCC SIW slot antenna array," *IEEE Trans. Antennas Propag.*, vol. 60, no. 6, pp. 3025–3028, Jun. 2012.
- [1.33] Y. She, J. Hirokawa, and M. Ando, "Loss evaluation of post-wall waveguides and its effect on antenna efficiency in millimeter-wave bands," in *Proc. Asia Pac. Microw. Conf. (APMC)*, Singapore, pp. 2041–2044, Dec. 2009.
- [1.34] Operation of radar services in the 76-81 GHz band, Federal Communication Commission, FCC-15-16, Feb. 2015 [Online]. Available: [https://apps.fcc.gov/edocs\\_public/attachmatch/FCC-15-16A1\\_Rcd.pdf](https://apps.fcc.gov/edocs_public/attachmatch/FCC-15-16A1_Rcd.pdf)

- [1.35] N. Ghassemi, J. Gauthier, and K. Wu, “Low-cost E-band receiver front-end development for gigabyte point-to-point wireless communications,” in *Eur. Microw. Conf.*, pp. 1011–1014, Oct. 2013.
- [1.36] Y. Yusuf, H. T. Cheng, and X. Gong, “A seamless integration of 3-D vertical filters with highly efficient slot antennas,” *IEEE Trans. Antenna Propag.*, vol. 59, no. 11, pp. 4016–4022, Nov. 2011.
- [1.37] S. M. Sherman and D. K. Barton, *Mono-Pulse Principles and Techniques*, 2nd ed. Norwood, MA, USA: Artech House, 2011.
- [1.38] D. D. Howard, “High range-resolution monopulse tracking radar,” *IEEE Trans. on Aerosp. Electron. Syst.*, vol. AES-11, no. 5, pp. 749–755, Sep. 1975.
- [1.39] I. Gresham et al., “Ultra-wideband radar sensors for short-range vehicular applications,” *IEEE Trans. Microw. Theory Techn.*, vol. 52, no. 9, pp. 2105–2122, Sep. 2004.
- [1.40] N. Iwakiri, N. Hashimoto, and T. Kobayashi, “Performance analysis of ultra-wideband channel for short-range monopulse radar at Ka-Band,” *Journal of Electrical and Computer Engineering*, vol. 2012, Article ID 710752, 9 pages, 2012.
- [1.41] M. Sierra-Castaner, M. Sierra-Perez, M. Vera-Isasa, and J. L. Fernandez-Jambrina, “Low-cost monopulse radial line slot antenna,” *IEEE Trans. Antennas Propag.*, vol. 51, no. 2, pp. 256–262, Feb. 2003.
- [1.42] H. Wang, D. G. Fang, and X. G. Chen, “A compact single layer monopulse microstrip antenna array,” *IEEE Trans. Antennas Propag.*, vol. 54, no. 2, pp. 503–509, Feb. 2006.
- [1.43] Y. J. Cheng, W. Hong, and K. Wu, “94 GHz substrate integrated monopulse antenna array,” *IEEE Trans. Antennas Propag.*, vol. 60, no. 1, pp. 121–129, Sep. 2012.



- [1.44] K. Tekkouk, M. Ettorre, L. L. Coq, and R. Sauleau, “SIW pillbox antenna for monopulse radar applications,” *IEEE Trans. Antennas Propag.*, vol. 63, no. 9, pp. 3918–3927, Sep. 2015.
- [1.45] A. K. Singh, “A low cost, low side lobe and high efficiency nonorthogonally coupled slotted waveguide array antenna for monopulse radar tracking,” in *IEEE Antennas and Propagation Society International Symposium*, pp. 732–735, July 2005.
- [1.46] W. T. Zhang, F. Y. Cui, Q. Wang, X. Y. He, C. F. She, and Y. Y. He, “Design of a waveguide slot array antenna for monopulse tracking application in millimeter wave,” in *Proceedings of the 12th European Radar Conference*, pp. 469–472, Sep. 2015.
- [1.47] G.-L. Huang, S.-G. Zhou, T.-H. Chio, C.-Y.-D. Sim and T.-S. Yeo, “Wideband dual-polarized and dual-monopulse compact array for SAR system integration,” *IEEE Geosci. Remote Sens. Lett.*, vol. 13, no. 8, pp. 1203–1207, Aug. 2016.
- [1.48] J. Wang. et al., “Terabit free-space data transmission employing orbital angular momentum multiplexing,” *Nature Photonics*, vol. 6, pp. 488–496, June 2012.
- [1.49] Z.-G. Guo, and G.-M. Yang, “Radial uniform circular antenna array for dual-mode OAM communication,” *IEEE Antennas Wireless Propag. Lett.*, vol.16, pp. 404–407, Mar. 2017.

## Figures and Tables

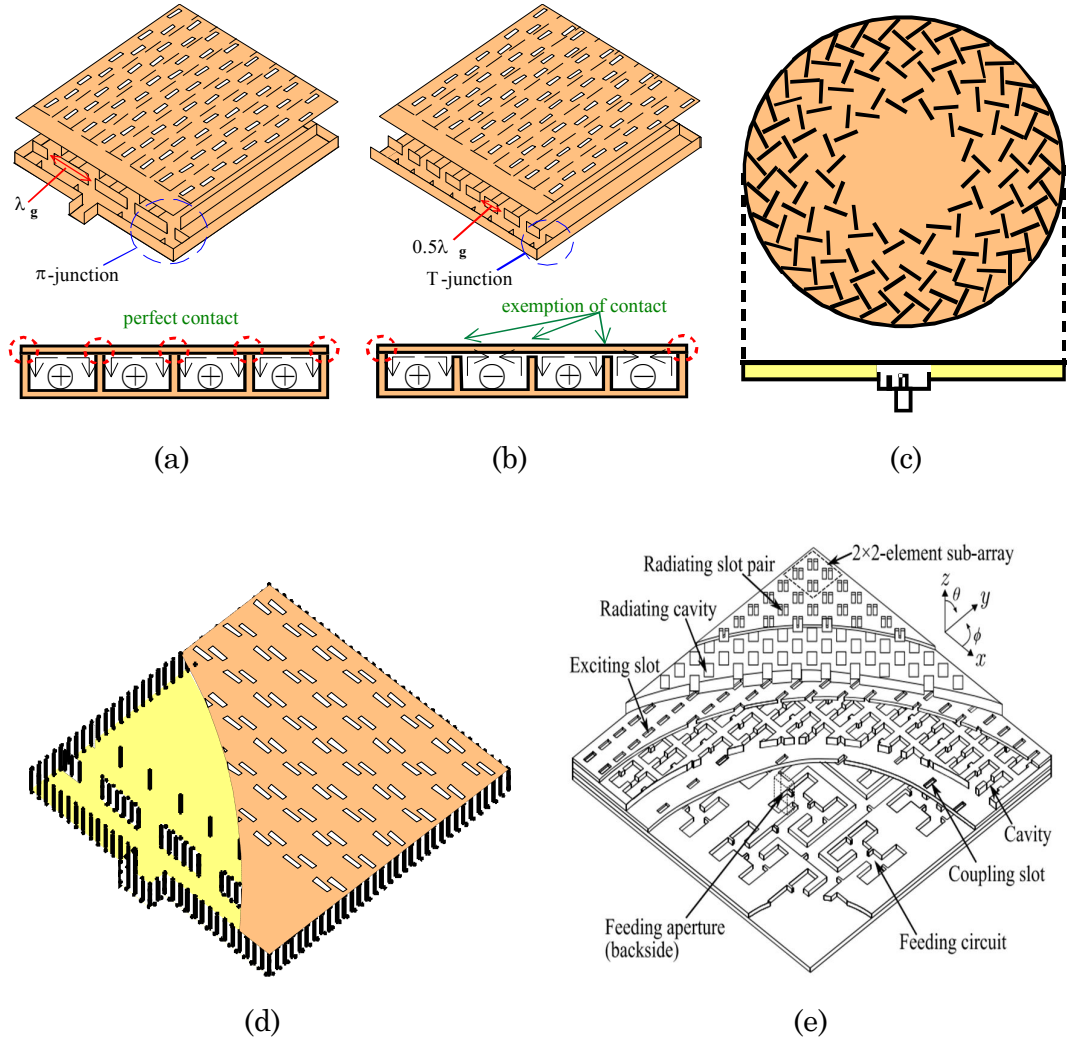


Fig. 1.1 Waveguide slot array antennas pioneered at Tokyo Tech. (a) Co-phase-feed single-mode waveguide slot array antenna. (b) Alternating-phase-feed single-mode waveguide slot array antenna. (c) Radial line slot antenna (RLSA). (d) Post-wall waveguide slot array antenna. (e) Plate-laminated hollow-waveguide slot array antenna.

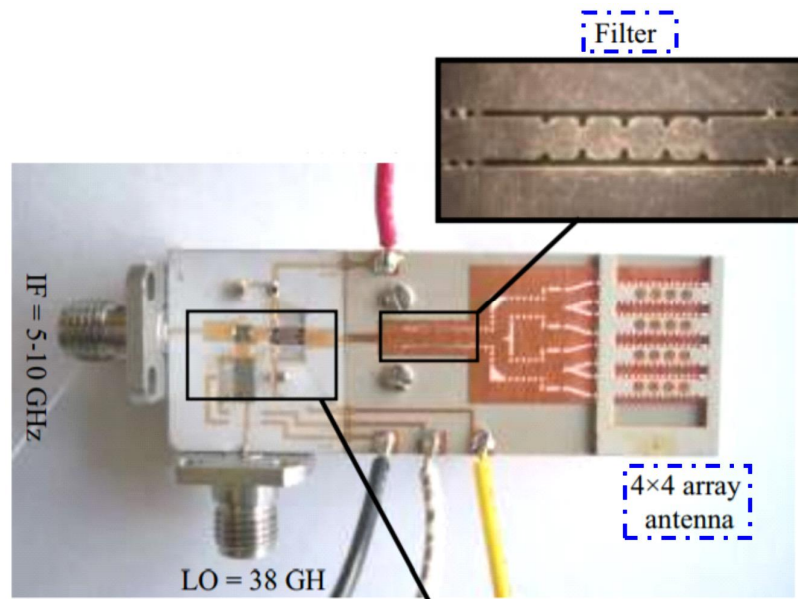


Fig. 1.2 Integration scenario in [1.35].

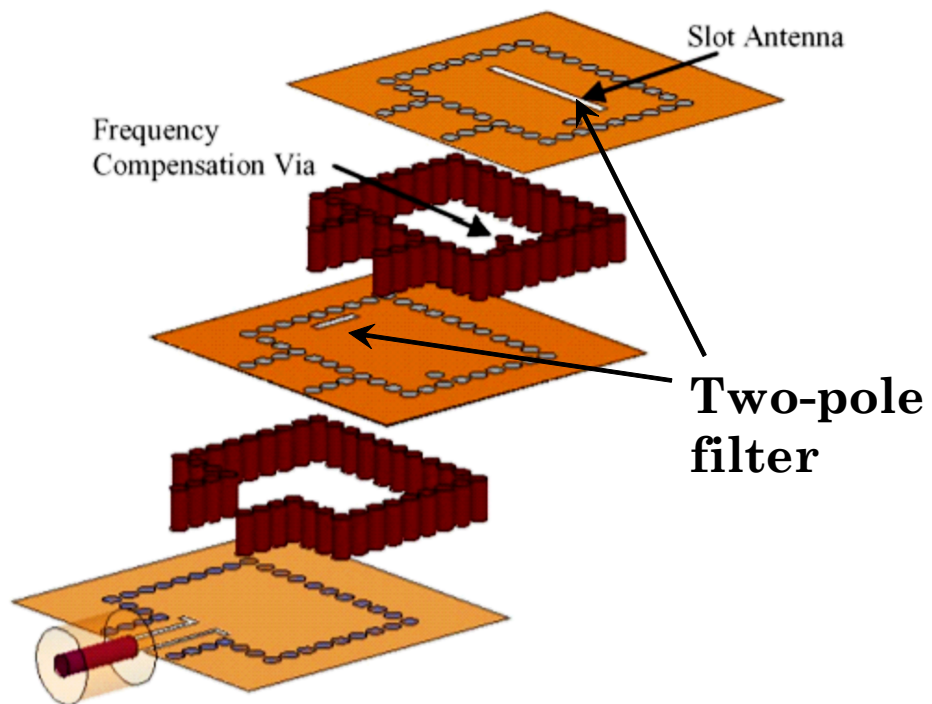
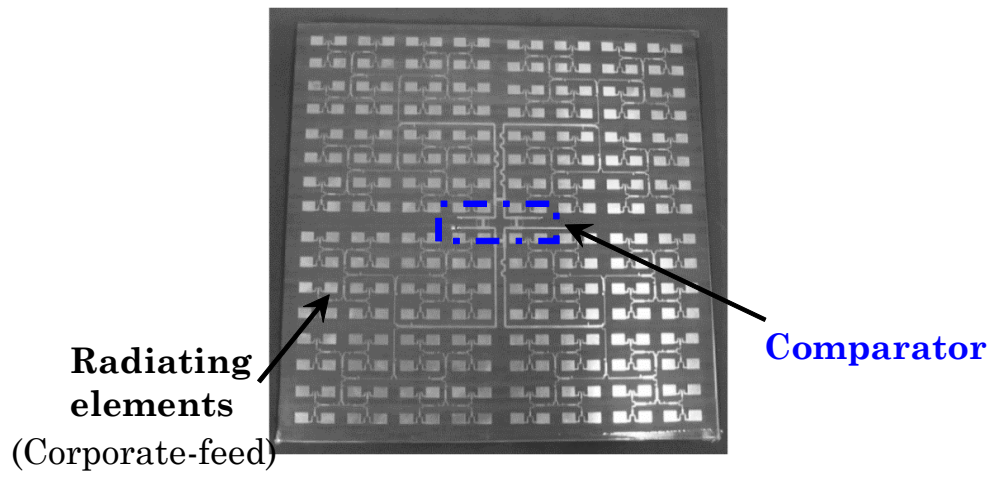
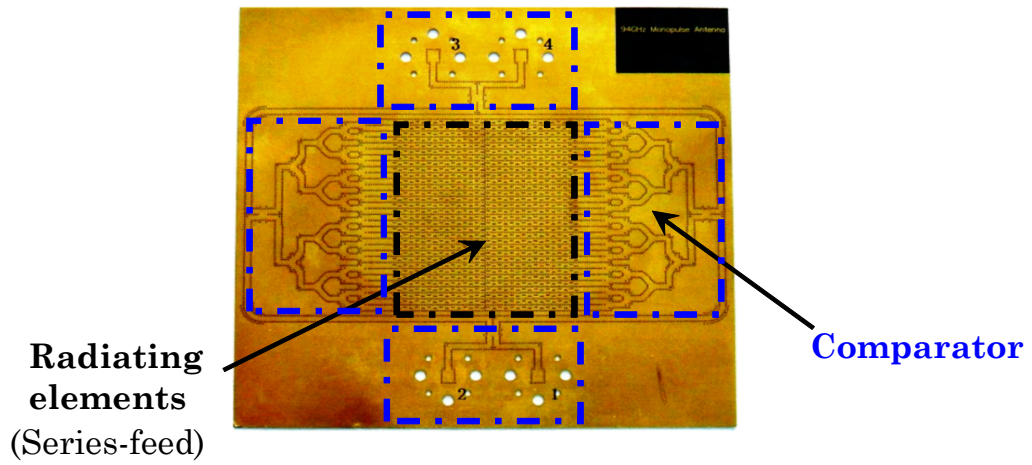


Fig. 1.3 Integration scenario in [1.36].



(a)



(b)

Fig. 1.4 Monopulse array antennas proposed in (a) [1.42] and (b) [1.43].

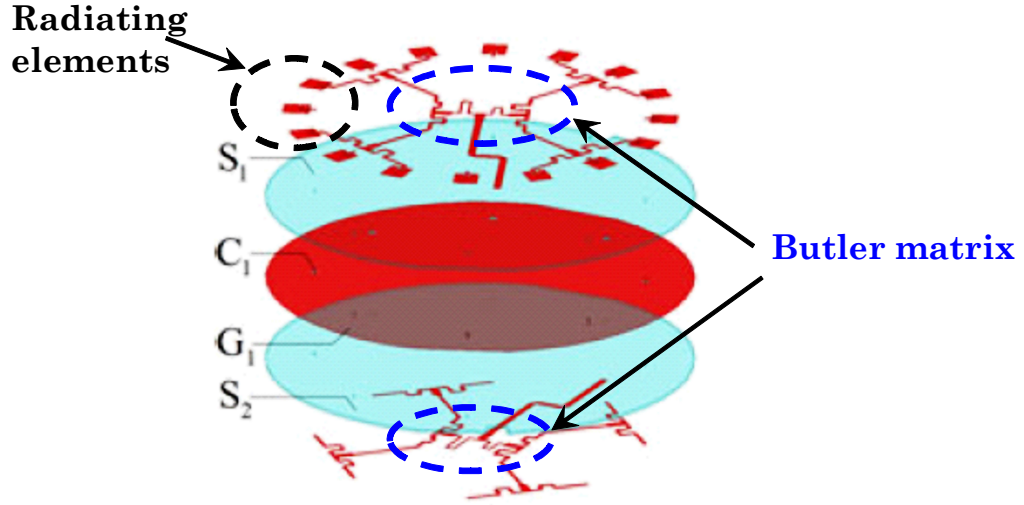


Fig. 1.5 Array antenna for OAM applications proposed in [1.49].

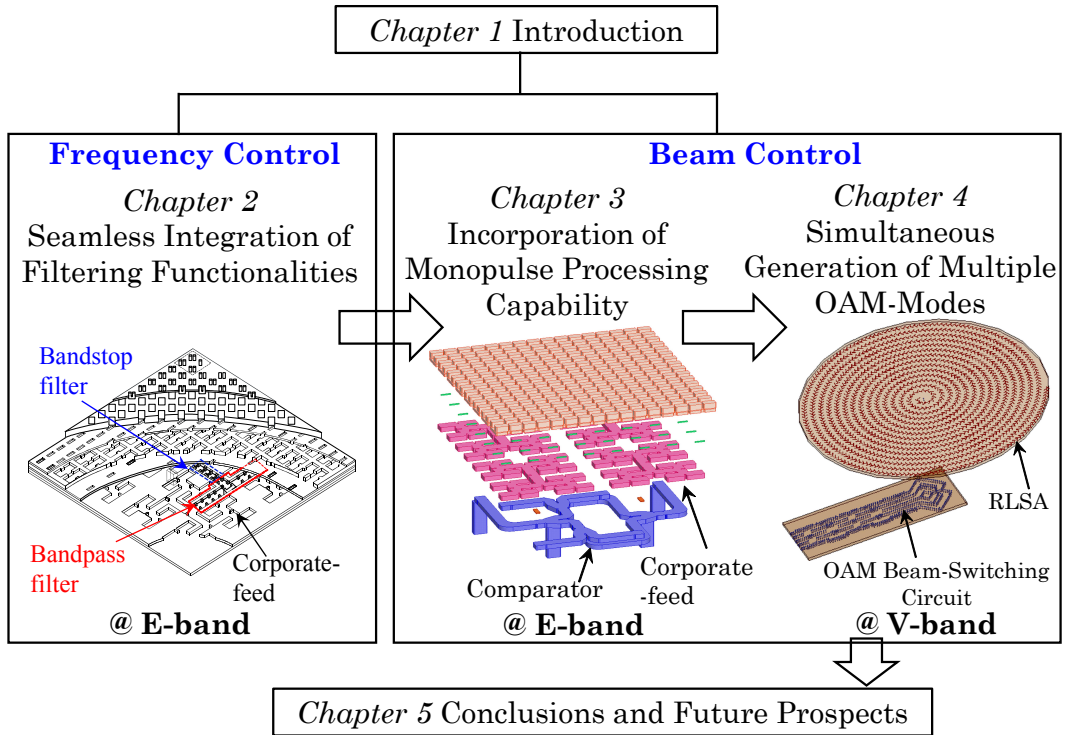


Fig. 1.6 Flowchart of the thesis.

# Chapter 2 Seamless Integration of Filtering Functionalities

## 2.1 Introductory Remarks

An E-band  $16 \times 16$ -element slot array antenna has been demonstrated in [1.28]. It can cover the full 71–86-GHz band and is expected to be a promising candidate for future applications in E-band multi-Gbps point-to-point wireless communication links due to its excellent performance such as wide bandwidth, high gain, high efficiency, low sidelobe level (SLL) and so on.

This chapter presents a first extensive report, validated by measured data for E-band waveguide filters fabricated by diffusion bonding of laminated thin copper plates. After experimental characterization of a single cavity resonator, a T-shaped bandpass filter with simultaneous power-division/band-selection and a compact bandstop filter using a band-rejection element are both designed at 78.5 GHz to suppress the unwanted frequency bands in E-band application. The design guidelines are provided and the design hurdles including fabrication stability, compatibility, miniaturization and overall performance are addressed. Especially, in the bandstop filter design using the band-rejection element [2.1], critical locations where the diffusion bonding may not succeed well are investigated and empirical values are provided to enable corrections in practice. It needs to be emphasized that this is a first experimental investigation of this kind of band-rejection element in practical bandstop filter design. The measured results of the developed filters are presented and discussed to show the validity of the predicted results.

This chapter also demonstrates the integration of a  $16 \times 16$ -element slot array antenna [1.28] and the proposed filters that combine the radiating and filtering functionalities in one package. A seamless integration strategy is adopted to enable the filters to be fully integrated into the corporate-feed

circuit of the array antenna, without imposing a detuning effect on the radiating elements. The part of the feeding circuit is replaced with the filters, which does not increase the total volume. This methodology is the first to provide an effective way ahead to the full and high-density integration of E-band passive front-end waveguide components using a batch process. Two prototypes with different specifications have been characterized and fabricated: one with a single wideband passband (building block 1); and one with two narrow passbands (building block 2). The reflection, realized gain, directivity, cross polarization, and radiation pattern of the two building blocks are measured to illustrate the validity of the design approach.

## 2.2 Design and Characterization of the Filters

### 2.2.1 The Cavity Resonator

As the basis of the cavity filter design, the characterization on a single cavity resonator must be performed. Fig. 2.1 shows a 3-D overview and a side view of the cavity resonator:  $a \times b \times c = 2.40 \text{ mm} \times 2.94 \text{ mm} \times 1.00 \text{ mm}$  with two narrow inductive windows for weak excitation. Such a coupling structure is advantageous in the fabrication process using diffusion bonding of laminated thin metal plates, because it occupies only one etching pattern and the coupling strength can be simply adjusted by the width of the inductive window without adding to the number of etching patterns.

Theoretically, for a hollow-waveguide cavity with a given resonance frequency, the unloaded quality factor  $Q_u$  is mainly determined by the metal used in the stack and the height dimension of the cavity. The metals that are currently possible for use in diffusion bonding in the company in charge of fabrication are copper and stainless steel.

Relevant details for these two metals are detailed in Table 2.1. The simulated result by the eigenmode solver shows that the TE<sub>101</sub>-mode in the

cavity is resonating at approximately 78.48 GHz. The  $Q_u$  can be greatly improved by increasing the cavity height, but considering the integration in this study the  $c$  is chosen as 1.00 mm. The fabrication stability should be the primary concern and our previous study has shown that copper and stainless steel are sufficiently stable during the fabrication [1.28–30]. As shown in Table 2.1, the cavity with copper has a much higher  $Q_u$  than the one with stainless steel due to its higher conductivity. However, copper has a higher density than stainless steel, resulting in a tradeoff between weight and performance. To meet the stringent system requirement in terms of loss and efficiency, the metal used in this study is selected as copper.

The  $Q_u$  could also be evaluated by the following equations using a two-port transmission model [2.2]:

$$\frac{1}{Q_u} = \frac{1}{Q_l} - \frac{1}{Q_{ext}} \quad (2-1)$$

$$Q_l = \frac{f_{res}}{\Delta f_{3-dB}} \quad (2-2)$$

$$S_{21} = 20 \log_{10} \left( \frac{Q_l}{Q_{ext}} \right) \quad (2-3)$$

where  $Q_l$  is the loaded  $Q$  factor,  $Q_{ext}$  is the external  $Q$  factor that includes the input-output loading effects,  $f_{res}$  is the resonance frequency,  $S_{21}$  is the insertion loss at the resonance frequency, and  $\Delta f_{3-dB}$  is the 3-dB bandwidth of the  $f_{res}$ .

The geometry of a single transition used for measurement is inserted in Fig. 2.2. Each port of the cavity resonator is interconnected with one transition. To accommodate the waveguide flanges in the measurement, the distance between the adjacent WR-12 ports is selected to be 24 mm. Fig. 2.2 shows the simulated results of two back-to-back interconnected transitions, where the length of the straight waveguide is set to be 24 mm. Within 71–86-GHz band, the simulated reflection is less than  $-16$  dB, and the insertion loss varies between 0.11 to 0.21 dB. This transition will be used in the



measurement hereafter and its effect will be included in the measured results.

Fig. 2.3 shows the simulated result of the single cavity resonator. The simulated  $f_{\text{res}}$  and  $Q_u$  using the two-port transmission model are extracted as 78.49 GHz and 2261 respectively, which show good agreement with the results using the HFSS eigenmode solver.

The structure including the single cavity and the transitions is fabricated by diffusion bonding of laminated thin copper plates. The fabrication flow has been detailed elsewhere [1.28–30]. In fabrication, the inherent tolerance mainly comes from the etching and the laminating process. We estimate the inherent fabrication tolerance by comparing the measured result to the simulated result of the model with an imposed over- or under-etching amount in all the design parameters. If they can match well, then we take the effect of the imposed etching amount equivalent to the effect from the inherent fabrication tolerance. Note that the equivalent etching amount is normally within a range when the fabricated structure is complex, because the measured result may partially match with the simulated results of the model with different imposed etching amounts. Our previous researches have shown that the inherent tolerance in fabrication can be equivalent to an over-etching amount, within 0–30  $\mu\text{m}$ . Therefore, to compensate the inherent fabrication tolerance, we impose a 20- $\mu\text{m}$  under-etching (also abbreviated as “–20- $\mu\text{m}$ ”) in all the fabrication parameters in the computer-aided drafting (CAD) of the cavity resonator.

The cavity is composed of eight plates of 0.1 mm thick and one of 0.2 mm thick. This arrangement is mainly determined by the structure of the bandstop filter that is co-fabricated, and which will be discussed below. The measured result and the photograph of the fabricated prototype are added Fig. 2.3. The measured resonance frequency is 79.07 GHz, with a 23.32-dB insertion loss and a 3-dB bandwidth of 40 MHz. The measured  $Q_u$  is found to be 2121. The measured resonance frequency matches well with the simulated

result of the 8- $\mu\text{m}$  under-etching model, which yields a  $Q_u$  of 2348 with a peak insertion loss of 22.9 dB. The discrepancy between the measured and simulated  $Q_u$  can mainly be attributed to the measurement tolerance. As the bandwidth is quite narrow, it is difficult to identify an accurate peak frequency and the corresponding 3-dB bandwidth due to the limited data points in measurement.

Considering the imposed 20- $\mu\text{m}$  under-etching in CAD, the inherent fabrication tolerance here could be equivalent to 12- $\mu\text{m}$  over-etching (also abbreviated as “+12- $\mu\text{m}$ ”).

The simulated and measured results of the cavity resonator are summarized in Table 2.1. The good agreement between the simulated and measured results demonstrates again the high fabrication quality in terms of the bonding and the surface roughness, thus verifying the feasibility of realizing low-loss filters at the E-band.

### 2.2.2 Design of the Bandpass Filter

A bandpass filter with a T-shaped structure could replace the T-junction in the corporate-feed circuit with simultaneous power-division/band-selection and use the space available in the feeding circuit more efficiently.

Fig. 2.4 shows the geometric configuration and the schematic topology of the proposed T-shaped bandpass filter. The filter consists of ten coupled cavity resonators marked Cavities 1 to 10 and arranged in a T-shape. The widths of the cavities are 2.40 mm and the heights are 1.00 mm, with the internal and external couplings both realized by the inductive window, and the coupling strength can be adjusted by the width of the window. The cavities operate in the fundamental  $\text{TE}_{101}$ -mode. Cavities 1 and 2 are co-shared cavities and the order of the filtering responses of the channels,  $S_{21}$  and  $S_{31}$ , is six. Cavity 2 is at the center of the T-junction and the power from Port 1 is

equally divided to Ports 2 and 3 if the coupling strength to Cavity 3 and that to Cavity 7 are equal. Due to the field distribution characteristics of the TE<sub>101</sub>-mode utilized in Cavity 2, the ideal phase difference between Ports 2 and 3 is zero. The main specification of the proposed filter is set to a 3-dB fractional bandwidth of 20% centered at 78.5 GHz with a -20-dB in-band reflection.

The synthesis procedure of the coupling matrix of the proposed 3-port T-shaped filter is similar to that of a 2-port filter ( $S_{21}$  or  $S_{31}$ ) with sixth-order coupled resonators [2.3, 4]. The design parameters of the external coupling coefficient ( $Q_{\text{ext}}$ ) and the internal coupling coefficient ( $k_{ij}$ ) for the given filter specifications are determined as:  $Q_{p1,1} = Q_{p2,6} = Q_{p3,10} = 4.980$ ,  $k_{6,5} = k_{10,9} = 0.1686$ ,  $k_{5,4} = k_{9,8} = 0.1222$ ,  $k_{4,3} = k_{8,7} = 0.1167$ ,  $k_{3,2} = k_{7,2} = 0.0864$ ,  $k_{2,1} = 0.1686$ . The values of  $Q_{\text{ext}}$  and  $k_{ij}$  are mainly dependent upon the width of the inductive window ( $w$ ), and can then be extracted by full-wave simulations using the following relations [2.5]:

$$Q_{\text{ext}} = \frac{f_{\text{res}}}{\Delta f_{\pm 90^\circ}} \quad (2-4)$$

$$|k| = \frac{f_1^2 - f_2^2}{f_1^2 + f_2^2} \quad (2-5)$$

where  $\Delta f_{\pm 90^\circ}$  is the frequency difference between the  $\pm 90^\circ$  phase response of  $S_{11}$ ;  $f_1$  and  $f_2$  are the two split frequencies in the HFSS eigenmode solver. The calculated design curves are given in Fig. 2.5, making it possible to obtain the initial physical parameters of the filter. Note that the resonance frequency of the cavity resonator will be perturbed due to the presence of the inductive window, but it can be compensated for by shortening the cavity length. With the initial physical parameters, the whole filter structure is tuned by the full-wave optimization until the response meets the design specifications, and its final dimensions are marked in Fig. 2.4(a).

Fig. 2.6 shows the simulated results of the proposed T-shaped filter. The simulated results show that the filter has a center frequency of 78.5 GHz

with a 3-dB fractional bandwidth of 20.1%. The in-band reflection lower than  $-20.0$  dB is 12.1 GHz (15.4%), corresponding to an in-band insertion loss from 3.1 to 3.3 dB.

The proposed T-shaped filter is fabricated with plates similar to those used for the cavity resonator. An amount of  $20\text{-}\mu\text{m}$  under-etching is also imposed in the CAD. The measured results and the photograph of the fabricated prototype are shown in Fig. 2.6. The measured 3-dB bandwidth is 16.1 GHz (20.5%) with the in-band reflection less than  $-11.7$  dB. At the design frequency of 78.5 GHz, the insertion losses of  $S_{21}$  and  $S_{31}$  are 3.4 and 3.3 dB, respectively. The minimum insertion losses of  $S_{21}$  and  $S_{31}$  are both 3.1 dB at 77.1 and 80.9 GHz with the same 1-dB down bandwidth of 13.9 GHz (17.7%). An amplitude imbalance of less than 0.35 dB is maintained over the 67–90 GHz-band, while the bandwidth for a phase imbalance of less than  $2^\circ$  is 15.1 GHz (19.2%). Considering the imposed  $20\text{-}\mu\text{m}$  under-etching in the CAD, the inherent fabrication tolerance here is estimated to be  $30\text{-}\mu\text{m}$  over-etching because the measured results agree well with the simulated results of the  $10\text{-}\mu\text{m}$  over-etching model.

Table 2.2 lists the performance of the proposed T-shaped bandpass filter with other published waveguide cavity bandpass filters using the micromachining technique. Despite the differences in design frequency, bandwidth, I/O interface, and filtering order/type, the proposed filter shows an encouragingly low loss and has superior ease of fabrication. Further, as mentioned above, the T-shaped structure would be more easily compatible and attractive in E-band applications where high-gain array antennas associated with feeding networks are employed.

### 2.2.3 Design of the Bandstop Filter

The concept of the band-rejection element used here and its application in

bandstop filter design was first presented in [2.1], but there only by simulated results without consideration or discussion of practical fabrication and manufacture. This subsection presents a detailed discussion considering fabrication and manufacture.

The structure of the proposed bandstop filter is shown in Fig. 2.7(a), it is 5.6 mm long, less than one guided wavelength, and achieves significant volume and size reductions over traditional bandstop filters by the use of a cavity resonator [2.6]. It has four fully imbedded irises, each consisting of two windows and would be able to generate and control a transmission zero at a prescribed frequency within the stopband.

However, different from other examples in this paper, there is the possibility of a fabrication problem in this bandstop filter. In the bonding process, each iris of the bandstop will carry mechanical pressure from the top and bottom plates simultaneously. However, the structure of the iris is not uniform in its vertical direction due to the different lengths between the two windows. Therefore, as shown in Fig. 2.7(b), the contact surfaces indicated by red lines may cannot be fully bonded because they can only carry pressure from the bottom plates. We evaluate this effect by imposing an air gap with a length of  $0.5 \times (w_{\text{cap.}} - w_{\text{ind.}})$  around each red line. The air gap can perturb the resonance frequency of the inductive window and affect the filter response.

In implementation, to remedy the aforementioned problem regarding the bonding, only one 0.2-mm-thick plate is placed between the two windows. Further, to minimize the number of etching patterns, the height of the capacitive windows were both selected as 0.6 mm, and the height of the inductive windows were both selected as 0.2 mm, respectively.

The specification of the proposed bandstop filter is given to have a 5% fractional bandwidth centered at 78.5 GHz with a 0.1-dB ripple. Initially, the four irises are separated from each other by the distance of a quarter of the guided wavelength. Then, the working frequency of the iris can be determined

by placing its transmission zero at 78.5 GHz. The simulated results of the working frequency of the iris versus the width of its windows are plotted in Fig. 2.8, which shows that the working frequency is inversely proportional to the width of the window.

The rest of the design procedure can be conducted as introduced in [2.5]. The element values of the chosen low-pass prototype for the filter design are  $g_0 = 1.0000$ ,  $g_1 = 1.1088$ ,  $g_2 = 1.3061$ ,  $g_3 = 1.7703$ ,  $g_4 = 0.8180$ , and  $g_5 = 1.3554$ . Then, the theoretical slope parameters of the four band-rejection irises can be calculated as  $x_1 = 13.31$ ,  $x_2 = 11.30$ ,  $x_3 = 8.34$ ,  $x_4 = 18.04$ .

The slope parameter of a single iris could be extracted by simulation following the equation [2.5]:

$$x = \frac{f_0}{2\Delta f_{3\text{-dB}}} \quad (2-6)$$

where  $f_0$  is the center frequency and  $\Delta f_{3\text{-dB}}$  is the 3-dB bandwidth inside the stopband. For reference, some extracted slope parameters when an iris working at 78.5 GHz is provided in Fig. 2.8. Finally, the initial physical parameters of the irises and the distances between them are optimized until the overall response of the filter fully meets the design requirements. The detailed parameters of the proposed bandstop filter are:  $w_{\text{ind.1}} = w_{\text{ind.4}} = 1.71$  mm,  $w_{\text{ind.2}} = w_{\text{ind.3}} = 1.67$  mm,  $w_{\text{cap.1}} = w_{\text{cap.4}} = 2.02$  mm,  $w_{\text{cap.2}} = w_{\text{cap.3}} = 2.13$  mm,  $d_{12} = d_{34} = 1.81$  mm, and  $d_{23} = 1.79$  mm, where  $w_{\text{ind.i}}$  stands for the width of the inductive window of Iris  $i$ ,  $w_{\text{cap.i}}$  for the width of the capacitive window of Iris  $i$ ,  $d_{ij}$  for the distance between Iris  $i$  and Iris  $j$ , respectively.

The simulated results of the proposed bandstop filter are presented in Fig. 2.9. At the design frequency of 78.5 GHz, the transmission is rejected to  $-55$  dB. Within the 71–76 and 81–86-GHz bands, the reflection is below  $-9.9$  and  $-13.6$  dB, while the insertion loss ranges from 0.18 to 0.63 dB and from 0.27 to 0.59 dB, respectively.

The simulated results of the models with air gap or over-etching are added in Fig. 2.9. When the height of the air gap or the amount of the over-

etching increases, the center frequency of the bandstop filter decreases proportionally, the air gap degrades the filter performance in terms of rejection within the stopband and the reflection near the stopband, while the over-etching model performance is not degraded. This is because in the over-etching model, the design parameters of the two windows will simultaneously change with a same amount.

However, as aforementioned, the air gap will only perturb the resonance frequency of the inductive window. To confirm the existence of the supposed air gap and to investigate its characteristic, we fabricated four models: two with  $0\text{-}\mu\text{m}$  under-etching (the same with the design parameters) in CAD and two with  $30\text{-}\mu\text{m}$  under-etching in CAD. The widths of the capacitive windows of Iris 2 and Iris 3 are relatively large and 0.1-mm-thick plates are used to form the windows to precisely realize the corners, as required by the etching process. Therefore, the fabricated model is composed of eight 0.1-mm-thick plates and one 0.2-mm-thick plate and with three etching patterns.

The simulated and measured results of the bandstop filters are given in Fig. 2.10 and Table 2.3. The stable fabrication enables the models with the same fabrication parameters to exhibit very similar performances. The measured center frequencies of the two filters with  $0\text{-}\mu\text{m}$  under-etching in CAD are 75.2 GHz, while the ones of the filters with  $30\text{-}\mu\text{m}$  under-etching in CAD are 78.3 GHz. The etching effect of the assumed air gap can be obtained by comparing the difference between etching effects in the inherent fabrication, the CAD, and the center frequency shift. The estimated etching effects of the assumed air gap for the two filters with  $0\text{-}\mu\text{m}$  under-etching in CAD are  $+28\text{-}\mu\text{m}$ , while the ones for the two filters with  $30\text{-}\mu\text{m}$  under-etching in CAD are  $+20\text{-}\mu\text{m}$ . Therefore, we concluded that the effect from the assumed air gaps does exist.

It appears that the effect of the air gap seems to be somewhat unstable

at different etching amounts that imposed in CAD, however the center frequencies of the models with 30- $\mu\text{m}$  under-etching in CAD are quite near the design value while maintaining excellent performance. At the design frequency of 78.5 GHz, there is a 55-dB transmission-rejection level, while the transmission-rejection levels for better than 10 and 40 dB are 2.7 GHz (76.8–79.5 GHz) and 1.7 GHz (77.2–78.9 GHz). In each passband, the frequency bands for reflection below  $-15$  dB are from 73.0 to 75.9 GHz and 80.5 to 84.1 GHz, with insertion losses less than 0.9 and 1.2 dB. The insertion losses at 73.5 and 83.5 GHz are 0.44 and 0.28 dB, respectively. The relatively more significant degradation of the measured insertion loss around 76 and 86 GHz compared to the simulated loss is mainly due to the overall left-shifted frequency characteristics.

To the best knowledge of the authors, this is the first reported bandstop filter working over 76–81 GHz with such high performance and compact size suitable for E-band application.

A method to eliminate the air gap is under investigation in cooperation with the company in charge of the fabrication here, and a stronger bonding pressure over specific areas is expected to be able to effect this. Nevertheless, at this stage, trial-and-error would be adequate to determine the value empirically with the stable fabrication process. The empirical value of 30- $\mu\text{m}$  under-etching in CAD will be used for further validation in the next section. It can be pointed out that the investigation of the air gap here can be used as a reference for other fabrication techniques such as machining and micromachining. Because in the machining and micromachining techniques, imperfections may also be introduced when bonding or assembling a band-rejection element or other structure with similar critical parts as discussed above.



## 2.3 Integration of Filters into a $16 \times 16$ -Element Slot Array Antenna

### 2.3.1 Integration Strategy

Straightforward interconnection between an antenna array and a filtering circuit increases size, cost and system complexity, as well as it deteriorates the system performance including the efficiency [1.35], [2.7]. Some reports have addressed this based on dielectric-filled waveguides, aiming at effectively integrating filter and antenna [1.36], [2.8]. However, the integration technique there is not applicable here as the corporate-feed circuit and the radiating elements of the antenna array [1.28–30] have to be stacked, and occur in different layers. Further, the detuning effect on the radiating elements discussed in [1.36] and [2.8] has to be eliminated after the integration of the filtering functionality. This is because: i) the radiating elements in [1.28] are fully corporate-feed and work well over the entire 71–86-GHz band. An elimination of the detuning of the radiating elements could effectively reduce the design cycle time and speed the introduction of new products in practical E-band applications because only the feeding circuit would need to be modified based on the required filtering specification; and ii) the radiation pattern could be preserved if the radiating elements remain unchanged.

We propose two integrations of the filter to be fully incorporated into the corporate-feed circuit of the array antenna without any increase in or addition to the footprint or thickness: one includes the  $16 \times 16$ -element array antenna and the proposed bandpass filter only (building block 1); the other one includes the  $16 \times 16$ -element array antenna and the proposed bandpass/bandstop filters (building block 2). The geometric configuration of building block 2 and a half bisection of its corporate-feed circuit are shown in Fig. 2.11, while building block 1 is obtained by directly removing the bandstop filter of building block 2. As shown in Fig. 2.11(b), the two filters are fully

integrated into the corporate-feed circuit adding the filtering functionality there without additional interconnecting circuits. The radiating elements at the upper layer are corporately fed by the feeding circuit via coupling slots etched on the common metal plate. This seamless incorporation of the filters into the corporate-feed circuit play a critical role in the module miniaturization and performance improvement, enabling enhanced band-selectivity over the band of interest and reduced loss. Further, in this way the radiation characteristics of the radiating elements are preserved without additional detuning processes.

The two planar building blocks exhibit very low profiles and their effective sizes are both  $51.36 \text{ mm} \times 51.36 \text{ mm} \times 3.20 \text{ mm}$  ( $13.44 \lambda \times 13.44 \lambda \times 0.84 \lambda$  at 78.5 GHz), the same as the original antenna. The parameters of the radiating elements as well as the left part of the feeding circuit other than the integrated filters are the same as those of the original antenna.

The proposed bandstop can be imbedded in Branch 1 thanks to its compact size. The co-shared Cavities 1 and 2 of the T-shaped filter are fitted into Branch 3 while the remaining eight cavities are symmetrically arranged in Branches 1 and 2. This T-shaped arrangement uses the corporate-feed circuit more effectively and eases possible problems due to the antenna size when adopting the traditional in-line bandpass filter topology. For instance, the corporate-feed circuit in Fig. 2.11(b) is composed of cascading T-junctions, and the longest branch of these T-junctions are Branches 1 to 3, each 10.45 mm. Leaving out the bandstop filter, each of the branches could accommodate an in-line filter with at most four cavities and with two when the antenna size is halved to  $8 \times 8$ -element. This shows that the available filtering order can be doubled by using the T-shaped topology. A higher filtering order can improve the band-rejection level at the cost of higher in-band insertion loss [2.5].

Fig. 2.12 shows the simulated reflection of the corporate-feed circuit of

the building blocks. It can be found that the reflection characteristics of the corporate-feed circuit could be effectively controlled by its intrinsic filtering functionality, exhibiting similar shape with the designed filters. Within the frequency band of 67–90 GHz, the bandwidth for reflection  $< -10.0$  dB of the feeding circuit of building blocks 1 and 2 are 13.7 GHz (71.3–85.0 GHz) and 9.7 GHz (71.1–76.5 and 80.2–84.5 GHz) respectively. Implying that the transmission response of the feeding circuit outside the concerned passband have been well suppressed by the filters.

The simulated reflection characteristics of the two building blocks are provided in Fig. 2.13 and Fig. 2.14. It clearly shows that in comparison with the original antenna, the desired band-selection shape of the reflection contributed by the included filtering functionalities, could be achieved. The simulated realized gain, the cross polarization, and the directivity are plotted in Fig. 2.15. Due to the introduced loss by the filter, the realized gain of the two building blocks in the desired passband is slightly degraded compared to the original antenna, while the band-edge is steeper and the out-of-band rejection is more significant. Further, the radiating elements are well preserved, resulting in the cross polarization and the directivity of the two building blocks to be nearly unchanged.

The passband of building block 1 for  $V_{SWR} < 2$  is 13.7 GHz (71.3–85.0 GHz), and at its design frequency of 78.5 GHz, there is a 33.1-dBi realized gain with a 90.4% total efficiency. Within the bandwidth for  $V_{SWR} < 2$ , the realized gain ranges from 31.7 to 33.6 dBi, with the total efficiency 79.9% to 93.3%. Within the passband, the maximum gain-reduction is 0.2 dB compared to the original antenna.

The passband of building block 2 for  $V_{SWR} < 2$  is from 72.3–76.2 GHz and 80.3–84.3 GHz, with the realized gains 31.5 to 32.6 dBi and 30.6 to 33.4 dBi, respectively. At 67, 78.5, and 90 GHz, the realized gains are  $-2.1$ ,  $-14.7$ , and 16.2 dBi, respectively. The building block 2 also supports a bandwidth for

total efficiency higher than 70% from 70.8 to 76.2 GHz, and 80.4 to 84.8 GHz. Within the passband, the maximum gain-reduction is 0.4 dB compared to the original antenna.

### 2.3.2 Fabrication and Experiments

The two building blocks are fabricated by diffusion bonding of laminated thin copper plates without any subsequent assembly process. The fabrication parameters of the bandstop filter included in the building block 2 are imposed with  $30\text{-}\mu\text{m}$  under-etching in CAD based on the discussion in the previous section, while the other fabrication parameters of the two building blocks are still with  $20\text{-}\mu\text{m}$  under-etching in CAD. The feeding circuits of the two building blocks are composed of eight 0.1-mm-thick plates and one 0.2-mm-thick plate. The radiating elements are composed of ten 0.2-mm-thick plates.

Fig. 2.16 shows the photograph of the fabricated prototype. The measured results of the realized gain and the radiation patterns are carried out by V- and W-band test systems for the 67–75-GHz and 75–90-GHz bands, respectively, and the directivity is transformed from the measured near-field results with the realized gain estimated in comparison with a standard gain horn.

The measured reflection characteristics of the two building blocks are added in Fig. 2.13 and Fig. 2.14. The measured results show that building block 1 supports a passband for  $\text{VSWR} < 2$  of 13.4 GHz (71.3–84.7 GHz); while building block 2 supports a passband for  $\text{VSWR} < 2$  of 9.6 GHz segmented by 71.1–75.6 and 79.4–84.5 GHz. Outside their passbands of interest, the transmissions are gradually attenuated.

From the frequency shift of the periphery passband skirt, the inherent fabrication tolerance equivalent to over-etching in the building block 1 is within 0–20  $\mu\text{m}$ , while that in the building block 2 (apart from the bandstop

filter) is within 20–30  $\mu\text{m}$ . Considering the estimated results from the cavity resonator (+12- $\mu\text{m}$ ) and the bandpass filter (+30- $\mu\text{m}$ ), it can be concluded that the inherent fabrication tolerance in the first fabrication is equivalent to over-etching within 0–20  $\mu\text{m}$  while the one in the second fabrication is within 20–30  $\mu\text{m}$ . Due to the random and unavoidable error in each fabrication process, the two fabrications here exhibit slightly different tolerance amounts, which however are still within the empirical value of 0–30  $\mu\text{m}$ .

The measured stopband center frequency of building block 2 is 77.9 GHz, which is left shifted by about 600 MHz compared to the designed result but matching well with the simulated result of the model with 10- $\mu\text{m}$  over-etching in the bandstop filter. However, given the more inherent tolerance amount in over-etching in the second fabrication, the empirical value of 30- $\mu\text{m}$  under-etching in CAD for the bandstop filter in this study can in principle be considered effective.

The measured characteristics of the realized gain, the cross polarization and the directivity are included in Fig. 2.15. For building block 1, at the design frequency of 78.5 GHz, there is a 33.0-dBi directivity, a 32.7-dBi realized gain, and an 82.7% total efficiency. Within the bandwidth of 71.3–84.7 GHz, a total efficiency above 70% is fully supported. The realized gain is more than 32 dBi across 73.6–84.7 GHz, and suppressed to -1.3 and 17 dBi at 67 and 90 GHz. For building block 2, it supports a bandwidth for total efficiency above 69% from 71.9–75.4 and 79.8–84.8 GHz, for a realized gain of more than 31.4 dBi from 72–75.5 and 75.6–84.7 GHz. At 67, 78.5, and 90 GHz, the realized gains are shaped to 5.9, -3, and 17.8 dBi, respectively. At the 73.5 and 83.5 GHz, the measured realized gain/directivity are 32/32.8 and 32.3/33.4 dBi, respectively. Note that in the gain measurement, the parasitic loss introduced by the jig and the waveguide connectors (such as WR-12 to WR-10/15 transition, angle transformer, straight connector, etc.) that used for interconnecting the antenna and the test system cannot be

eliminated by calibration. This parasitic loss is roughly estimated as between 0.2 and 0.4 dB within the E-band.

The simulated/measured conductor losses of building block 1 at 73.5, 78.5, and 83.5 GHz are 0.42/0.72, 0.33/0.35 and 0.30/0.51 dB; for building block 2 at 73.5 and 83.5 GHz, they are 0.56/0.80 and 0.44/0.61 dB, respectively. The discrepancy between the simulated and measured conductor losses can be attributed to the measurement error in the realized gain and the directivity.

Compared to the simulated results with the original antenna, the simulated/measured gain-reduction levels of building block 1 at 67 and 90 GHz are 31.7/32.8 and 14.2/15.7 dB; while for building block 2 at 67, 78.5, and 90 GHz they are 33.2/25.7, 55.2/31.22 and 16.7/14.8 dB.

Within the passband for  $VSWR < 2$ , the measured cross polarizations of the two building blocks are below  $-28.6$  and  $-25.3$  dB, respectively. The spurious peak around 78.5 GHz of building block 2 may be caused by the system noise.

The simulated and measured results of the radiation patterns are plotted together in Fig. 2.17 and Fig. 2.18. The simulated radiation patterns of the two building blocks at 78.5 GHz are similar to those of the original antenna. The measured radiation patterns at different frequencies agree well with the simulated ones at 78.5 GHz in the first SLL and the 3-dB beamwidth. The measured main-beam directions of the two building blocks are consistently pointing in the boresight direction independent of frequencies, while the maximum first SLL levels and the 3-dB beamwidths at the  $E$ - and  $H$ -planes are  $-24.1$  dB and  $4.3^\circ$ , respectively. No grating lobe is observed. The achieved radiation patterns imply that the expected uniform excitation among the radiating elements is achieved over the bandwidths of interest.

## 2.4 Concluding Remarks

This chapter demonstrates E-band waveguide filters and their integration into a corporate-feed slot array antenna with excellent performance using the commercially available process of diffusion bonding of laminated thin copper plates. It is verified that a high- $Q$  waveguide resonator and low-loss bandpass/bandstop filters at the E-band could be developed by virtue of the mature bonding process presented by diffusion bonding of laminated thin copper plates. The full integration of the proposed filters into the corporate-feed circuit of a  $16 \times 16$ -element slot array antenna combining the radiating and filtering functionalities in one package are validated with high gain and high efficiency.

The feasibility and effectiveness of using empirically derived values to compensate for bonding imperfections in the band-rejection element is also confirmed. The compact and high-performance planar building blocks developed here enable a reliable passive front-end solution for E-band ultra-high capacity point-to-point communications under different operation specifications (single wideband with compatibility over the 76–81-GHz band, and dual narrowbands with suppression over the 76–81-GHz band). The fabrication tolerance equivalent to under-/over-etching is quantitatively explained. A reasonable and adequate agreement between simulations and experiments is evidence that the diffusion bonding of laminated thin copper plates offer a potentially effective E-band waveguide fabrication and packaging solution for batch-processes.

## References

- [2.1] U. Rosenberg, S. Amari, and F. Seyfert, "Pseudo-elliptic direct-coupled resonator filters based on transmission-zero-generating irises," in *Eur. Microw. Conf. Dig.*, pp. 962–965, Sep. 2010.
- [2.2] M. J. Hill, R. W. Ziolkowski, and J. Papapolymerou, "Simulated and measured results from a Duroid-based planar MBG cavity resonator filter," *IEEE Microw. Wireless Compon. Lett.*, vol. 10, no. 12, pp. 528–530, Dec. 2000.
- [2.3] R. J. Cameron, "General coupling matrix synthesis methods for Chebyshev filtering functions," *IEEE Trans. Microw. Theory Techn.*, vol. 47, no. 4, pp. 433–442, Apr. 1999.
- [2.4] S. Amari, "Synthesis of cross-coupled resonator filters using an analytical gradient-based optimization technique," *IEEE Trans. Microw. Theory Techn.*, vol. 48, no. 9, pp. 1559–1564, Sep. 2000.
- [2.5] J.-S. Hong and M. J. Lancaster, *Microstrip Filters for RF/Microwave Applications*. New York: Wiley, 2001.
- [2.6] J. D. Rhodes, "Waveguide bandstop elliptic filters," *IEEE Trans. Microw. Theory Techn.*, vol. MTT-20, pp. 715–718, Nov. 1972.
- [2.7] F. F. He, K. Wu, W. Hong, H. Liang, and X. P. Chen, "Low-cost 60-GHz smart antenna receiver subsystem based on substrate integrated waveguide technology," *IEEE Trans. Microw. Theory Techn.*, vol. 60, no. 4, pp. 1156–1165, Apr. 2012.
- [2.8] Y. Yusuf and X. Gong, "Compact low-loss integration of high-Q 3-D filters with highly efficient antennas," *IEEE Trans. Microw. Theory Techn.*, vol. 59, no. 4, pp. 857–865, Apr. 2011.
- [2.9] Y. Li, P. L. Kirby, and J. Papapolymerou, "Silicon micromachined W-band bandpass filter using DRIE technique," in *Proc. 36th Eur. Microw. Conf.*, pp. 1271–1273, Sep. 2006.



- [2.10] S. Song, C.-S. Yoo, and K.-S. Seo, “W-band bandpass filter using micromachined air-cavity resonator with current probes,” *IEEE Microw. Wireless Compon. Lett.*, vol. 20, no. 4, pp. 205–207, Apr. 2010.
- [2.11] X. Shang, M. Ke, Y. Wang, and M. J. Lancaster, “Micromachined W-band waveguide and filter with two embedded H-plane bends,” *IET Microw. Antennas Propag.*, vol. 5, no. 3, pp. 334–339, Feb. 2011.
- [2.12] C. A. Leal-Sevillano, J. R. Montejo-Garai, M. Ke, M. J. Lancaster, J. A. Ruiz-Cruz, and J. M. Rebollar, “A pseudo-elliptical response filter at W-band fabricated with thick SU-8 photo-resist technology,” *IEEE Microw. Wireless Compon. Lett.*, vol. 22, no. 3, pp. 105–107, Mar. 2012.

## Figures and Tables

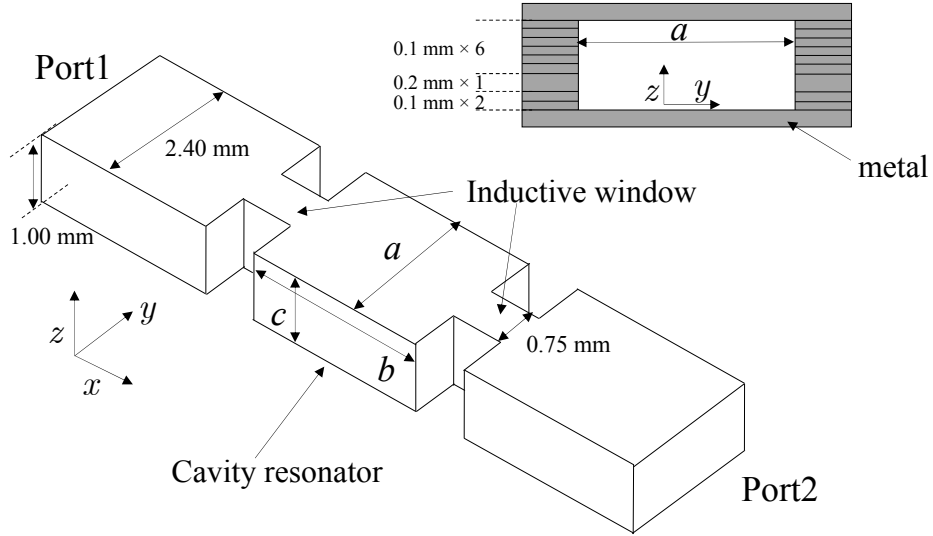


Fig. 2.1 Exploded view of the single cavity resonator and its stacking-arrangement.

TABLE 2.1  
PARTICULARS FOR DIFFERENT METALS<sup>(1)</sup>

	Conduc- tivity in simulation (S/m)	Sim. $Q_u$ by eigen- mode @ 78.48 GHz	Sim. $Q_u$ by two- port model @ 78.49 GHz	Sim. $Q_u$ by two- port model @ 79.07 GHz	Meas. $Q_u$ by two- port model @ 79.07 GHz
Copper	$5.8 \times 10^7$	2224	2261	2348	2121
Stainless steel	$1.5 \times 10^6$	364	N/A	N/A	N/A

(1): The modes here are the TE<sub>101</sub>-modes.

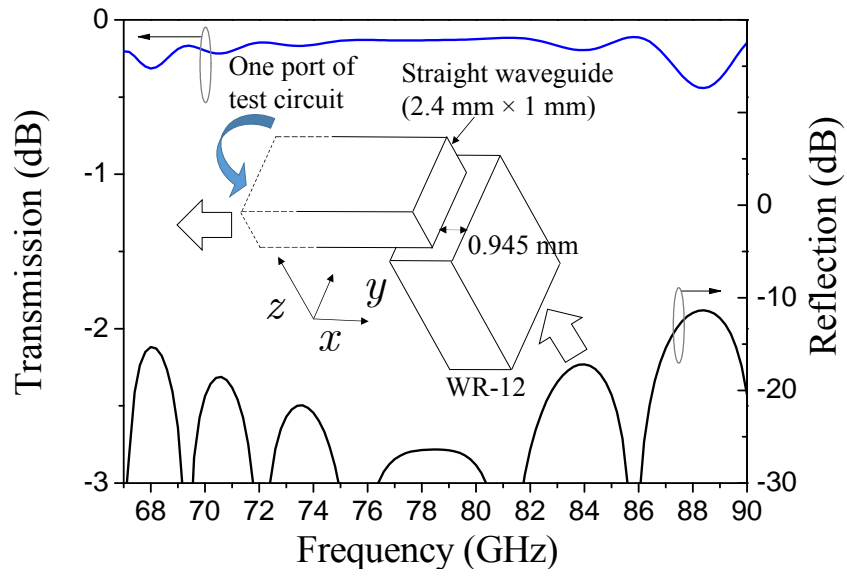


Fig. 2.2 Simulated results of two back-to-back interconnected transitions, with inserted geometry of a single transition.

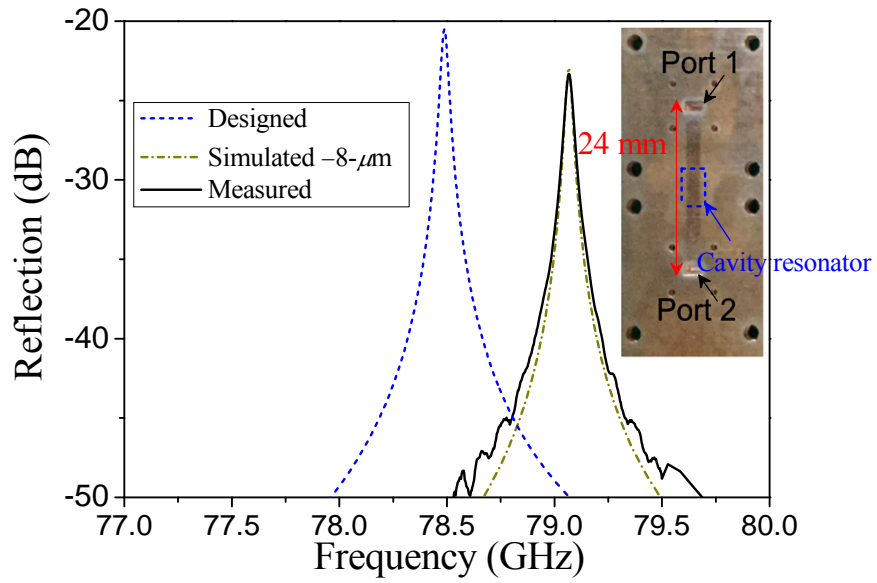
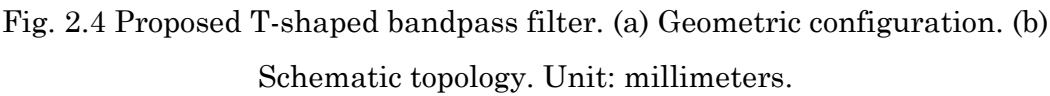


Fig. 2.3 Simulated and measured results of the single cavity with external excitations, with inserted figure of the fabricated prototype.



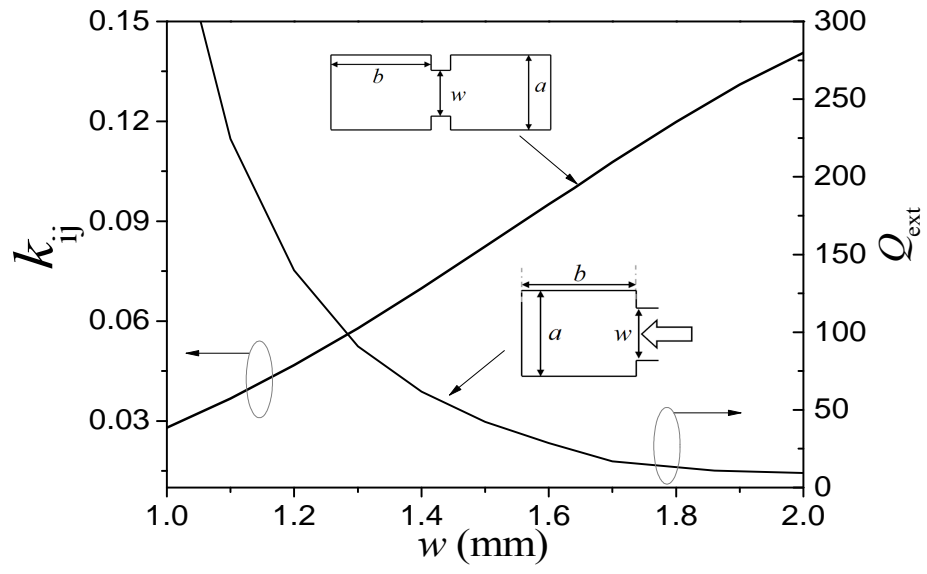
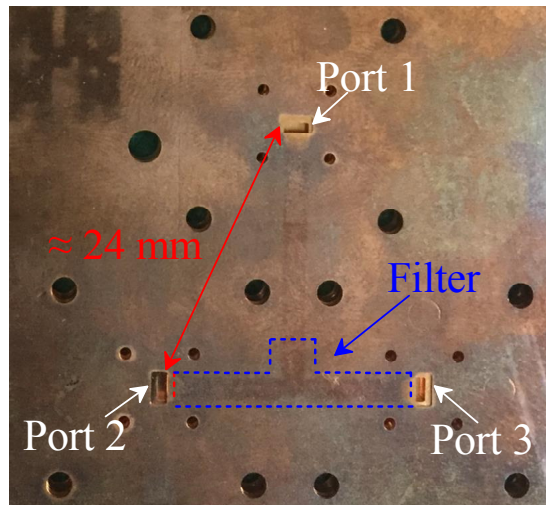
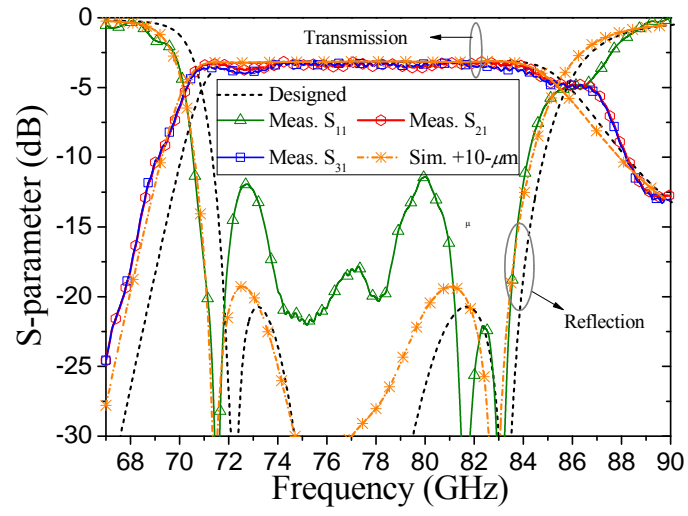


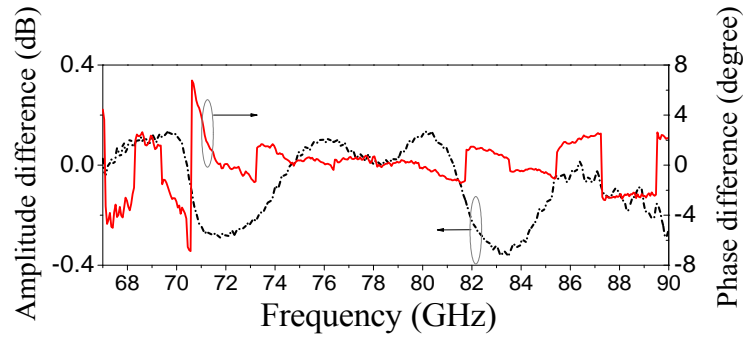
Fig. 2.5 Simulated  $k_{ij}$  and  $Q_{ext}$  as a function of  $w$ .



(a)



(b)

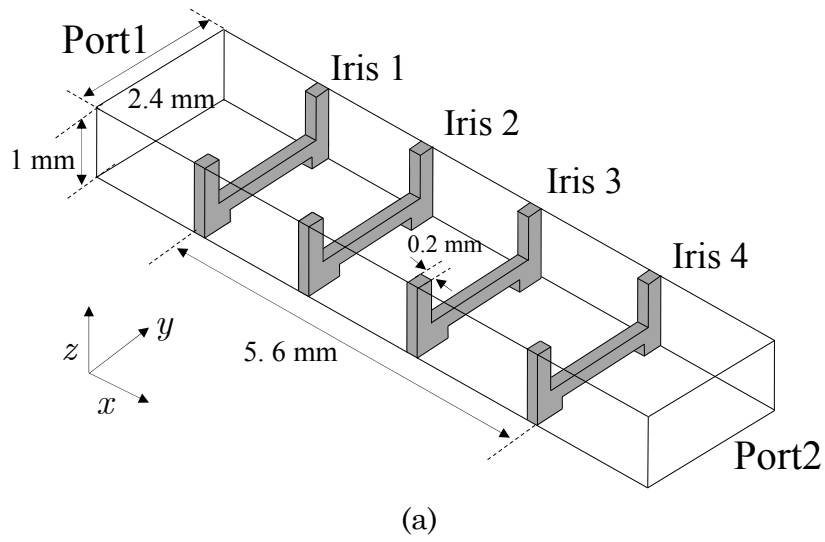


(c)

Fig. 2.6 Proposed T-shaped filter. (a) Photograph of the fabricated prototype. (b) Measured and simulated transmission and reflection characteristics. (c) Measured amplitude and phase differences.

TABLE 2.2  
DETAILS OF OTHER REPORTED WAVEGUIDE CAVITY FILTERS

Ref.	Fabri- cation method	Filtering order/type	Design freq. (GHz)	Meas. 3-dB fractional bandwidth (%)	Meas. minimal insertion loss (dB)
[2.9]	DRIE	3/chebyshev	94.1	4.8	1.1
[2.10]	DRIE	4/chebyshev	94.0	4.9	1.3
[2.11]	SU-8	4/chebyshev	90.0	9.7	1.0
[2.12]	SU-8	4/pseudo- elliptical	100.0	5.0	$\approx 1.2$
This Work	Diffusion bonding	6/chebyshev	78.5	20.5	0.1



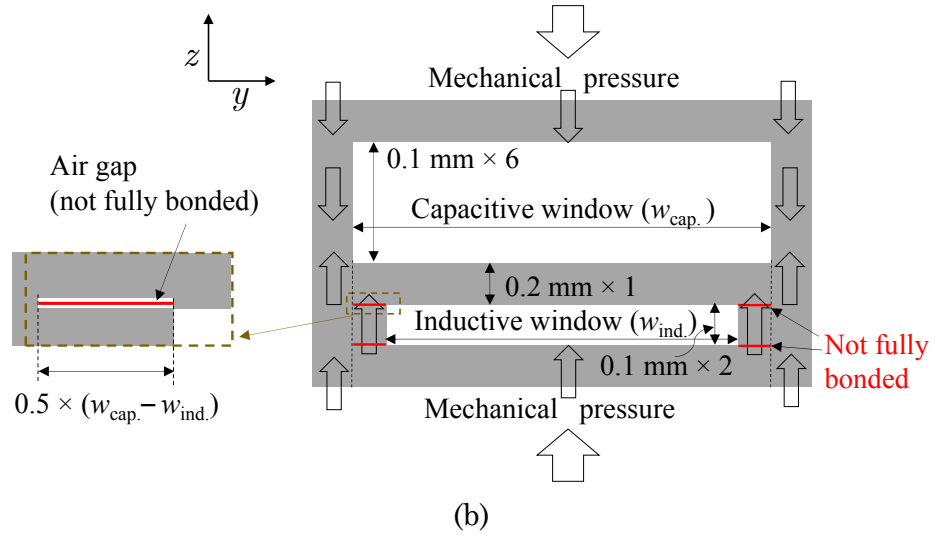


Fig. 2.7 Geometric configurations. (a) Proposed bandstop filter. (b) A single iris.

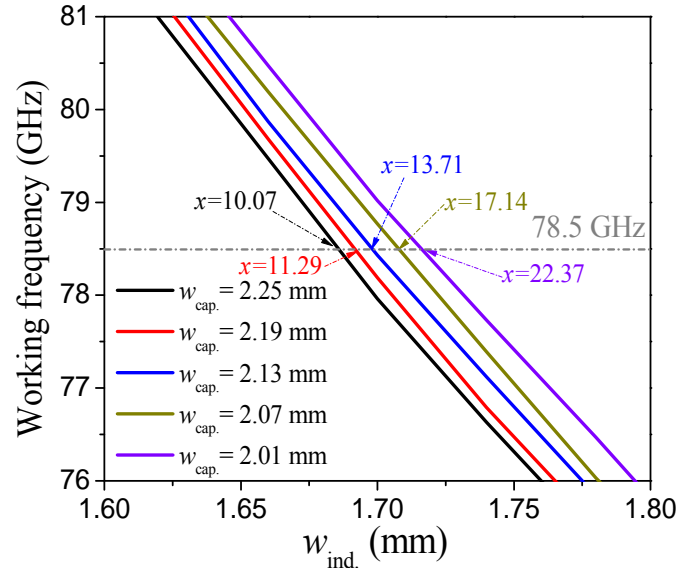


Fig. 2.8 Frequency characteristic of a single iris against the width of the windows.



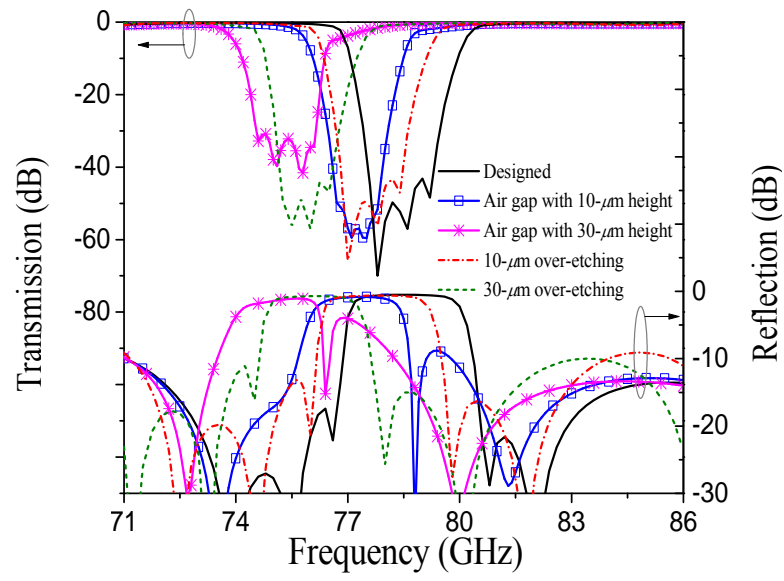
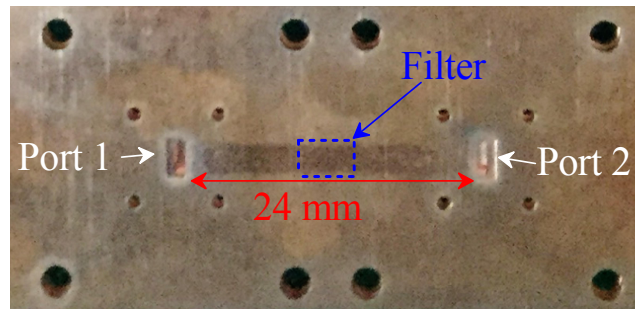
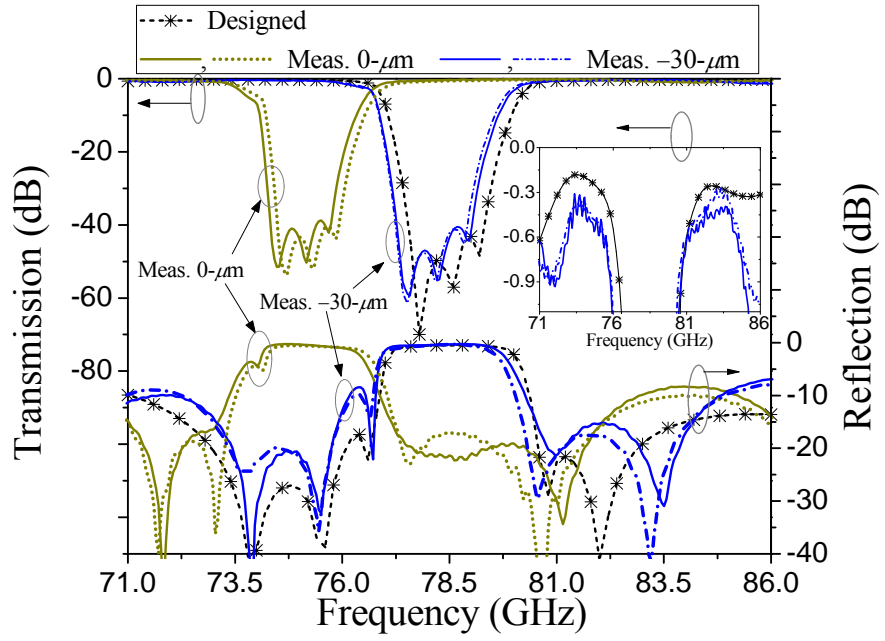


Fig. 2.9 Simulated results of the bandstop filter with over-etching and air gap modes.



(a)



(b)

Fig. 2.10 Proposed bandstop filter. (a) Photograph of one fabricated prototype. (b) Simulated and measured results.

TABLE 2.3  
SUMMARY OF THE SIMULATED AND MEASURED RESULTS

	Etching effect in inherent fab. <sup>(1)</sup> ( $\mu\text{m}$ )	Etching effect in CAD ( $\mu\text{m}$ )	Center freq. (GHz)	Etching effect in freq. shift <sup>(2)</sup> ( $\mu\text{m}$ )	Etching effect in air gap <sup>(3)</sup> ( $\mu\text{m}$ )
Designed	N/A	N/A	78.5	N/A	N/A
Measured 1	+12	0	75.2	+40	+28
Measured 2	+12	0	75.2	+40	+28
Measured 3	+12	-30	78.3	+2	+20
Measured 4	+12	-30	78.3	+2	+20

(1): The etching amount from the inherent fabrication is estimated by the cavity resonator that co-fabricated.

(2): This etching amount is estimated by the frequency shift between the designed and the measured center frequencies.

(3): This etching amount is estimated by the difference in different etching effects.

### 16×16-Element Filter/Antenna Block

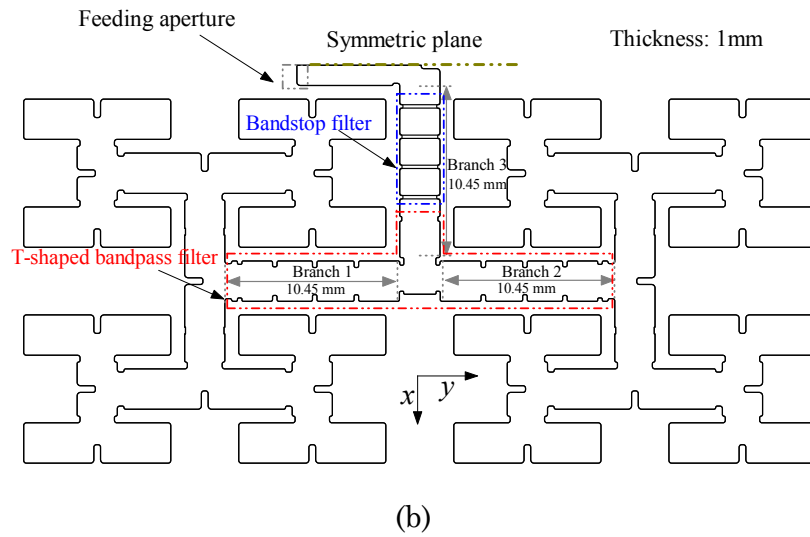
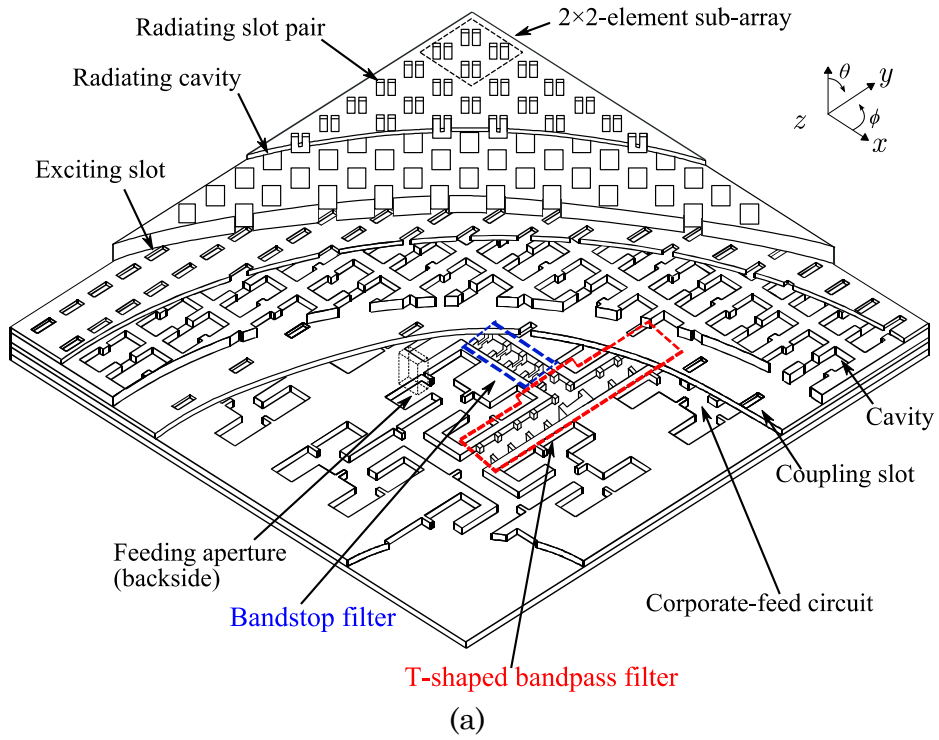


Fig. 2.11 Geometric configuration. (a) Building block 2. (b) Half bisection of the corporate-feed circuit of building block 2.

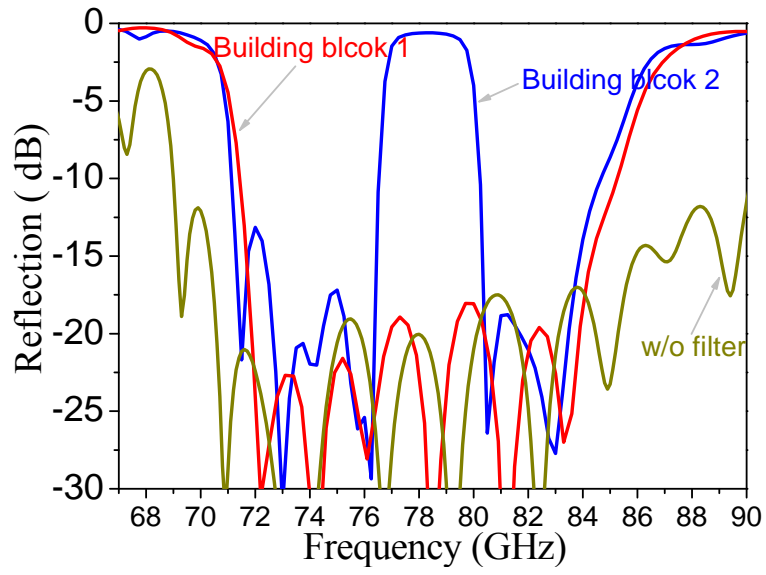


Fig. 2.12 Simulated reflection characteristics.

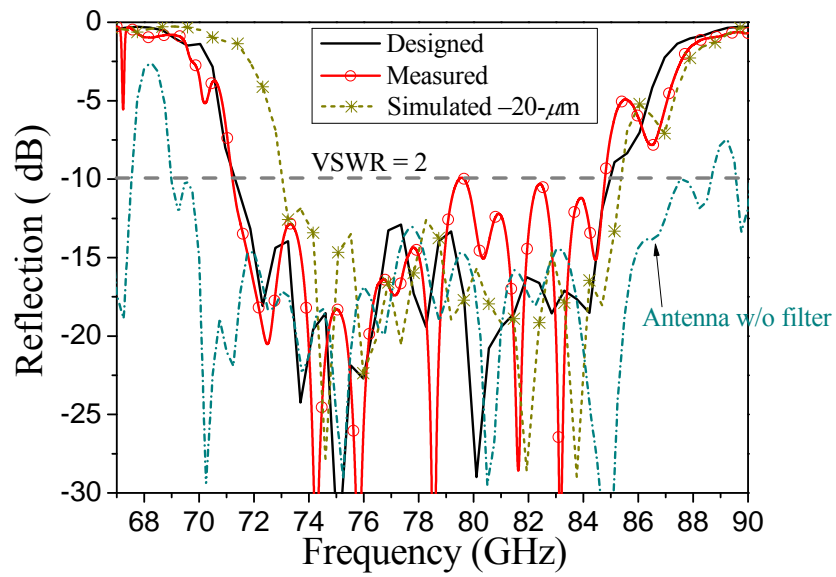
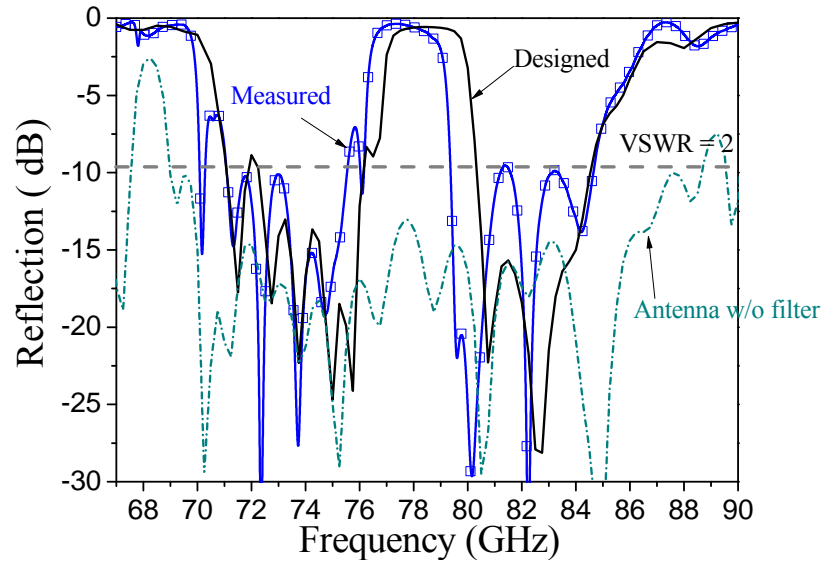
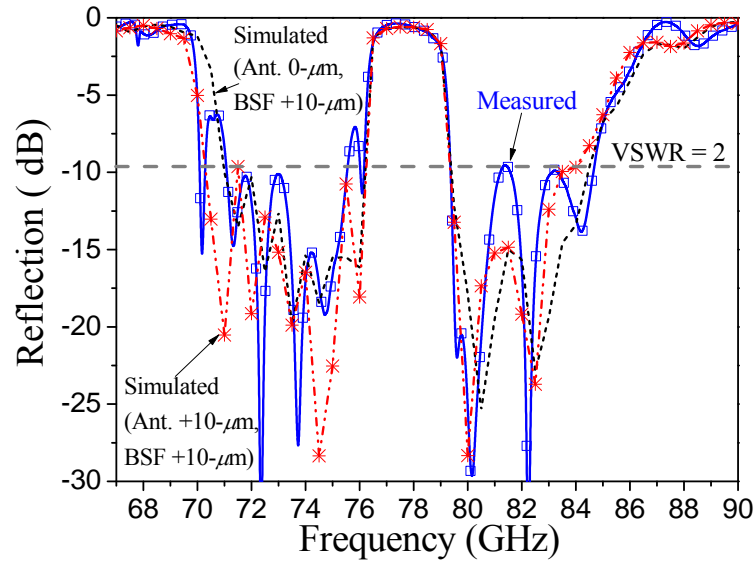


Fig. 2.13 Reflection characteristics of building block 1.

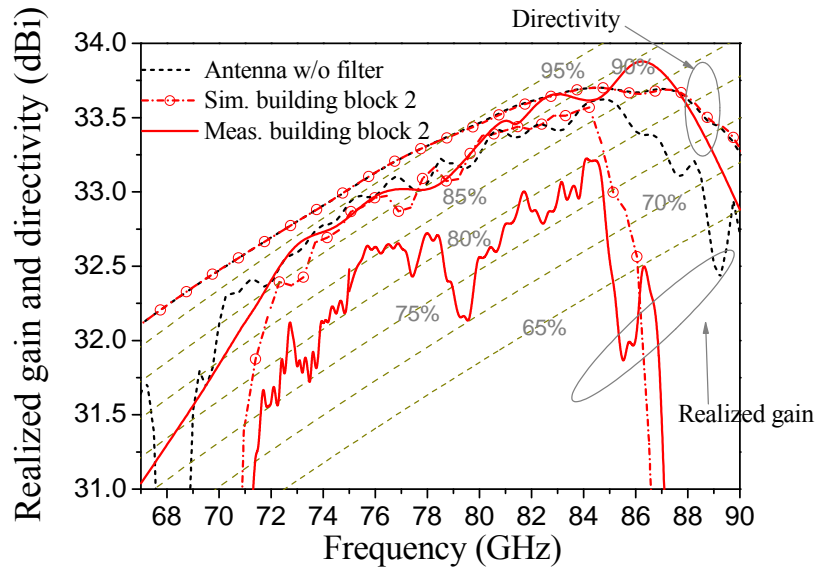


(a)

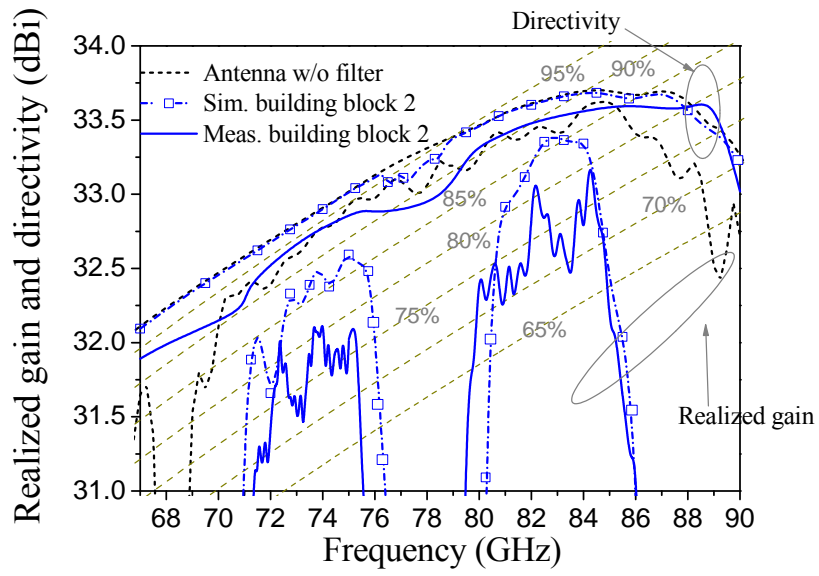


(b)

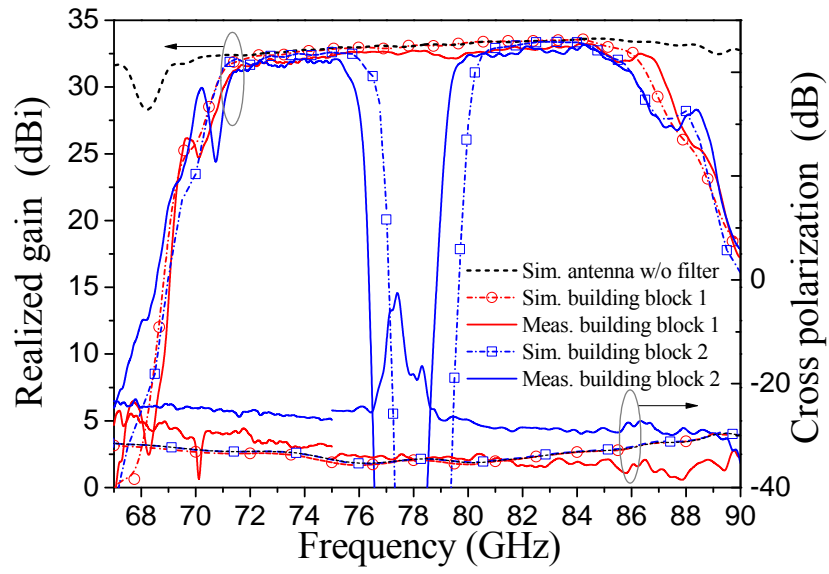
Fig. 2.14 Reflection characteristics of building block 2. (a) Simulated, measured results and (b) tolerance analysis. (BSF stands for the bandstop filter)



(a)



(b)



(c)

Fig. 2.15 Frequency characteristics of realized gain, directivity, and cross polarization. (a), (b) Detail within the passband. (c) Overview.

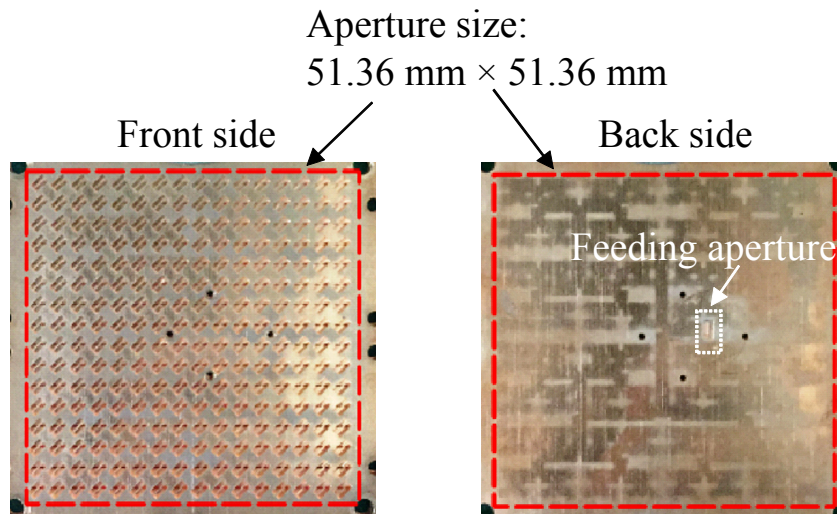


Fig. 2.16 Fabricated prototypes of the two building blocks.



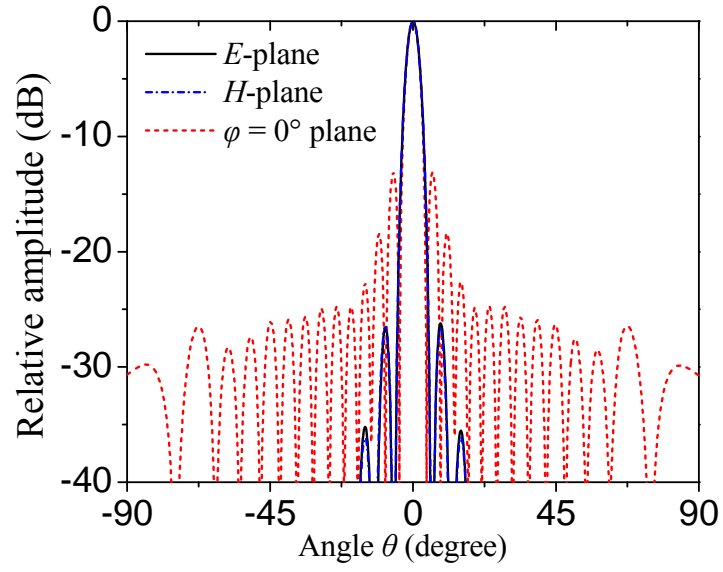
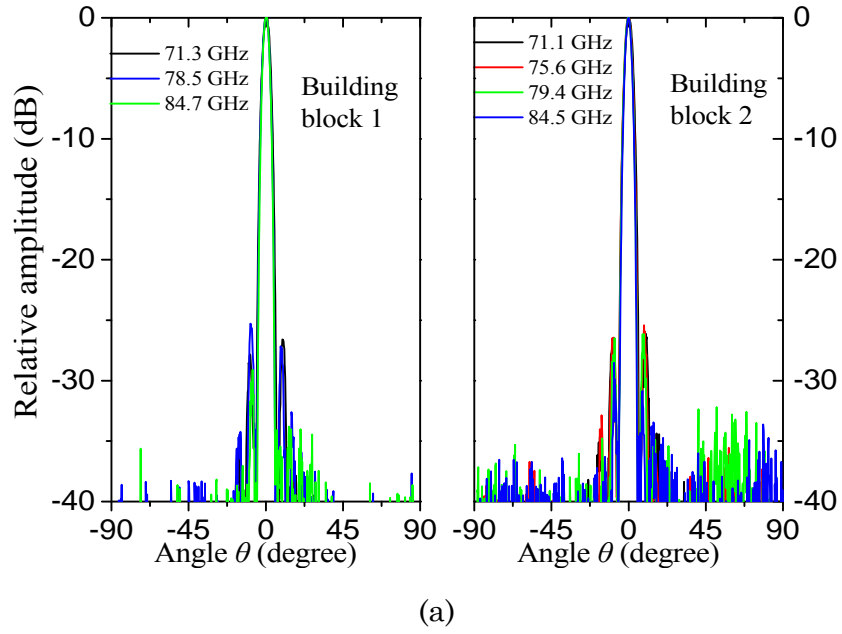
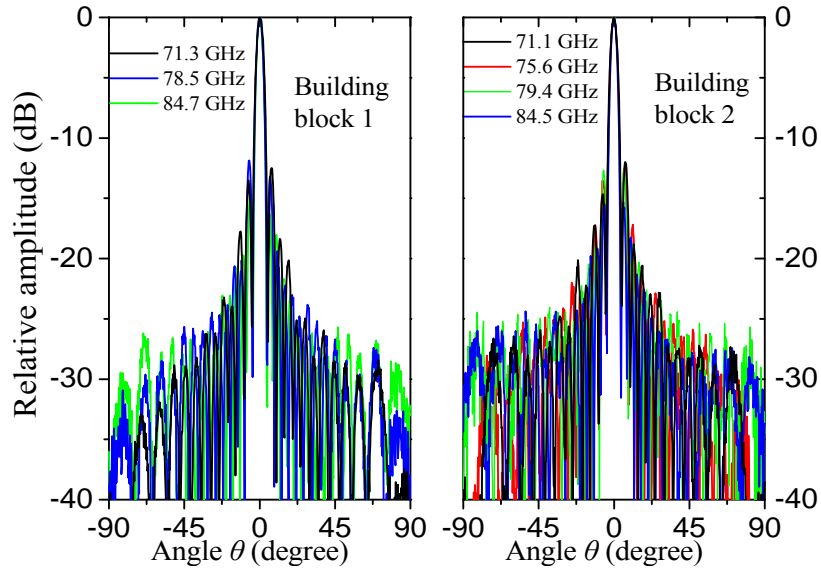


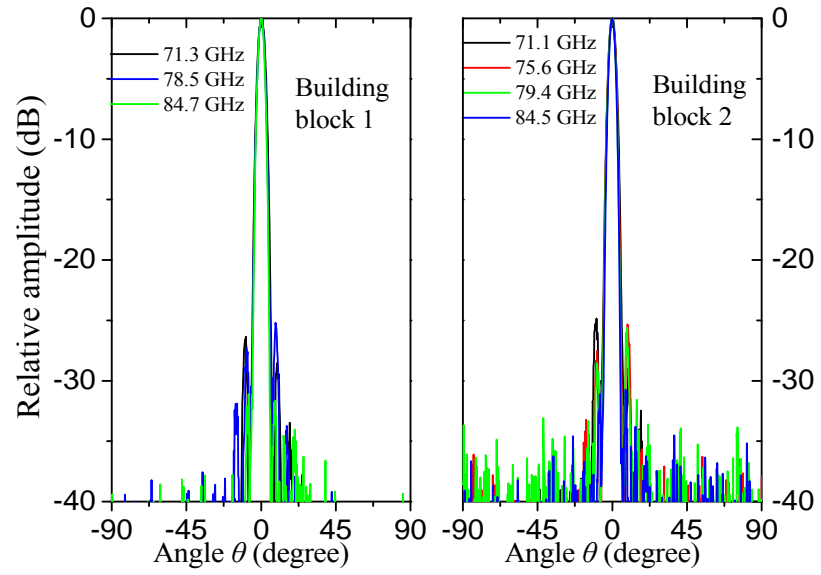
Fig. 2.17 Simulated radiation patterns of the two building blocks at 78.5 GHz.



(a)



(b)



(c)

Fig. 2.18 Measured radiation patterns at different frequencies. (a)  $E$ -plane.  
(b)  $\varphi = 0^\circ$  plane. (c)  $H$ -plane.

# Chapter 3 Incorporation of Monopulse Processing Capability

## 3.1 Introductory Remarks

In this chapter, a  $16 \times 16$ -slot array antenna for the E-band monopulse applications is developed by diffusion bonding of laminated thin metal plates. The antenna is composed of radiating elements, a corporate-feed circuit, and a comparator, which are vertically interconnected. The radiating elements are uniformly fed through the full-corporate-feed circuit. Self-symmetrical magic-T's and their folded counterparts are adopted for implementing a comparator with high isolation, high robustness against fabrication tolerances, as well as frequency-independent amplitude/phase balance. Reflection of each of the sub-components is sufficiently suppressed over a wide bandwidth.

The proposed antenna has been fabricated by diffusion bonding of laminated copper plates, which is a low-cost and mass-producible multi-layer hollow-waveguide fabrication technique. The measured results show that the antenna can work very well over the full E-band.

## 3.2 Antenna Configuration and Operation Mechanism

In the design of monopulse radar system, normally two resolutions, i.e. range resolution and angular resolution are concerned. The range resolution is determined by the bandwidth while the angular resolution is by the antenna directivity. Based on different system specifications such as transmit power, antenna gain, target radar cross section, received power, loss factors and so on, the E-band monopulse radar is attractive for short-to-medium distance (from several meters to several miles) tracking applications such as collision

avoidance and local surveillance/defense. Here, a  $16 \times 16$ -element array antenna is considered in order to achieve a gain and a directivity of larger than 30 dBi.

Fig. 3.1 shows the architecture and the stacking arrangement of the proposed  $16 \times 16$ -element monopulse array antenna. The thickness is 5.8 mm, a laminate of 29 etched metal plates of identical thickness, each 0.2 mm thick. The radiating element, the corporate-feed circuit, and the comparator are formed by 10, 5, and 12 plates, respectively. The dimension of the waveguide employed in the antenna is  $2.4 \text{ mm} \times 1.0 \text{ mm}$ . The design frequency is 78.5 GHz and the design frequency band is from 67 to 90 GHz.

The antenna radiates a wave through the radiating cavities located on the top layer. The  $E$ -plane of the antenna coincides with the  $yz$ -plane ( $90^\circ$ -plane) while the  $H$ -plane coincides with the  $xz$ -plane ( $0^\circ$ -plane). The radiating cavities are spaced at fixed distances in the  $x$ - and  $y$ -directions. The corporate-feed circuit consists of four identical parts with cascaded  $H$ -plane T-, and H-junctions. The 16 coupling slots are arranged between the radiating elements and the corporate-feed circuit, and occur at the end of H-junctions. The  $2 \times 2$ -element subarrays of the radiating elements are uniformly fed by each end of an H-junction through the coupling slot. The comparator with four input ports (Ports 1–4) and four output ports is implemented by four magic-T's. The comparator and the corporate-feed circuit are interconnected through the coupling apertures which are located at the end of the output waveguide of the comparator. The coupling aperture is incorporated by a double-layered interconnecting circuit. The antenna is fed by standard WR-12 waveguides ( $3.10 \text{ mm} \times 1.55 \text{ mm}$ ) from the back through the feeding apertures etched in the bottom plate.

Fig. 3.2 shows a block diagram and the operating mechanism of the antenna. The radiating elements can be viewed as four identical quadrants. Each quadrant represents one  $8 \times 8$ -element subarray and is effected by one

output port of the comparator. The radiating cavities within one quadrant all have the same phase distribution, however the overall phase distribution among the four quadrants can be controlled by the phase transformation over the difference/sum ports of these magic-T's. When Port 1 is excited, the sum beam is generated; when Port 2 or 4 is excited, the difference beam is generated in the  $E$ -plane or  $H$ -plane, respectively; when Port 3 is excited, the difference beams in the cross-planes ( $45^\circ$ - and  $135^\circ$ -planes) are generated.

The commercial software HFSS 14 and 16 were used to perform the simulations conducted here, and copper with a conductivity of  $5.8 \times 10^7$  S/m is used throughout the simulations.

### 3.3 Design of the Building Blocks

#### 3.3.1 Radiating Element

We developed a wideband  $2 \times 2$ -element subarray in the E-band [1.28],  $45^\circ$  polarized to maintain a low side-lobe level at its co-polarization plane, which however cannot coincide with the plane for the monopulse operation considered here. Further, the rotation of the radiating cavity will unavoidably degrade the cross-polarization level.

Based on the above considerations, we propose a  $2 \times 2$ -element with  $0^\circ$  polarization suitable for the monopulse operation considered here which is able to maintain a satisfactory radiation performance, as shown in Fig. 3.3. It is composed of one coupling slot, one cavity, four narrow exciting slots, and four  $0^\circ$  polarized radiating cavities, occupying four etching patterns. The narrow exciting slot between the radiating cavity and the cavity is aimed at suppressing the grating lobe generated by the wide radiating cavity.

The distance between two adjacent radiating cavities is set to 3.18 mm ( $0.83 \lambda_0$  at 78.5 GHz). Two pairs of walls with periodic boundary conditions are imposed above the radiating cavities to take the mutual

coupling effect from adjacent subarrays into account. In addition, the array-setup functionality is used to predict the radiation characteristics of the array antenna. The design parameters have been fully tuned to broaden the operation bandwidth. The final design parameters are listed in Table 3.1.

Fig. 3.4 shows the calculated amplitude and phase distributions of the  $E_x$  along center line of the slot pair at 78.5 GHz. It can be found that in the traditional mode scaled from [3.1], there is 4.7-dB amplitude difference and  $32.8^\circ$  phase difference at the edge of each slot. Fig. 3.5 shows the calculated  $E$ -plane radiation pattern of the subarray with array-setup functionality. Granting lobes of  $-15.4$  dB peaking at  $\pm 37.1^\circ$  can be observed due to the non-uniformity field distribution. On the other hand, in the proposed model, the amplitude and phase distributions in each slot are more symmetric with respect to the edge. The amplitude and phase differences at the edge of each slot are remarkably suppressed to approximately 0.35 dB and  $0.1^\circ$ , respectively. The grating lobes have been suppressed to an unappreciable level. In addition, the aperture efficiency has been enhanced by 8.8%, from 90.4% to 99.2%.

Fig. 3.6 shows the simulated reflection and cross polarization of the proposed  $2 \times 2$ -element subarray. At 67–90 GHz, a wide bandwidth for impedance matching is achieved, 21.8% for  $VSWR < 1.5$  with the poorest local value of  $-19.6$  dB. The cross polarization at the boresight within the design frequency band is below  $-64$  dB, showing a promising enhancement compared to that in [3.1], where additional narrow slot pairs were adopted.

### 3.3.2 Corporate-Feed Circuit

Fig. 3.7 shows a half bisection of a quarter of the corporate-feed circuit. It occupies one etching pattern, and is obtained by scaling down the  $H$ -plane T-, and H-junctions presented in [3.1]. However, improvements of the design

have been made on the H-junction by introducing a cancelling iris, which is approximately a quarter of the guided wavelength away from the window, as indicated in Fig. 3.7. In this situation, the reflection from the window can be further reduced by cancelling with the reflection from the iris due to the  $180^\circ$  phase difference.

Fig. 3.8 shows the reflection characteristics of the junctions and the corporate-feed circuit. The bandwidth of the T-junction for reflection  $< -20$  dB is 27.2%. The bandwidth of the H-junction for reflection  $< -20$  dB has been improved from 20.5% to 23.1% with the cancelling iris, and the poorest local value from  $-22.7$  to  $-30.6$  dB. Consequently, the bandwidth of the corporate-feed circuit for reflection  $< -20$  dB has been improved from 18.5% to 22.1%, with the poorest local value from  $-21.1$  to  $-25.4$  dB.

### 3.3.3 Comparator

The magic-T is a critical component of the comparator, therefore the stability and practicality of the magic-T from the standpoint of fabrication is the starting point for the design. The magic-T's presented in [3.2–5] have an important feature in common in that they all adopt a scheme with T-shaped junctions, and the matching elements formed by wedge, post, cone, iris and other features are centered inside the junction. However, in the fabrication process using diffusion bonding of laminated thin metal plates, the top surface of these matching elements must be free from mechanical pressure due to the E-plane waveguide branch above, and the result may be imperfect bonding [3.6] due to the low (absent) pressure, resulting in deformations and air gaps between the plates forming the matching element. Here, the Y-shaped junction is considered to ensure fabrication stability.

Fig. 3.9 shows the geometry and the stacking arrangement of the proposed comparator, which is a double-layered structure incorporating four

etching patterns. The thickness of each layer is 1 mm, the coupling/feed apertures and coupling slots are positioned in the middle and bottom plates. The comparator is implemented by four magic-T's, two of which are denoted as (A) and two as (B). The difference and sum ports of the (A) magic-T's serve as the input ports of the comparator; while the ports of (B) magic-T's for power-dividing serve as the output ports of the comparator and are coupled with the corporate-feed circuit. To connect the external WR-12 waveguide, the *H*-arms of the (A) magic-T's are extended by E-bends. Several L-shaped waveguides are employed for the transition. To accommodate the waveguide flanges in the measurements, the distance between adjacent feeding apertures is selected to be larger than 20 mm.

Fig. 3.10 shows the geometry and simulated reflection characteristic of the E-bend. With principles similar to those presented in the previous subsection, the E-bend with the newly introduced cancelling irises show a greatly improved bandwidth for reflection  $< -25$  dB, i.e. 19.4% (70.8–86 GHz) compared the traditional E-bend [3.1].

Fig. 3.11 shows the geometry and the frequency characteristic of the magic-T's. A (A) magic-T consists of an *H*-plane junction and an *E*-plane junction, and the shared junction is formed by a Y-shaped bifurcation. The shape of the impedance-transformer at the junction is crucial for matching the *E*- and *H*-arms simultaneously, while many irises are also added for further tuning the impedance matching. The *E*- and *H*-arms of the (A) magic-T are mutually perpendicular, and have centerlines in one symmetry plane of the junction. The coupling aperture is arranged between the *E*-arm and the junction. Such self-symmetry guarantees a perfect isolation between the sum and difference ports and the desired phase difference between the two output ports. The power-dividing arms after the junction are rotated by  $90^\circ$  to facilitate the interconnection between the magic-T's.

To achieve structural compactness and simplification, the (B) magic-



T used in the comparator is obtained by folding the  $E$ -arm of the above (A) magic-T toward the lower layer, with a transverse coupling slot etched in the middle plate. In this way, the  $E$ -arms of the (B) magic-T's and the power-dividing arms of the (A) magic-T can be placed in the same layer, and interconnected through L-shaped waveguides without a vertical transition, avoiding an increase in thickness and number of etched patterns.

No rigorous theoretical treatments represented with an equivalent circuit as a starting point would be directly applicable to the design of such waveguide hybrid junctions. But the design problem can be reduced to that of maintaining symmetry and simultaneously suppressing the reflection from the  $E$ - and  $H$ -arms by electromagnetic-based optimization [3.2–5]. All the design parameters indicated in Fig. 3.11(a) have been fully optimized to broaden the bandwidth and the final values are listed in Table 3.2. As shown in Fig. 3.11(b), the bandwidth of the sum ports for reflection  $< -20$  dB is 19.1% (70.9–85.9 GHz); while that of the difference ports is 21.8% (69.8–86.9 GHz). The isolation of the (A) and (B) magic-T are better than 45 and 60 dB, respectively.

In magic-T (B), the folded placement of the  $E$ -arm leads to the mismatch of the centerlines between the  $E$ - and  $H$ -arms. Such mismatch will degrade the structural symmetry, which is crucial to the isolation and amplitude/phase balance characteristics of the magic-T. Therefore, the coupling slot should be narrow enough to remedy the effect caused by the aforementioned mismatch. Fig. 3.12 shows the simulated result of the parametric study on the width of the coupling slot with regards to the bandwidth, amplitude/phase difference, and isolation. It can be found that the bandwidth will gradually raise with the increase of the width of coupling slot until reaching its peak value, and then constantly decreases. On the other hand, in principle, the narrower width of the coupling slot can bring out higher isolation level and smaller amplitude/phase difference. In other words,

a trade-off should be made among above specifications when determining the width of the coupling slot. Nevertheless, regardless of the variation of the bandwidth, the isolation and amplitude/phase difference can be kept to a quite satisfactory level over an appreciable range of slot width.

Fig. 3.13(a) shows the simulated reflection characteristics of the comparator (including the E-bends and the L-shaped transitions). The bandwidth of the input ports for  $VSWR < 1.5$  is 21.1% (70.6–87.2 GHz).

Fig. 3.13(b) shows the simulated amplitude/phase error of the comparator. The amplitude error for one of the input ports is defined as the difference between the maximum and the minimum amplitudes among all the output ports. The phase error for one of the input ports is defined as the difference between the ideal and the average of the phase difference between adjacent output ports. The simulated amplitude and phase errors across 67–90 GHz are small to negligible, less than 0.1 dB and  $0.2^\circ$ , respectively. From this it may be concluded that a frequency-independent monopulse processing capability of the comparator has been successfully implemented.

In the fabrication process of diffusion bonding of laminated thin metal plates, errors mainly arise due to the etching and laminating processes, and may be considered to be a result of over-etching, something which is practically within the extent of 0–30  $\mu\text{m}$ . Including the effect of the worst case by imposing 30- $\mu\text{m}$  of over-etching on all the design parameters of the comparator, results in the simulated results shown in Fig. 3.13(b). With this imposed error, amplitude and phase errors are nearly unchanged, suggesting the inherent robustness of the comparator against fabrication errors.

### **3.4 Antenna Implementation and Simulated Results**

For the antenna, the proposed building blocks are integrated to create a  $16 \times$

16-slot array antenna, and a problem here is the interconnection between the corporate-feed and the comparator. To avoid overlap between the corporate-feed circuit and the comparator in co-plane interconnection, here we adopt a double-layered interconnecting circuit formed by adding a pair of cancelling irises to the one proposed in [1.29].

Fig. 3.14 shows the geometry and the simulated result of the adopted double-layer interconnecting circuit. The bandwidth for reflection  $< -25$  dB is 21.4% (70.5–87.3 GHz), which is a great improvement compared to the traditional circuit [1.29].

Fig. 3.15 shows the simulated reflection characteristic of the antenna. The bandwidth for VSWR  $< 2$  at the both input ports is 21.8% (69.4–86.5 GHz).

Fig. 3.16 shows the simulated realized gain, the directivity, and the cross polarization of the sum beam (Port 1) at the boresight. At the design frequency of 78.5 GHz, the simulated realized gain and directivity are 32.8 and 33.3 dBi, making the corresponding antenna efficiency and aperture efficiency 86% and 95% for the 50.88 mm  $\times$  50.88 mm aperture size. The cross polarization within the design frequency band is below  $-67$  dB.

### 3.5 Experimental Results

The proposed antenna was fabricated by diffusion bonding of laminated thin copper plates, and a photo-graph of the fabricated prototype is shown in Fig. 3.17. The antenna is composed of ten etching patterns and the plates are 74 mm  $\times$  74 mm  $\times$  0.2 mm. The total antenna dimension is 50.88 mm  $\times$  50.88 mm  $\times$  5.8 mm ( $13.31 \lambda_0 \times 13.31 \lambda_0 \times 1.52 \lambda_0$  at 78.5 GHz). Note that the through holes in the antenna prototype are used for screws in interconnecting the jig and the test system.

In the measurements, the unused ports are terminated with E-band matching loads. The far-field measurement is carried out by two test systems

which operate in the V-band (67–75 GHz) and the W-band (75–90 GHz), respectively.

### 3.5.1 Reflection and Isolation

Fig. 3.18 shows the measured reflection and isolation characteristics of the antenna. The antenna exhibits a wide bandwidth for the impedance matching and also a high isolation level. The measured bandwidth of both input ports for  $VSWR < 2$  is 21.9 % (70.0–87.2 GHz), matching well with its simulated counterpart. The measured reflection is slightly degraded in comparison with the simulated one. However, the wide bandwidth for  $VSWR < 2$  is confirmed in the measurement. The discrepancy between the simulated and measured reflection characteristics can be mainly attributed to the fabricated tolerance and the parasitic effect from the jig used for interconnecting the antenna and the test system.

Within this bandwidth, the isolation between two of the input ports are better than 33.5 dB. To facilitate the characterization, the bandwidth of both input ports for  $VSWR < 2$  is defined as the band of operation of the antenna here.

### 3.5.2 Realized Gain, Directivity, and Loss Evaluation

The measured realized gain and directivity of the sum beam at the boresight are added in Fig. 3.16. At the design frequency of 78.5 GHz, the realized gain and directivity are 32.6 and 33.3 dBi, which correspond to antenna and aperture efficiencies of 83% and 95%, respectively. The bandwidth for 1-dB gain down with respect to 78.5 GHz is 19.2% (72.9–88.0 GHz). Across the operation band, an antenna efficiency  $> 73\%$  and an aperture efficiency  $> 89\%$

are fully supported. Across the operation band, the cross polarization is verified to be below  $-44.2$  dB.

Within the operation band, the discrepancy between the measured realized gain and its simulated counterpart is mainly caused by the discrepancy between the measured and simulated reflection characteristics, as well as by the parasitic loss from the jig and the waveguide connectors used for interconnecting the antenna and the test system. This parasitic loss cannot be fully de-imbedded in measurement and it is roughly estimated to be less than as between  $0$ – $0.2$  dB within the operation band.

Fig. 3.19 shows the simulated and measured antenna losses which are estimated by the difference between the directivity and the realized gain while excluding the mismatching loss. Therefore, the simulated antenna loss is identical to the simulated conductor loss, while the measured antenna loss also includes the error in measurement and the leakage loss caused by the bonding imperfection. At  $78.5$  GHz, the simulated and measured losses are  $0.43$  and  $0.39$  dB. Across the operation band, the measured loss is smaller than  $0.85$  dB. The reasonable agreement between the simulated and measured results is evidence of the outstanding fabrication quality in terms of the surface roughness and the electric contact among the plates.

### 3.5.3 Radiation Pattern

Fig. 3.20 shows the simulated and measured radiation patterns at  $78.5$  GHz. At  $78.5$  GHz, the measured first SLL of the sum beam in the  $E$ -,  $H$ -,  $45^\circ$ -, and  $135^\circ$  planes are  $-13.3$ ,  $-13.4$ ,  $-27$ , and  $-26.5$  dB, with a 3-dB beamwidth of  $3.95^\circ$ ,  $3.85^\circ$ ,  $3.93^\circ$ , and  $3.92^\circ$ , respectively. For the difference beams, the measured amplitude differences in the  $E$ -,  $H$ -,  $45^\circ$ -, and  $135^\circ$ -planes are  $0.22$ ,  $0.12$ ,  $0.02$ , and  $0.12$  dB, with the high null depth level of  $-53.0$ ,  $-58.0$ ,  $-57.8$ , and  $-65.6$  dB, respectively. The amplitude differences of the peak gain

between the sum and difference beams in each plane are detailed in Table 3.3. It shows that in the  $E$ - and  $H$ -planes, there is an approximately 3-dB difference in the measured peak gain between the respective sum and difference beams. Similarly, in the  $45^\circ$ - and  $135^\circ$ -planes, there is an approximately 6-dB difference in the measured peak gain between the respective sum and difference beams. This suggests that high gain and high efficiency are also achieved for the difference beams.

Fig. 3.21 shows the measured radiation patterns at different frequency points across the operation band. Here, the main-beam of the sum beam and the null of the difference beams are consistently pointing at the boresight.

Fig. 3.22 shows details of the measured results in different planes across the operation band. The 3-dB beamwidth of the sum beam in both planes is from  $3.4^\circ$  to  $4.0^\circ$ . The SLL of the sum beam in the  $E$ -,  $H$ -,  $45^\circ$ -, and  $135^\circ$  planes are better than -12.5, -12.7, -25.6, and -26.1 dB, respectively, with no grating lobes observed. Besides, the amplitude difference in the  $E$ -,  $H$ -,  $45^\circ$ -, and  $135^\circ$ -planes are less than 0.28, 0.26, 0.37, and 0.18 dB, with the null depth lower than -51.4, -52.0, -55.3, and -51.6 dB, respectively.

Table 3.4 summaries the comparison with other related works at the design frequency. Note that in [1.47] the value of efficiency was given however the type of efficiency such as radiation efficiency, aperture efficiency, and antenna efficiency as well as the antenna size for the efficiency estimation was not given. As shown, the proposed antenna here has a quasi-planar profile that ease of practical integration. The proposed antenna shows dramatic performance improvements in terms of operation bandwidth and null depth level. The proposed antenna also shows an encouragingly high antenna efficiency given such high operation frequency and complicated architecture.

### 3.6 Concluding Remarks

In this chapter, an E-band plate-laminated  $16 \times 16$ -slot full-corporate-feed waveguide monopulse array antenna with compact size and low profile has been successfully demonstrated. The multi-layer architecture greatly facilitates the component design and interconnections, enabling a compact overall size and low losses. A stable radiation performance with excellent monopulse capabilities independent of the frequency is achieved by the well-designed sub-components associated with the full-corporate-feed architecture here.

The antenna demonstrates a wide operation bandwidth covering the full E-band with high isolation, high gain, high efficiency, and low cross polarization. Across the operation band, the antenna also demonstrates excellent monopulse capabilities with a narrow pencil beam and high null depth level. The antenna is promising and attractive for short-to-medium distance monopulse tracking radar applications with ultra-high range-resolution and high data-rate capabilities.

## References

- [3.1] Y. Miura, J. Hirokawa, M. Ando, Y. Shibuya, and G. Yoshida, "Double-layer full-corporate-feed hollow-waveguide slot array antenna in the 60GHz-band," *IEEE Trans. Antennas Propag.*, vol. 59, no.8, pp. 2844–2851, Aug. 2011.
- [3.2] K. C. Hwang, "Design and optimization of a broadband waveguide magic-T using a stepped conducting cone," *IEEE Microw. Wireless Compon. Lett.*, vol. 19, no. 9, pp. 539–541, Sep. 2009.
- [3.3] C. A. Leal-Sevillano, J. A. Ruiz-Cruz, J. R. Montejo-Garai, and J. M. Rebollar, "Compact broadband couplers based on the waveguide magic-T junction," in *IEEE MTT-S Int. Microw. Symp. Dig.*, pp. 151–154, Oct. 2013.
- [3.4] W. Kahn, "E-plane forked hybrid-T junction," *IRE Trans. Microw. Theory Techn.*, vol. MTT-3, no. 6, pp. 52–58, Dec. 1955.
- [3.5] A. A. San Blas, F. Mira, V. E. Boria, B. Gimeno, M. Bressan, and P. Arcioni, "On the fast and rigorous analysis of compensated waveguide junctions using off-centered partial-height metallic posts," *IEEE Trans. Microw. Theory Techn.*, vol. 55, no. 1, pp. 168–175, Jan. 2007.
- [3.6] X. Xu, J. Hirokawa, and M. Ando, "A waveguide slot array antenna with integrated T-shaped filters in the corporate-feed circuit," in *Proc. of International Symposium on Antennas and Propagation (ISAP)*, Session S3.1.2, pp.45–46, Nov. 2015.



## Figures and Tables

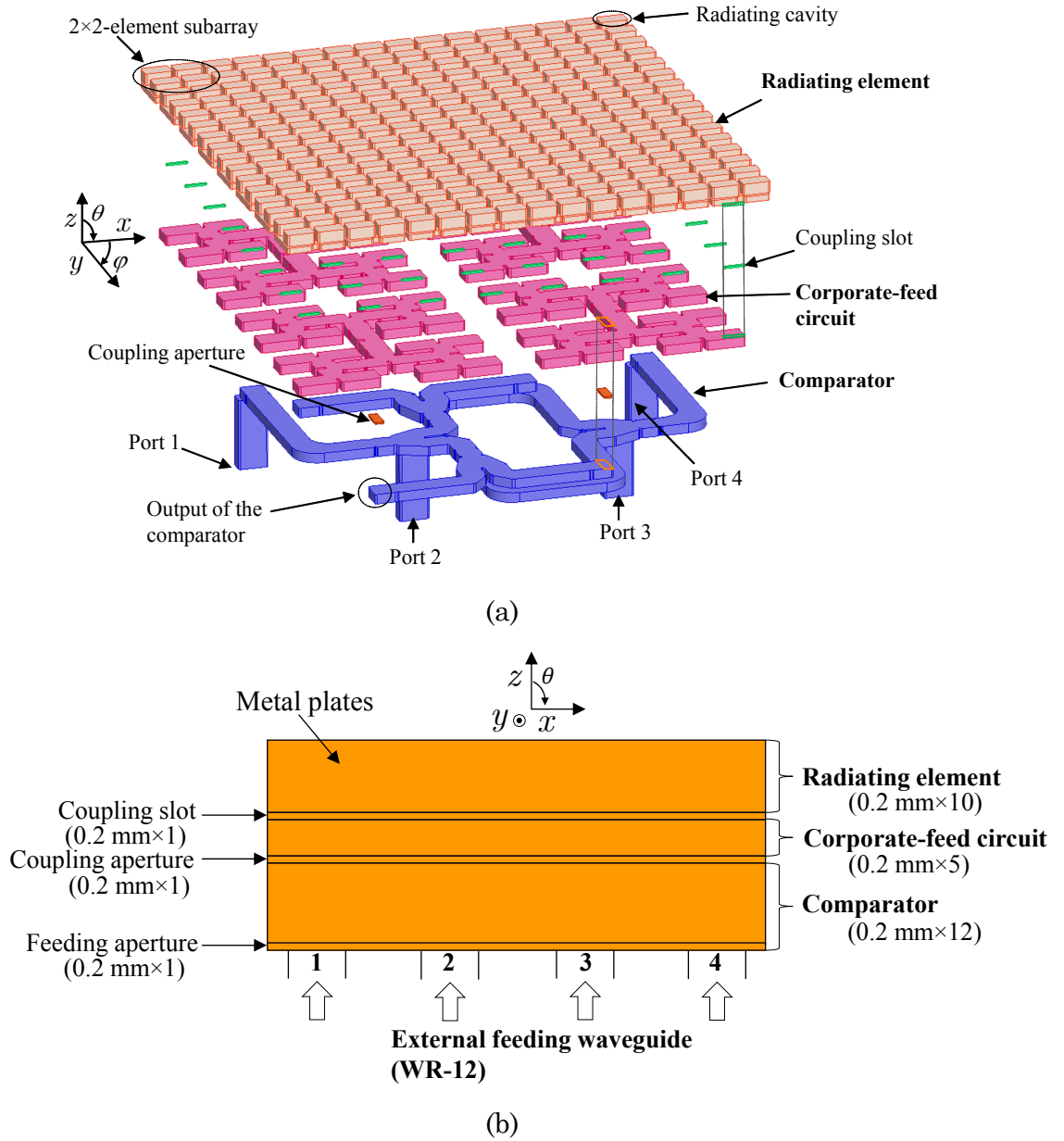
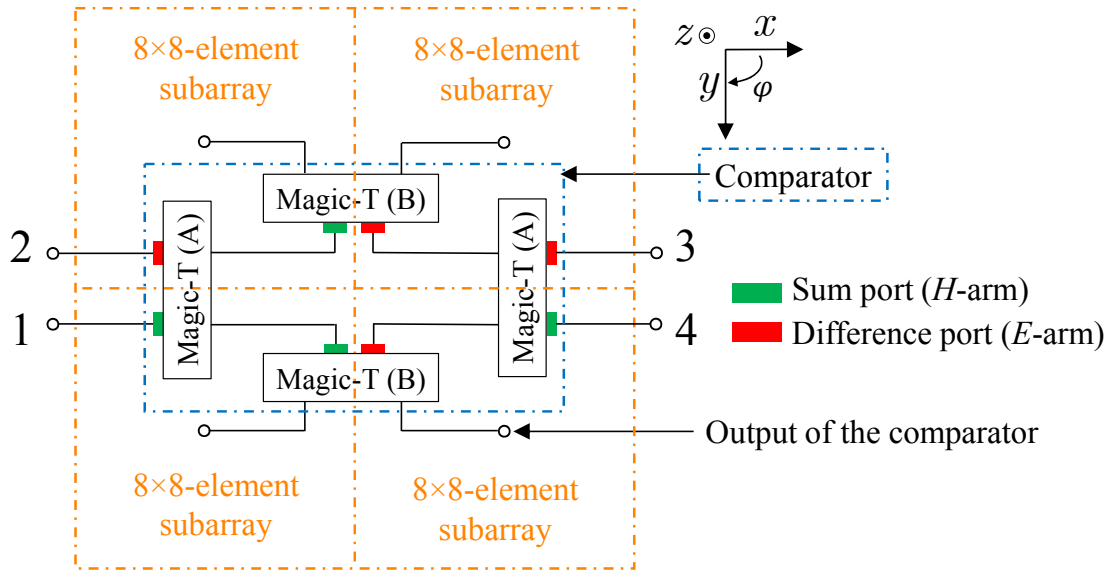
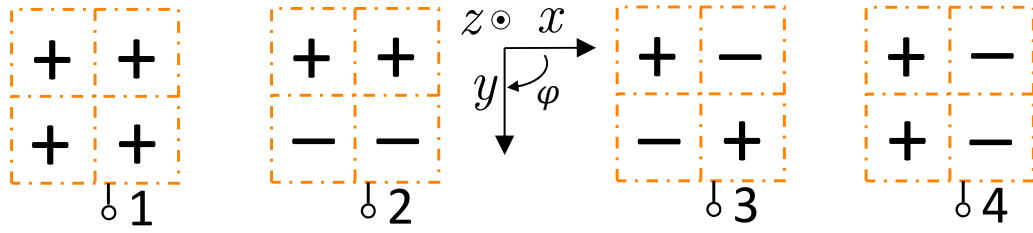


Fig. 3.1 Proposed  $16 \times 16$ -element monopulse array antenna. (a) Architecture. (b) Stacking arrangement.



(a)



(b)

Fig. 3.2 Proposed  $16 \times 16$ -element monopulse array antenna. (a) Block diagram. (b) Operating mechanism.

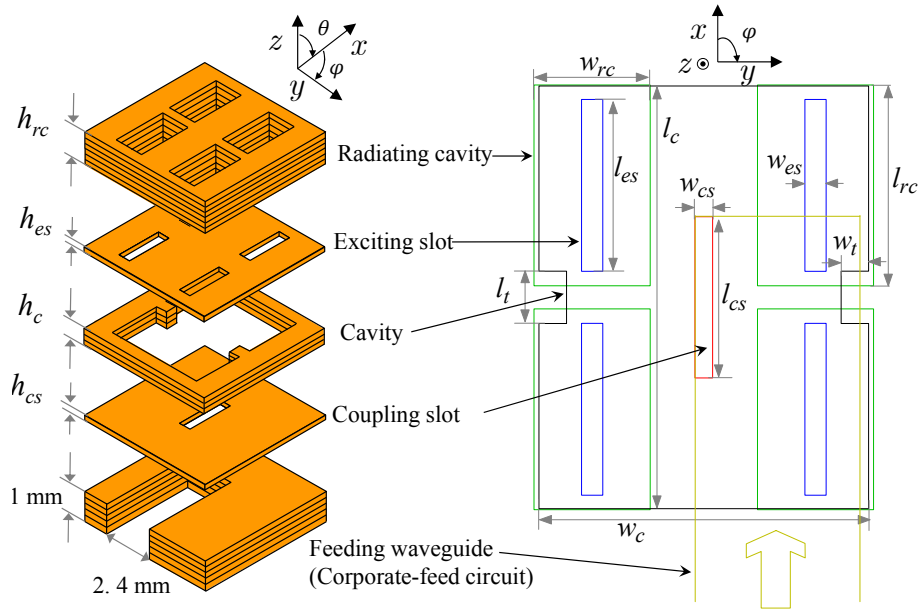


Fig. 3.3 Architecture of the proposed  $2 \times 2$ -element subarrays.

TABLE 3.1  
DESIGN PARAMETERS OF A  $2 \times 2$ -ELEMENT SUBARRAY

Design parameters		Value (mm)
Distance between adjacent radiating cavities	\	3.18
Thickness of the radiating cavity	$h_{rc}$	1.20
Thickness of the exciting slot	$h_{es}$	0.20
Thickness of the cavity	$h_c$	0.60
Thickness of the coupling slot	$h_{cs}$	0.20
Width, length of the radiating cavity	$w_{rc}, l_{rc}$	1.65, 2.85
Width, length of the exciting slot	$w_{es}, l_{es}$	0.30, 2.44
Width, length of the cavity	$w_c, l_c$	4.69, 6.00
Width, length of the cavity wall	$w_t, l_t$	0.39, 0.74
Width, length of the coupling slot	$w_{cs}, l_{cs}$	0.25, 2.29

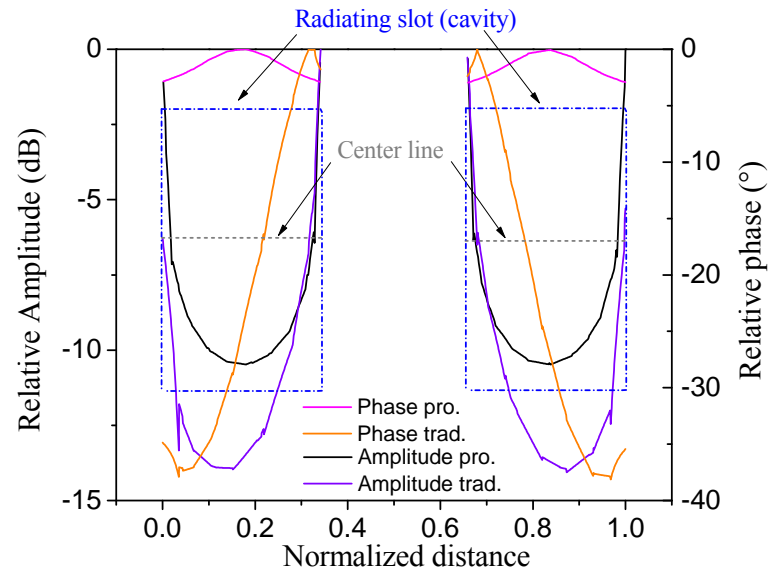


Fig. 3.4 Calculated amplitude and phase distribution of the  $E_x$  along the center line.

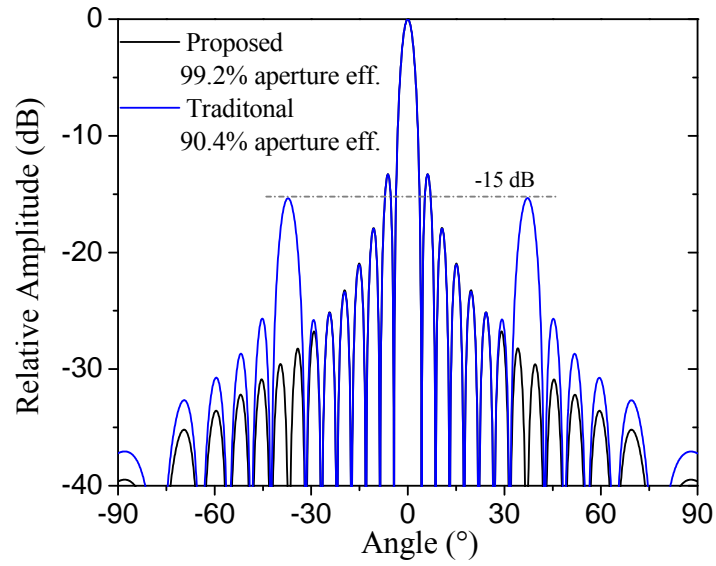


Fig. 3.5 Calculated  $E$ -plane radiation pattern with array-setup functionality.

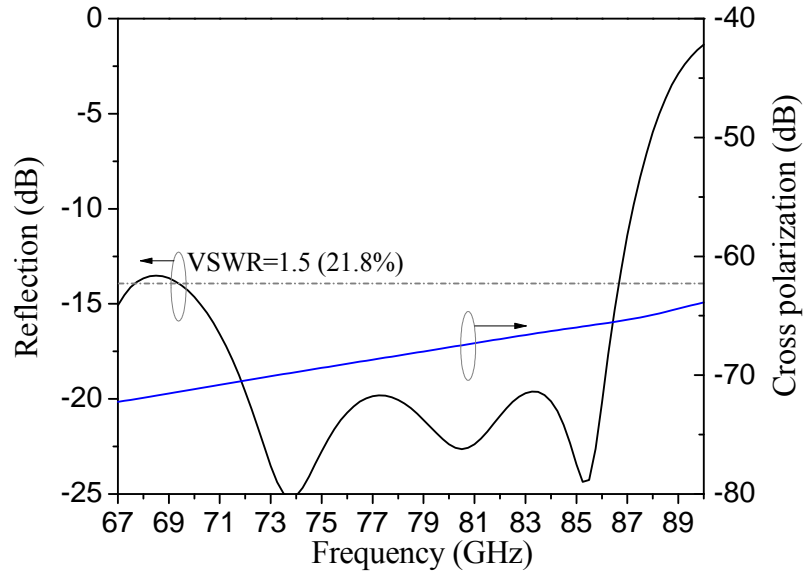


Fig. 3.6 Simulated reflection and cross polarization of the proposed  $2 \times 2$ -element subarray.

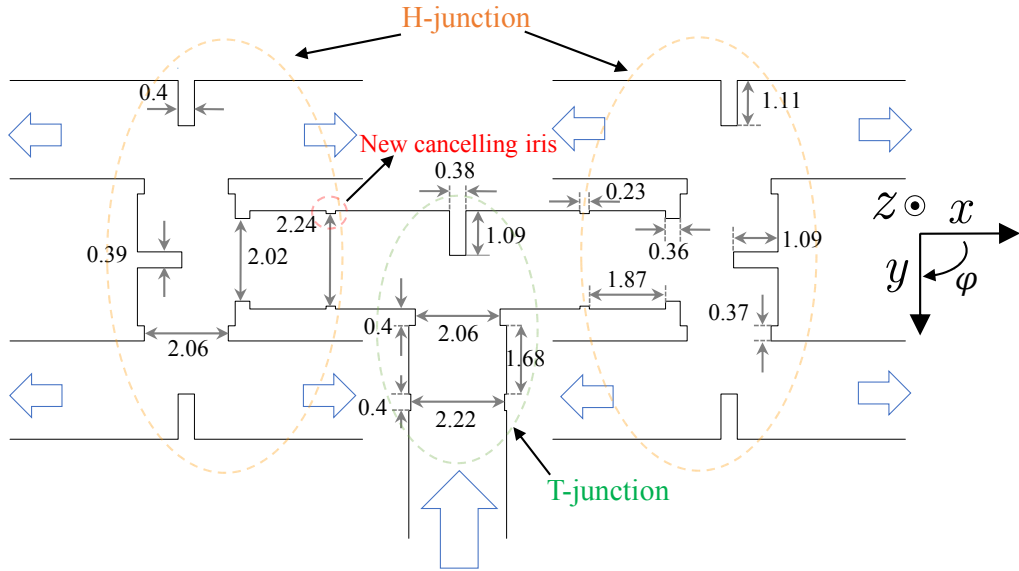


Fig. 3.7 Half bisection of a quarter of the corporate-feed circuit. Unit: millimeters.

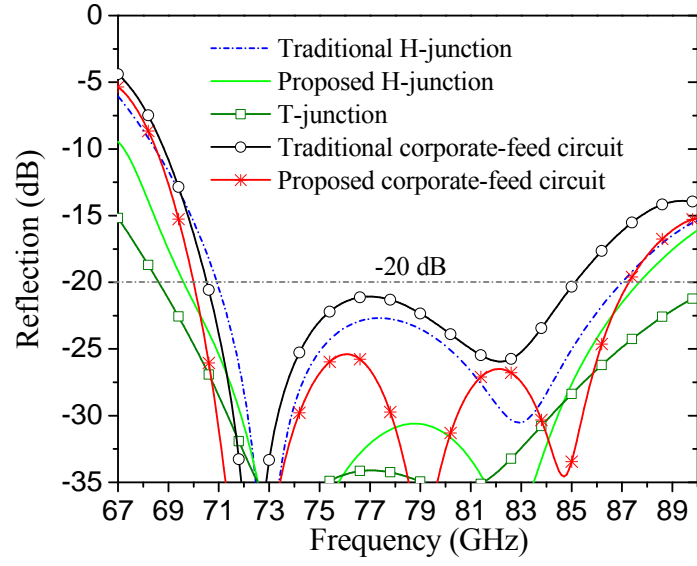
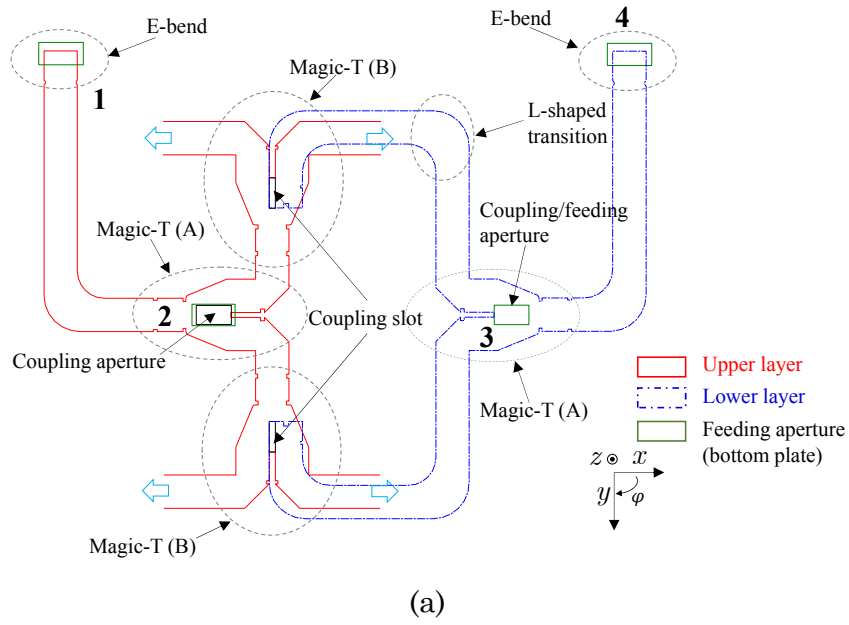


Fig. 3.8 Simulated reflection characteristics of the junctions and the corporate-feed circuit.



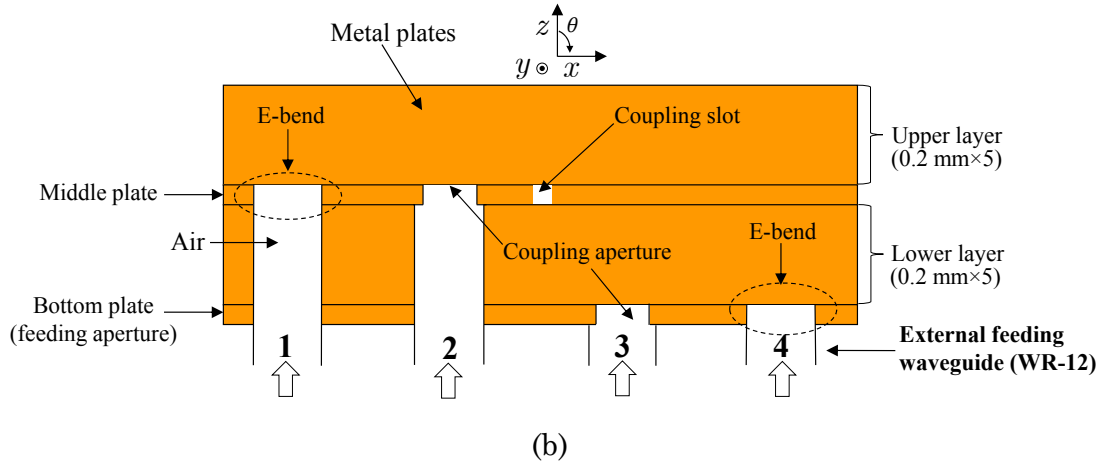


Fig. 3.9 Proposed comparator. (a) Geometry. (b) Stacking arrangement.

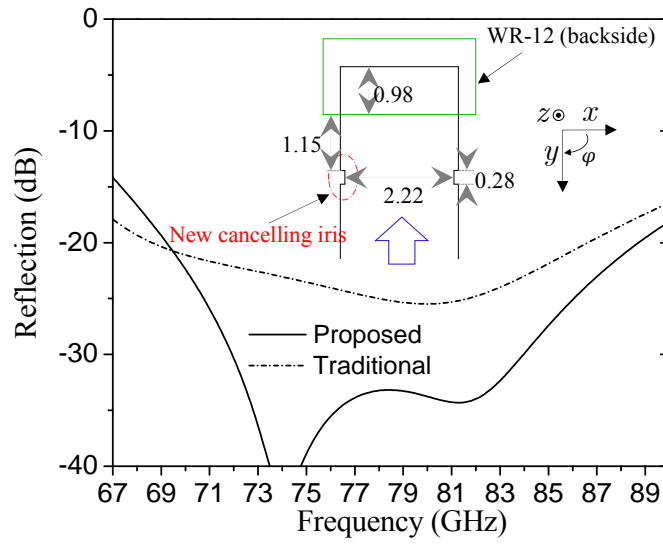


Fig. 3.10 Simulated reflection characteristic of the proposed E-bend, with inserted geometry. Unit: millimeters.

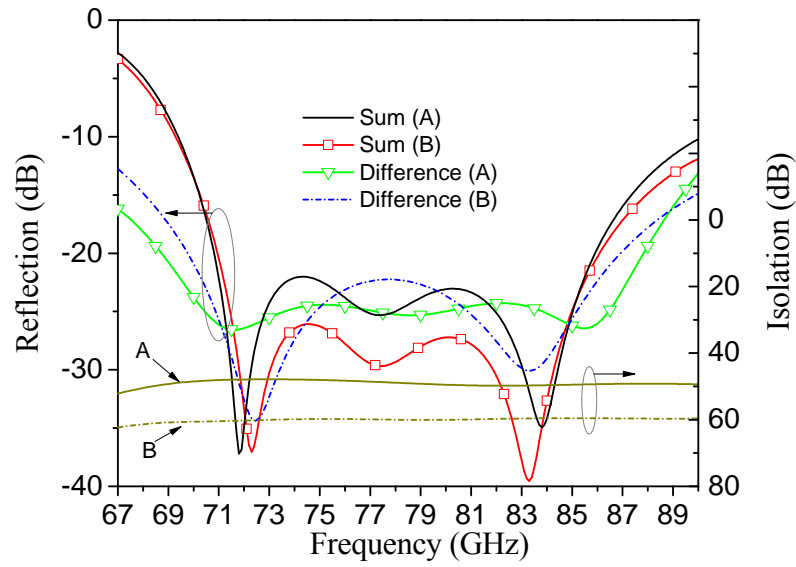
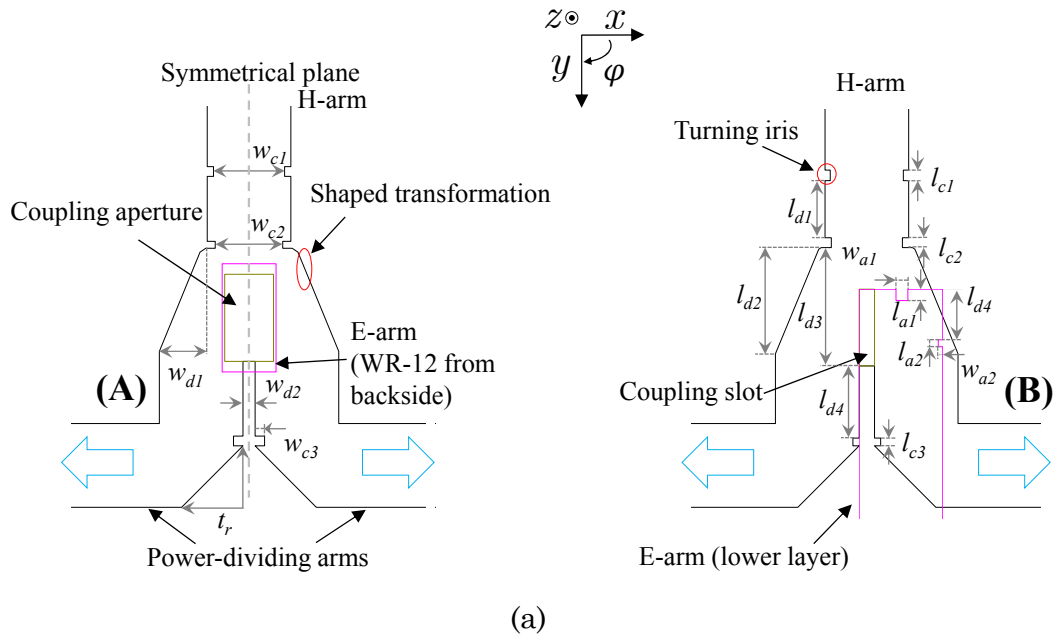


Fig. 3.11 Proposed magic-T. (a) Geometry. (b) Simulated reflection and isolation characteristics.



TABLE 3.2  
DESIGN PARAMETERS OF THE MAGIC-T

Design parameters	Value (mm)		Design parameters	Value (mm)	
	(A)	(B)		(A)	(B)
$l_{c1}$	0.30	0.28	$w_{c1}$	2.10	2.04
$l_{c2}$	0.29	0.20	$w_{c2}$	2.04	1.94
$l_{c3}$	0.23	0.28	$w_{c3}$	0.18	0.27
$l_{d1}$	1.64	1.86	$w_{d1}$	1.46	1.47
$l_{d2}$	3.04	2.95	$w_{d2}$	0.44	0.35
$l_{d3}$	3.39	3.24	$t_r$	\	1.76
$l_{d4}$	2.07	2.14	$w_{a1}$	\	0.34
$w_{a2}$	\	0.13	$l_{a1}$	\	0.32
$l_{a2}$	\	0.20	$l_{d4}$	\	1.45
Width/length of the coupling slot	\	0.44/2.20	Width/length of the coupling aperture	1.40/2.50	\

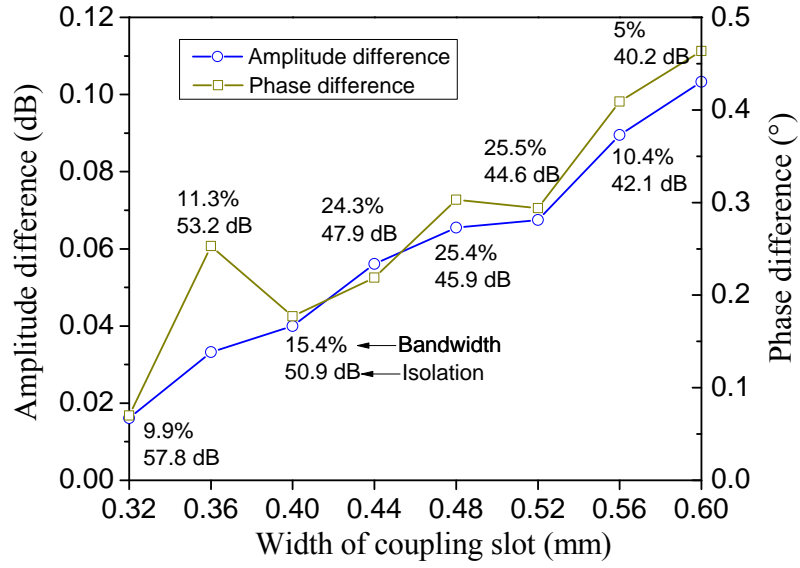
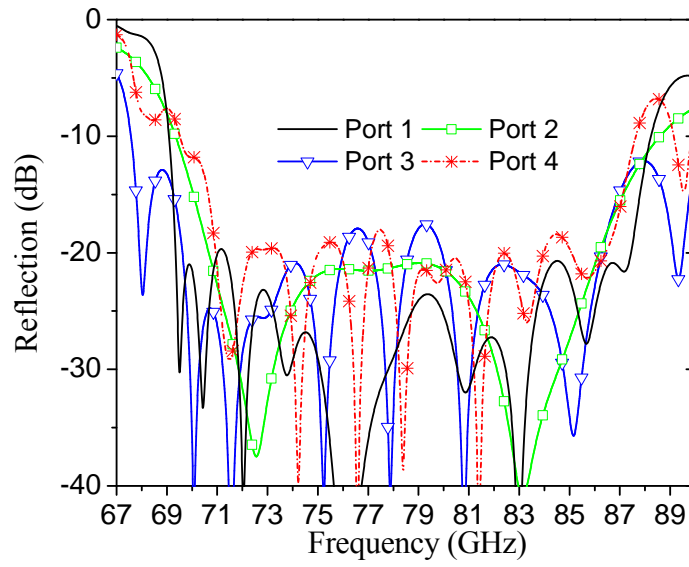
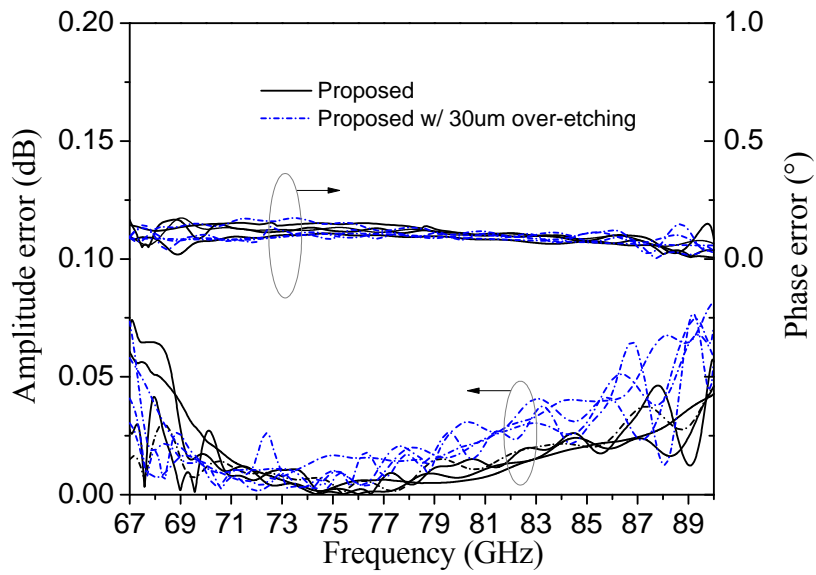


Fig. 3.12 Simulated bandwidth and isolation characteristics of magic-T (B).



(a)



(b)

Fig. 3.13 Simulated results of the proposed comparator. (a) Reflection characteristic. (b) Amplitude/phase error.

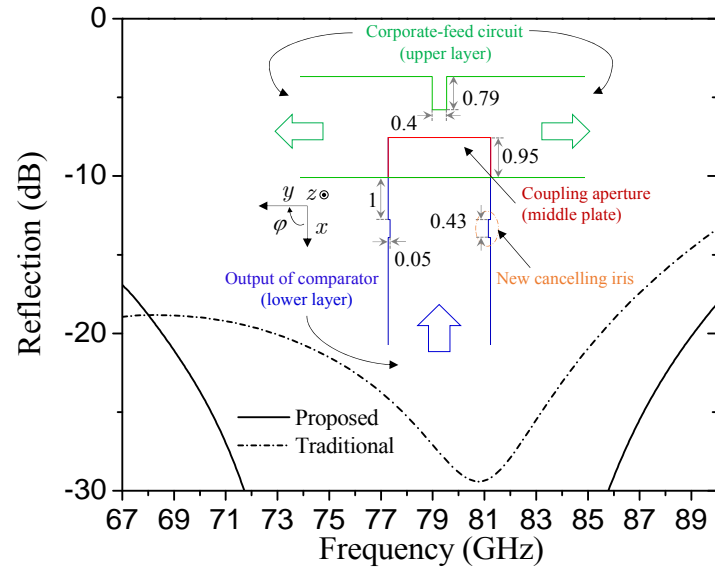


Fig. 3.14 Simulated reflection characteristic of the proposed double-layer interconnecting circuit, with inserted geometry. Unit: millimeters.

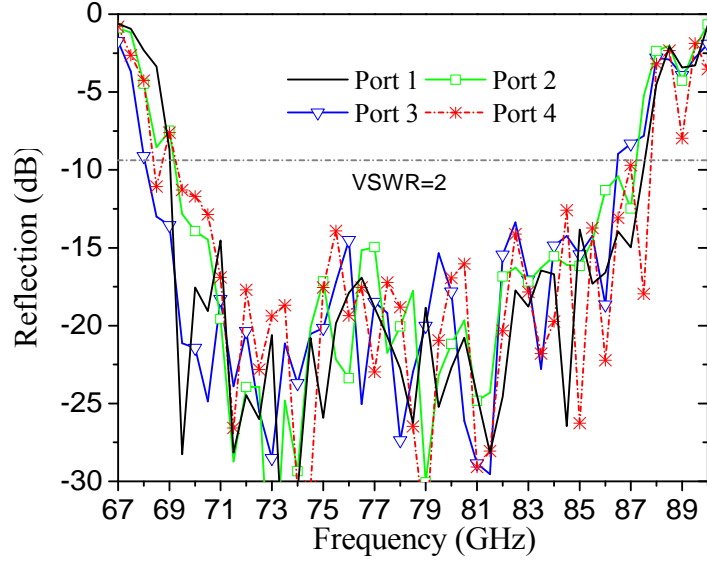


Fig. 3.15 Simulated reflection characteristic of the proposed antenna.

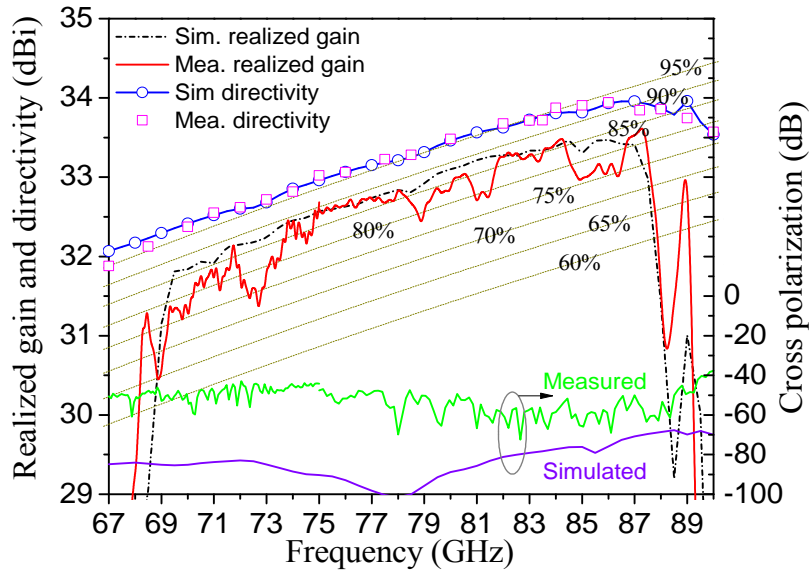


Fig. 3.16 Realized gain, directivity and cross polarization of the sum pattern at boresight.

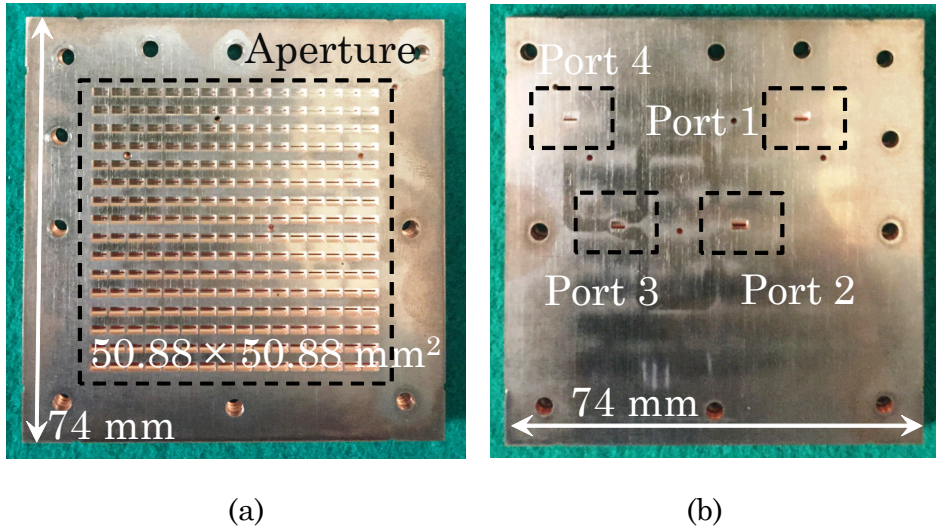
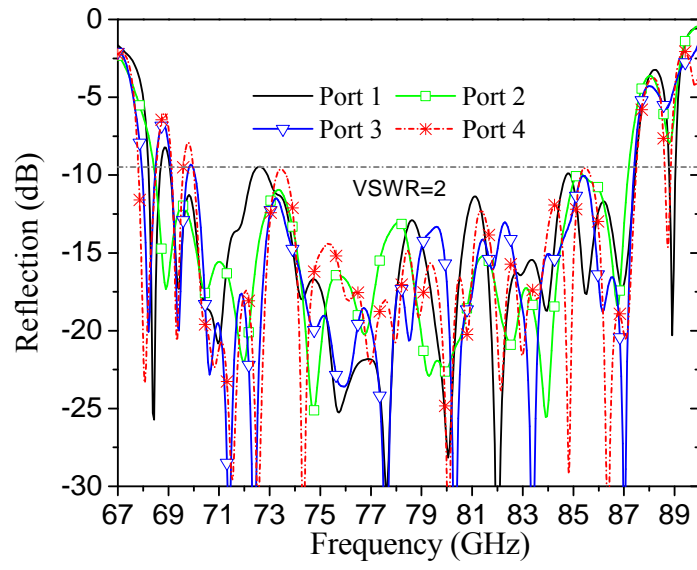
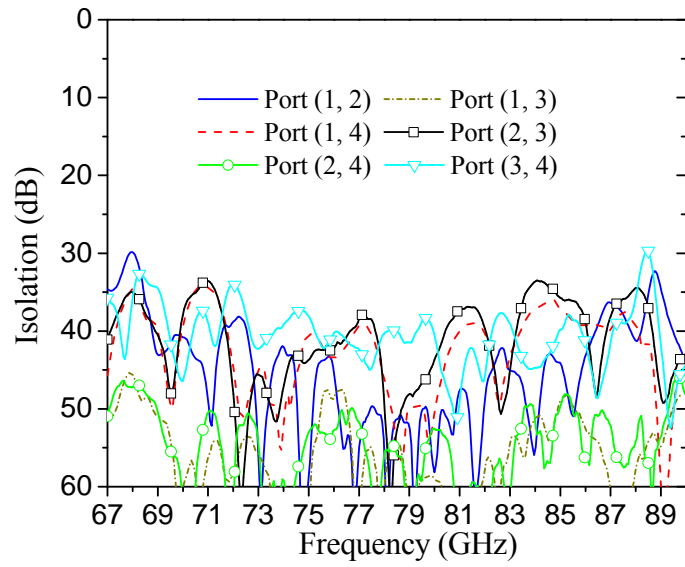


Fig. 3.17 Photograph of the fabricated prototype. (a) Front. (b) Back.



(a)



(b)

Fig. 3.18 Measured results of the antenna. (a) Reflection. (b) Isolation.

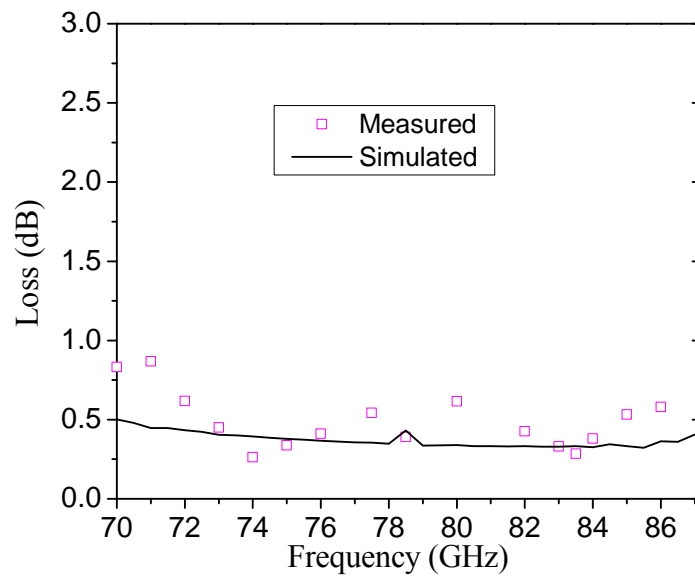


Fig. 3.19 Simulated and measured antenna losses.

TABLE 3.3  
AMPLITUDE DIFFERENCE OF THE PEAK GAIN BETWEEN THE SUM AND  
DIFFERENCE BEAMS

	E-plane	H-plane	45°-plane	135°-plane
Theoretical (dB)	3	3	6	6
Measured (dB)	2.85	3.18	6.10	6.03

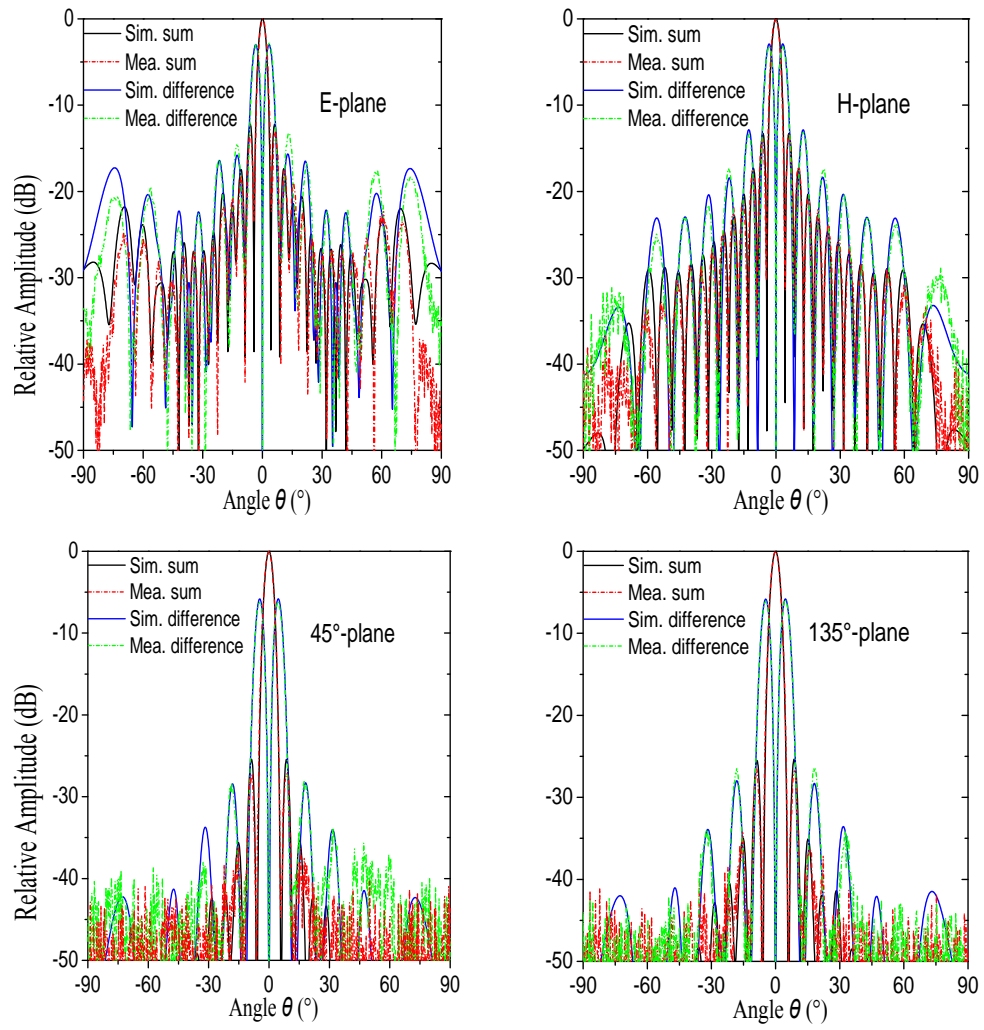


Fig. 3.20 Simulated and measured radiation patterns at the design frequency of 78.5 GHz in different planes.

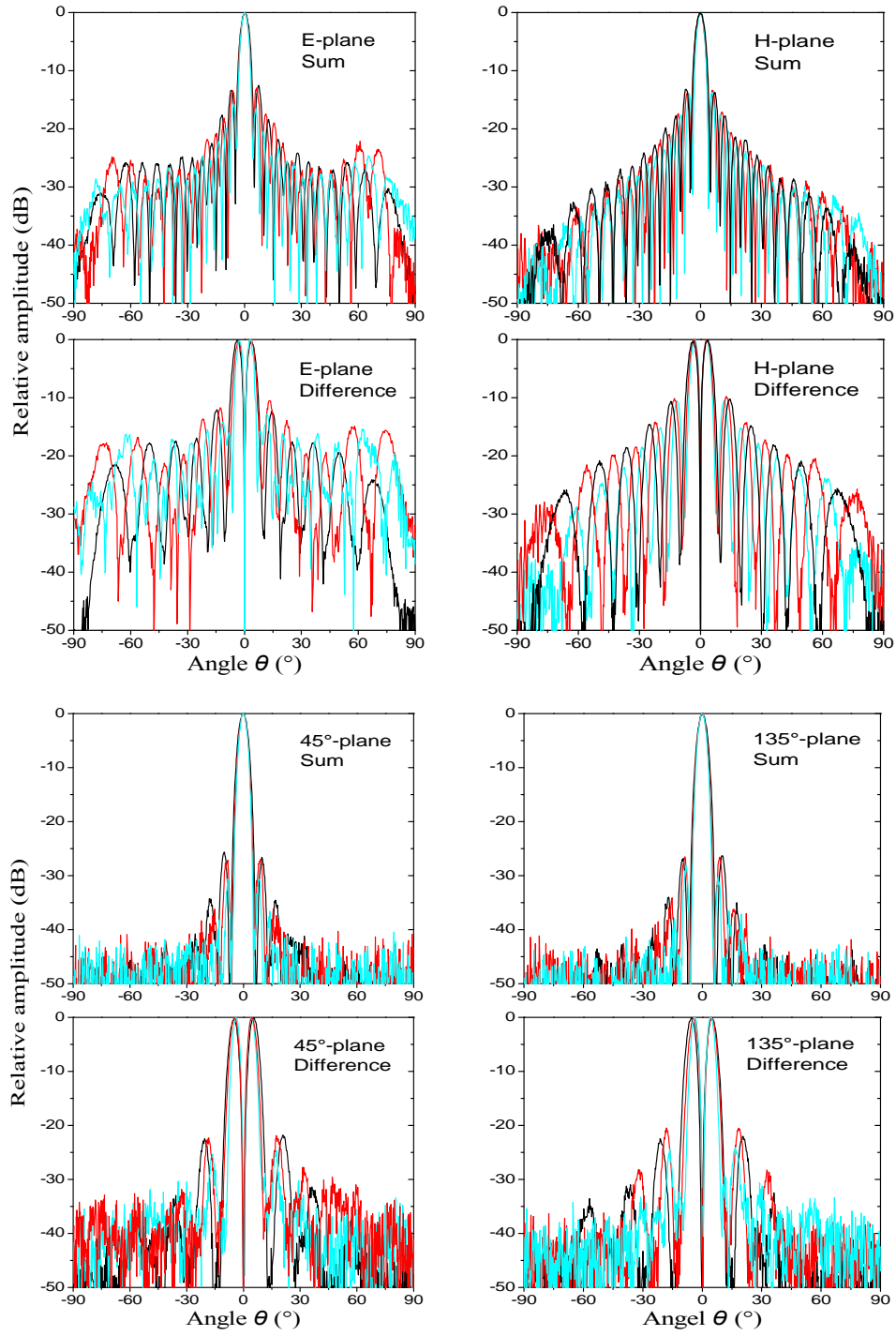
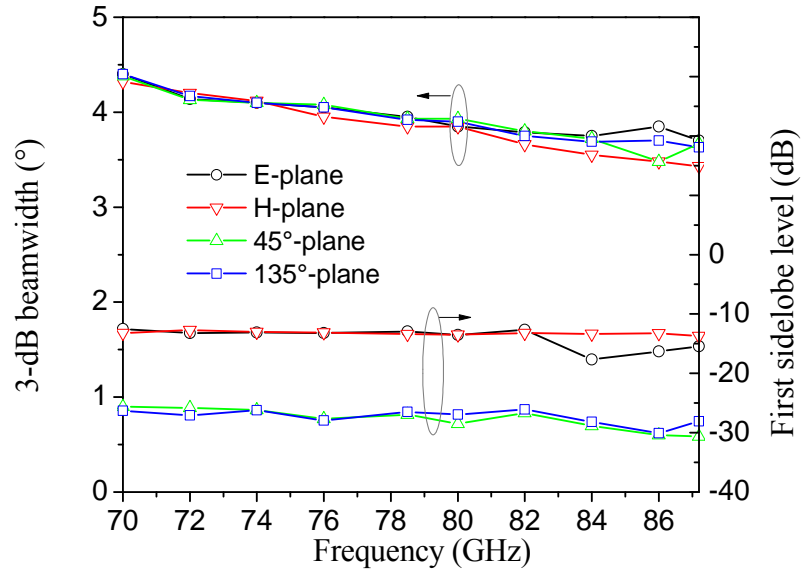
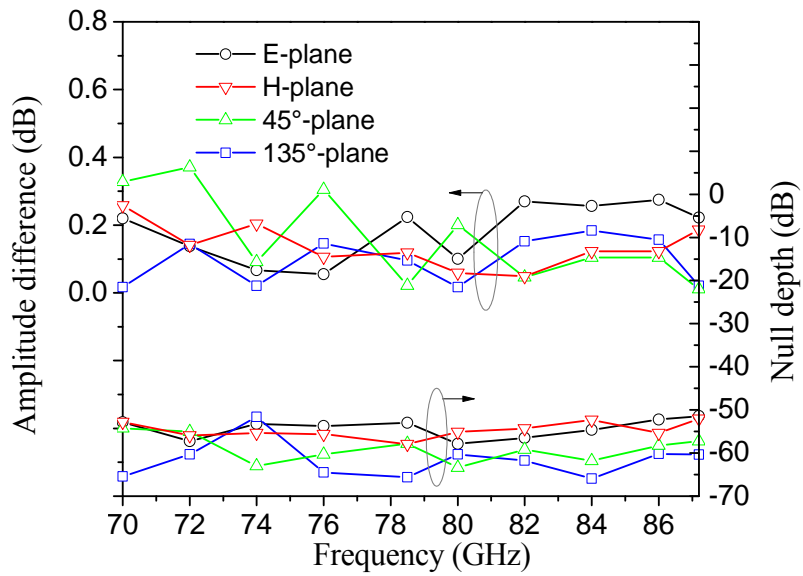


Fig. 3.21 Measured radiation patterns at 70 (black line), 78.5 (red line), and 87.2 (cyan line) GHz.





(a)



(b)

Fig. 3.22 Measured results. (a) 3-dB beamwidth and SLL of the sum beam.  
(b) Amplitude differences and null depth of the difference beam.

TABLE 3.4  
COMPARISON WITH OTHER RELATED WORK

Ref.	Architecture	Radiating element	$f_0$ (GHz)	Operation bandwidth (%)	Sum-beam realized gain at $f_0$ (dBi)	Sum-beam efficiency at $f_0$ (%)	Null depth at $f_0$ (dB)	Profile
[1.41]	Multi-layer	144-slot (RLSA)	13.7	$\approx 4.4$	18.2	$\approx 23.4$ (ant. eff.)	$< -25$ (circular polar.)	Planar
[1.42]	Single-layer	$16 \times 16$ -patch (microstrip)	14.25	5.6	24.5	20 (ant. eff.)	$< -30$ (E-plane) $< -30$ (H-plane)	Planar
[1.43]	Single-layer	$32 \times 32$ -slot (SIW)	94	3.2	25.21	16.3 (rad. eff.)	$-27.97$ (E-plane) $-27.60$ (H-plane)	Planar
[1.44]	Multi-layer	$26 \times 8$ -slot (SIW)	24.15	4.5	22.65	59.7 (rad. eff.)	$-20$ (H-plane)	Planar
[1.45]	Multi-layer	284-slot (waveguide)	17	2.9	$> 29$	—	$\approx -29$ (azimuth plane)	Three-dimensional
[1.46]	Multi-layer	820-slot (waveguide)	—	3.5	—	65.3 (not given)	$-35$ (E-plane) $-35$ (H-plane)	Three-dimensional
[1.47]	Multi-layer	$16 \times 16$ -slot (waveguide)	15	12.5	32.4	95 (not given)	$-38$ (E-plane) $-36$ (H-plane)	Three-dimensional
This work	Multi-layer	$16 \times 16$ -slot (waveguide)	78.5	21.9	32.6	83 (ant. eff.)	$-53$ (E-plane) $-58$ (H-plane)	Quasi-planar

# Chapter 4 Simultaneous Generation of Multiple OAM-Modes

## 4.1 Introductory Remarks

In this chapter, a RLSA, which is a light, low-cost and flat panel array antenna solution, has been proposed for future 60-GHz non-far region communication links using OAM multiplexing. Specifically, it is fed by an OAM beam-switching circuit using post-wall waveguide that allows simultaneously launching three different OAM-mode states. A Gaussian amplitude taper has been applied on the antenna aperture in order to launch a Gaussian beam. In addition, the effect of the aperture phase-taper on the channel capacity in OAM multiplexing has also been investigated.

## 4.2 Antenna Structure and Operation Mechanism

Fig. 4.1 shows the structure of the proposed antenna, which is designed at 60.4 GHz. It is basically composed of two parts, i.e. an OAM beam-switching circuit in the lower layer using post-wall waveguide (in 2.7mm-width) and a RLSA in the upper layer. Both the layers are made by a dielectric with  $\epsilon_r = 2.15$  and  $\tan \delta = 7 \times 10^{-4}$  (NPC-H220A by Nippon pillar packing company) and are 1.2-mm thick. The RLSA antenna is fed by the OAM beam-switching circuit through four coupling posts as shown in the inset of Fig. 4.1.

Fig. 4.2 shows the block diagram of the proposed antenna. The OAM beam-switching circuit has four input Port 1–4, and four output Port 5–8 (open posts) for feeding the RLSA. The OAM beam-switching circuit is sized by 68.0 mm  $\times$  26.0 mm  $\times$  1.2 mm, consisting of 90° hybrid couplers, cross couplers, and phase shifters.

Table 4.1 shows the phase shift at each output port. It can be found

that the OAM-mode states 0,  $-1$  and  $+1$  can be generated with reference to Ports 1, 3 and 4, respectively. Note that the phase shift associated to Port 2 does not allow to excite any rotational mode and thus Port 2 has to be closed on a matching load.

The antenna radiates a right-handed circular-polarized wave. The RLSA has 5079 radiating slot pairs, and the aperture size is approximately 200 mm ( $40\lambda$ , where  $\lambda$  is the wavelength in space at 60.4 GHz) in diameter.

To focalize in the non-far region, the Laguerre-Gaussian (LG) modes, that are solutions of paraxial Helmholtz equation in free space using cylindrical coordinates, have been considered. The LG modes are demonstrated to be capable of inherently processing OAM modes [4.1]. Based on the LG modes theory, a Gaussian amplitude taper has been applied on the antenna aperture. In addition, on the antenna aperture, we also have applied a phase taper, which can work as a convex lens. The applied phase taper can affect the transmission distance in the non-far region OAM multiplexing.

## 4.3 Antenna Design

### 4.3.1 OAM Beam-Switching Circuit

Theoretically, for an  $N \times N$  OAM beam-switching circuit, it can generate  $N$  OAM-mode states. However, in practical application where it is connected with an antenna, the number of launched OAM-mode states will be determined by the antenna configuration as well as the feeding structure.

Fig. 4.3 shows the structure of the OAM beam-switching circuit, which includes three kinds of building blocks. Building block 1 includes two identical  $90^\circ$  hybrids; building block 2 includes one  $90^\circ$  phase shifter, one cross coupler and one  $0^\circ$  phase shifter; building block 3 includes one  $-90^\circ$  phase shifter and three identical  $0^\circ$  phase shifters.

Fig. 4.4 shows the simulated reflection and isolation characteristics of

the OAM beam-switching circuit. Across the 58–63 GHz, the reflection and isolation are better than  $-17$  and  $18$  dB, respectively.

Fig. 4.5 shows the simulated amplitude and phase errors of the OAM beam-switching circuit. The amplitude error for one of the input ports is defined as the difference between the maximum and the minimum amplitudes among all the output ports. The phase error for one of the input ports is defined as the difference between the ideal and the average of the phase difference between adjacent output ports. At 60.4 GHz the amplitude error of Port 1, 3, and 4 are 1.4, 0.9, and 1.0 dB, and the phase error are  $1.6^\circ$ ,  $2.8^\circ$  and  $2.4^\circ$ , respectively.

### 4.3.2 Feeding Circuit for RLSA

The design objective of the feeding circuit for RLSA is to excite the specified modes in the PPW with low reflection good mode uniformity (in amplitude and phase).

Fig. 4.6 shows the analysis model of three types of feeding circuit using bended slots, center ring slot and open posts, respectively. The analysis model is a self-symmetric four-port network. The four input ports, Port 1–4 in the analysis model will be excited with the same amplitude and different progressive phase to simulate different OAM-mode states concerned in this work. To characterize this four-port network, the following reflection coefficients are defined:

$$R_1 = S_{11} + 2S_{12} + S_{13} \quad (\text{mode } 0) \quad (4-1)$$

$$R_2 = S_{11} - S_{13} \quad (\text{mode } \pm 1) \quad (4-2)$$

This design should be a compromise between the reflection and mode uniformity. At first the  $S_{11}$  should be minimized, then the  $R_1$  and  $R_2$  should be suppressed as low as possible. The center post in the upper substrate layer can enhance the isolation among the posts.

In Fig. 4.6(a), the four bended slots should be as close as possible in order to maintain a circumferential continuity. In Fig. 4.6(b), the circumferential length of the center ring slot should be around a quarter of wavelength at the design frequency in order to resonate. In Fig. 4.6(c), four 0.5mm-diameter posts occupy two substrate layers. These posts are arranged on a circle, whose radius is about  $\lambda_g/4$  ( $\lambda_g$  is the guide wavelength at 60.4 GHz in the PPW), concentric to the RLSA center.

Fig. 4.7 and Fig. 4.8 show the simulated reflection coefficients and the amplitude distribution inside the PPW under different mode operations. The bended slots can give good reflection coefficients. However, due to the circumferential discontinuity between the slots, the operation modes inside the PPW cannot be well excited. Due to the self-symmetrical characteristics, the center ring slot can excite the operation modes with very good field distributions. However, due to the strong coupling between the ports, the isolation is quite low. The open posts can be regarded as coaxial probes and work well here in terms of reflection coefficients and field uniformity.

These three types of feeding structure are summarized in Table 4.2. In this study, to guarantee a good rotational symmetry for OAM modes, the feeding circuit using four open posts is considered, at the cost of fabrication complexity. At the design frequency of 60.4 GHz, its  $S_{11}$ ,  $R_1$  and  $R_2$  are better than  $-15$  dB.

Fig. 4.9 shows the phase distribution of operation modes inside the PPW at 60.4 GHz. Similar to the amplitude distribution, good field uniformity is also observed. Fig. 4.10 shows the cross section of the open posts. The height of the posts are 1.8 mm, occupying 0.8 and 1 mm in two layers, respectively. Fig. 4.11 shows the simulated circumferential field distribution of mode 0 at 60.4 GHz. The amplitude and phase ripples are less than 0.5 dB and  $10^\circ$  respectively, implying good field uniformity is achieved.

### 4.3.3 RLSA

#### 4.3.3.1 Theoretical Analysis of the Aperture

In cylindrical coordinates, the solutions of the Helmholtz equation can be expressed as combinations of Laguerre–Gaussian modes [4.1], as

$$LG_p^l(\rho, \phi, z) = \sqrt{\frac{2p!}{\pi(p+|l|)}} \frac{1}{w(z)} \left(\frac{\sqrt{2}\rho}{w(z)}\right)^{|l|} L_p^{(|l|)}\left(\frac{2\rho^2}{w(z)^2}\right) \times \exp\left(-\frac{\rho^2}{w(z)^2} - jk \frac{\rho^2}{2R(z)} - jl\phi + j(2p+|l|+1)\zeta(z) - jkz\right) \quad (4-3)$$

$k = 2\pi / \lambda$  wave number

$z_R = \pi w_0^2 / \lambda$  Rayleigh length

$w(z) = w_0 \sqrt{1 + (z / z_R)^2}$  beam spot

$R(z) = z \left[ 1 + (z_R / z)^2 \right]$  curvature radius

$\zeta(z) = \arctan(z / z_R)$  Gouy phase

where  $\lambda$  is the wavelength,  $w_0$  is the waist radius,  $l$  and  $p$  are associated with the Laguerre polynomials. At any point along the beam-propagating direction these modes include the same Gaussian factor as the fundamental Gaussian mode multiplying the additional geometrical factors for the specified mode.

The beam waist  $w_0$  is selected as  $R/2$  (where  $R$  is the antenna radius). To launch the Gaussian beam, considering the fundamental LG mode under OAM-mode state 0, the amplitude distribution on the aperture is given by

$$\exp\left(-\frac{\rho^2}{w(z)^2}\right) \quad (4-4)$$

Based on (4-3), the phase distribution on the aperture is given as

$$\exp\left(jk \frac{\rho^2}{hR(z)}\right) \quad (4-5)$$

which can be treated as effect of convex lens or concave lens, when  $h$  is positive or negative, respectively.

Fig. 4.12 plots the amplitude and phase distributions of the aperture based on (4-4) and (4-5) with different  $h$  value.

Fig. 4.13 shows the analysis model of the transmittance between the

transmitter (Tx) and the receiver (Rx) antennas in a cylindrical coordinate. The analysis model is assumed to be loss less, bi-directional, and symmetrical. The Tx and the Rx antennas have the same complex aperture distributions of  $A(\rho)$ , which is  $\phi$ -independent.

Under OAM-mode state  $l$ , the transmittance  $S_{ll}$  is given by

$$(S_{ll})^2 = \frac{1}{\sqrt{P(\text{Tx})}\sqrt{P(\text{Rx})}} \int_0^{2\pi} \int_0^R M A(\rho) \rho d\rho d\phi \quad (4-6)$$

$P(\text{Tx}) = P(\text{Rx}) = \int_{\phi=0}^{2\pi} \int_{\rho=0}^R A(\rho)^* A(\rho) \rho d\rho d\phi$  are defined as the power stored on each antenna aperture,  $M$  is the propagated field generated by Tx antenna on the Rx antenna surface.

By applying the  $l$ -th order Hankel transform, the spectrum  $F_l$  of the Tx and Rx antenna apertures are given by

$$F_l^{\text{Tx}}(k_\rho) = F_l^{\text{Rx}}(k_\rho) = \int_0^R A(\rho) J_l(k_\rho \rho) \rho d\rho \quad (4-7)$$

where  $J_l$  is the Bessel function of the first kind of order  $l$ ,  $k_\rho$  is the wave number in the radial direction. Therefore the  $M$  can be interpreted as

$$M = \int_0^k F_l^{\text{Tx}}(k_\rho) J_l(k_\rho \rho) e^{-jk_z z_0} k_\rho dk_\rho \quad (4-8)$$

By applying (4-7) and (4-8), (4-6) will be as

$$\begin{aligned} & \frac{1}{\int_{\phi=0}^{2\pi} \int_{\rho=0}^R A(\rho)^* A(\rho) \rho d\rho d\phi} \int_0^{2\pi} \int_0^R \left( \int_0^k (F_l^{\text{Tx}}(k_\rho) J_l(k_\rho \rho) e^{-jk_z z_0} k_\rho dk_\rho) \right) A(\rho) \rho d\rho d\phi \\ &= \frac{2\pi}{\int_{\phi=0}^{2\pi} \int_{\rho=0}^R A(\rho)^* A(\rho) \rho d\rho d\phi} \int_0^k F_l^{\text{Tx}}(k_\rho) \left( \int_0^R A(\rho) J_l(k_\rho \rho) \rho d\rho \right) e^{-jk_z z_0} k_\rho dk_\rho \\ &= \frac{2\pi}{\int_{\phi=0}^{2\pi} \int_{\rho=0}^R A(\rho)^* A(\rho) \rho d\rho d\phi} \int_0^k F_l^{\text{Tx}}(k_\rho) F_l^{\text{Rx}}(k_\rho) e^{-jk_z z_0} k_\rho dk_\rho \end{aligned} \quad (4-9)$$

where  $k_z = \sqrt{k^2 - k_\rho^2}$  is the wave number in the  $z$  direction.

Fig. 4.14 shows the calculated transmittance with different  $h$  value, and the result with uniform phase distribution is also added. It can be found that among these three types of phase distributions, the one using concave lens has the poorest performance in terms of the S-parameter and



transmission distance. Compared to the case using uniform phase, the one using convex lens has slightly improved transmission distance however degraded S-parameter. Here the phase taper using convex lens is considered for the purpose of enhancing the transmission distance.

The OAM communication can be treated as a sub-topic of traditional multiple-in-multiple-out (MIMO) communication. Here we use the channel capacity of the MIMO system to evaluate the OAM system. The capacity of the system which includes the OAM-mode orthogonality is given by [4.2]

$$\sum_{l=1}^3 \log_2(1 + \text{SNR} |S_{ll}|^2) \quad (4-10)$$

where SNR is the signal-to-noise ratio determined by the transmit power, carrier bandwidth, noise density, noise figure and so on.

Fig. 4.15 shows the calculated channel capacity based on the aperture distribution using Gaussian amplitude taper and convex-lens phase taper. The calculated channel capacity has been normalized by the maximum value among the curves to eliminate the effect from different system specifications. It can be found that  $h$  can affect the near-region channel capacity and the  $h$  of 11 can give the best performance in terms of flatness. The aperture distribution with  $h = 11$  will be used in the design of the aperture in the following sub-section.

### 4.3.3.2 Design of the Aperture

This methodology can be interpreted as a holographic technique, followed by an optimization procedure that makes use of specific fitness functions introduced on the basis of the physical picture behind the working mechanism of the RLSA antenna [4.3].

The aperture distribution is assumed to be rotationally symmetric, the ideal target aperture magnetic current (the holographic image) can be expressed as

$$\mathbf{M}_0(\rho_i) = A(\rho_i) \hat{\mathbf{p}} \quad (4-11)$$

where  $A(\rho_i)$  is the aperture distribution in the design process,  $\hat{\mathbf{p}} = (\hat{\mathbf{x}} - j\hat{\mathbf{y}}) / \sqrt{2}$  is the right-hand circular polarization unit vector,  $\rho_i = (\rho_i, \phi_i)$  is the position of center of the  $i$ th slot pair element. The holographic interference pattern is given by the position and length of each slot pair element, which satisfy the following equations:

$$|\underline{\alpha}_m^p(\rho_i) \cdot \mathbf{H}^{\text{inc}}(\rho_i)| = C |A(\rho_i)| \quad (4-12)$$

$$\angle \{ \mathbf{M}_0^*(\rho_i) \cdot \underline{\alpha}_m^p(\rho_i) \cdot \mathbf{H}^{\text{inc}}(\rho_i) \} = \gamma \quad (4-13)$$

Where  $\underline{\alpha}_m^p$  is the dyadic polarizability of each slot pair that constitutes the circular polarization radiating element of the RLSEA;  $\mathbf{H}^{\text{inc}}$  is the incident wave excitation, which here is considered a cylindrical mode  $\text{TM}_{0,0}^z$  in the PPW;  $\gamma$  and  $C$  are arbitrary real constants. (4-12) imposes the matching between the magnitude distribution on the radiating aperture and the target one while (4-13) controls the correct slot pair positioning to ensure the target aperture phase distribution. A variation in slot length mainly affects the associated magnetic moment magnitude on the slot pair, while the phase change is a higher order effect; similarly, a variation in slot position mainly affects the associated magnetic moment phase on the slot pair, while the magnitude remains almost the same.

In the optimization scheme, this slots spiral is split into  $n_{\text{ring}}$  adjacent subspirals, the following complex fitness function is introduced to target the ideal aperture distribution, as

$$\overline{F}_n = 1 - \frac{\overline{A}}{\overline{M}} \left\{ \sum_{\substack{i=N_{n-1} \\ n>0}}^{N_n} \frac{\hat{\mathbf{p}}_{\text{RH}} \cdot \mathbf{M}(\rho_i)}{A(\rho_i)} \frac{i - N_{n-1}}{N_n - N_{n-1}} + \sum_{\substack{i=N_{n+1} \\ n < n_{\text{ring}}}} \frac{\hat{\mathbf{p}}_{\text{RH}} \cdot \mathbf{M}(\rho_i)}{A(\rho_i)} \frac{N_{n+1} - i}{N_{n+1} - N_n} \right\} \quad (4-14)$$

where  $\mathbf{M}(\rho_i)$  is the equivalent dipole moment of each slot pair, while  $\overline{A} = \sum_{i=1}^N |A(\rho_i)| / N$  and  $\overline{M} = \sum_{i=1}^N |\hat{\mathbf{p}}_{\text{RH}} \cdot \mathbf{M}(\rho_i)| / N$  are the target and the realized average co-polar dipole moment magnitudes, respectively, with  $N$  denoting

the total number of slot pairs.

In addition, another fitness function is introduced to target the ideal aperture distribution and to mitigate the effect of higher-order mode  $\text{TM}_{0,-2}^z$ , as

$$\begin{aligned} \bar{G}_n = 1 + & \sum_{\substack{i=N_{n-1} \\ n>0}}^{N_n} \frac{H_2^{(2)}\left(k_\rho \left[\rho_i - \frac{\Delta\rho}{2}\right]\right) e^{-2j\phi_{i1}} \hat{\phi}_{i1} \cdot \mathbf{M}_1(\rho_i)}{H_2^{(2)}\left(k_\rho \left[\rho_i + \frac{\Delta\rho}{2}\right]\right) e^{-2j\phi_{i2}} \hat{\phi}_{i2} \cdot \mathbf{M}_2(\rho_i)} \times \frac{i - N_{n-1}}{N_n - N_{n-1}} \\ & + \sum_{\substack{i=N_{n+1} \\ n < n_{\text{ring}}}}^{N_{n+1}} \frac{H_2^{(2)}\left(k_\rho \left[\rho_i - \frac{\Delta\rho}{2}\right]\right) e^{-2j\phi_{i1}} \hat{\phi}_{i1} \cdot \mathbf{M}_1(\rho_i)}{H_2^{(2)}\left(k_\rho \left[\rho_i + \frac{\Delta\rho}{2}\right]\right) e^{-2j\phi_{i2}} \hat{\phi}_{i2} \cdot \mathbf{M}_2(\rho_i)} \times \frac{N_{n+1} - i}{N_{n+1} - N_n} \end{aligned} \quad (4-15)$$

where  $k_\rho$  is the radial propagation constant of the mode  $\text{TM}_{0,0}^z$  in the PPW, and  $\phi_{i1}$  and  $\phi_{i2}$  are the azimuthal coordinates of the inner and outer slots, respectively, in the slot pair of center  $\rho_i$ , while  $\mathbf{M}_1(\rho_i)$  and  $\mathbf{M}_2(\rho_i)$  are the relevant dipole moments.

The optimization process converges in 28 steps. The resulting RLSA has 5077 radiating slot pairs, with slot length in between 1.16 mm and 1.70 mm, while the width is kept constant to 0.15 mm.

## 4.4 Simulated Results

### 4.4.1 Reflection and Isolation

The full antenna structure including the OAM beam-switching circuit and the RLSA has been simulated using HFSS 16. The copper with a conductivity of  $5.8 \times 10^7$  S/m was used throughout the simulations.

Fig. 4.16 shows the reflection and isolation characteristics of the antenna input ports. At the design frequency of 60.4 GHz, the reflections of the Port 1–3 are better than  $-16$  dB and the isolation among the input ports are better than 18 dB.

#### 4.4.2 Directivity and Cross-polarization of Port 1

Fig. 4.17 shows the simulated directivity and cross-polarization of Port 1 in the bore-sight. At the design frequency of 60.4 GHz, the directivity is 38.8 dBi, which correspond to aperture efficiency of 46%. Across 58–63 GHz, the cross-polarization is better than  $-28$  dB.

The antenna loss mainly comes from the mismatching, the conductor and the dielectric. At 60.4 GHz, the simulated mismatching, conductor and dielectric losses are 0.1, 0.9 and 1.2 dB, respectively.

#### 4.4.3 Field Distribution

Fig. 4.18 and 4.19 show the simulated E-field distribution (amplitude and phase) on the aperture and the reception plane (a distance of two times of Rayleigh length from the antenna surface) at the design frequency of 60.4 GHz. The applied amplitude and phase tapers can be verified by the field distributions of the Port 1. Note that the discrepancy between the designed and simulated aperture distribution can be attributed to the feeding effect from the OAM beam-switching circuit. The expected OAM phenomenon can be verified by the phase distributions of the Port 3 and 4.

### 4.5 Concluding Remarks

This chapter presents a 60-GHz RLSA, which is fed by an OAM beam-switching circuit, for OAM multiplexing. The OAM beam-switching circuit is based on a post-wall waveguide. It has four input ports and can generate three kinds of progressive phase difference among the output ports for OAM operation. We proposed three types of feeding circuit for the RLSA by using bended slots, center ring slot and open posts. It is found that the feeding circuit using open posts can give a good reflection coefficient as well as a good

field uniformity. To launch a Gaussian beam, a Gaussian amplitude taper has been applied on the antenna aperture. We also investigated the effect from the aperture phase distribution by using the uniform, convex lens and concave lens distributions. It is found that the convex-lens phase taper can give a better performance in terms of the transmission distance.

The design concept has been verified by simulating the full antenna model including the OAM beam-switching circuit and the RLSA, where the feeding circuit using open posts and the convex-lens aperture phase taper are considered. The simulated results show that, at the design frequency, the proposed antenna can generate three OAM-mode states:  $l = 0$ ,  $-1$ , and  $+1$  with good spatial distributions.

## References

- [4.1] L. Allen, , M.W. Beijersbergen, R.J.C. Spreeuw, and J.P. Woerdman, “Orbital angular momentum of light and the transformation of Laguerre-Gaussian modes,” *Phys. Rev. A*, vol. 45, no. 11, pp. 8185–8190, June 1992.
- [4.2] O. Edfors and A. J. Johansson, “Is orbital angular momentum (OAM) based radio communication an unexploited area?” *IEEE Trans. Antennas Propag.*, vol. 60, no. 22, pp. 1126–1131, Feb. 2012.
- [4.3] M. Albani, A. Mazzinghi, and A. Freni, “Automatic design of CP-RLSA antennas,” *IEEE Trans. Antennas Propag.*, vol. 60, no. 12, pp. 5538–5547, Dec. 2012.

## Figures and Tables

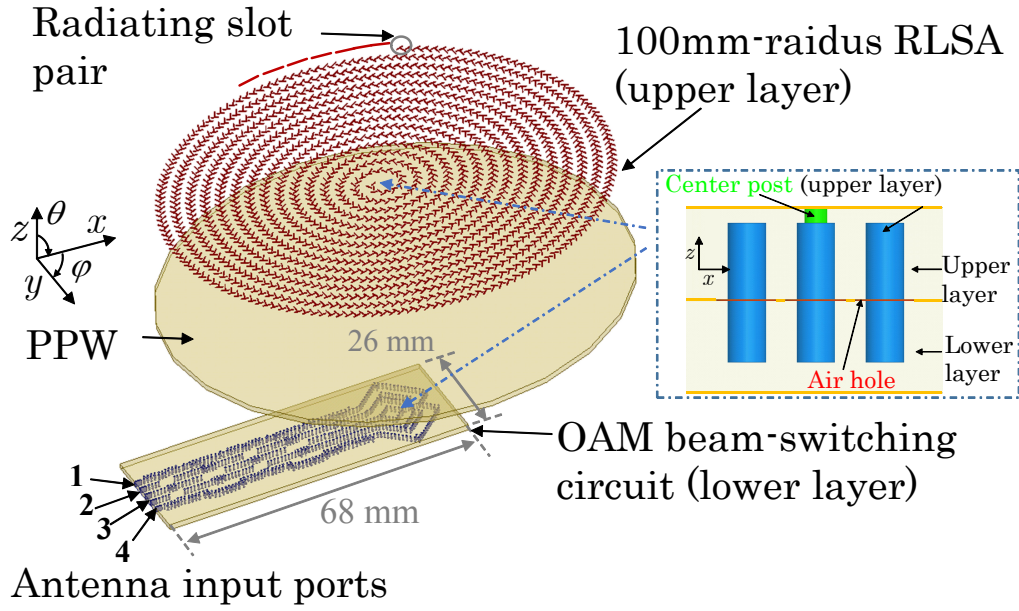


Fig. 4.1 Structure of the proposed antenna.

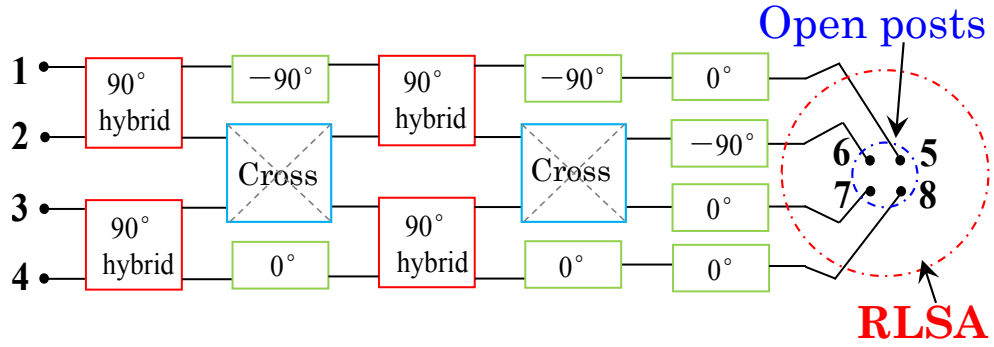


Fig. 4.2 Block diagram of the proposed antenna.

TABLE 4.1  
PHASE SHIFT AT EACH OUTPUT PORT

	5	6	7	8	OAM mode
1	$0^\circ$	$0^\circ$	$0^\circ$	$0^\circ$	0
2	$0^\circ$	$180^\circ$	$0^\circ$	$180^\circ$	NA
3	$0^\circ$	$-90^\circ$	$-180^\circ$	$-270^\circ$	-1
4	$0^\circ$	$90^\circ$	$180^\circ$	$270^\circ$	+1

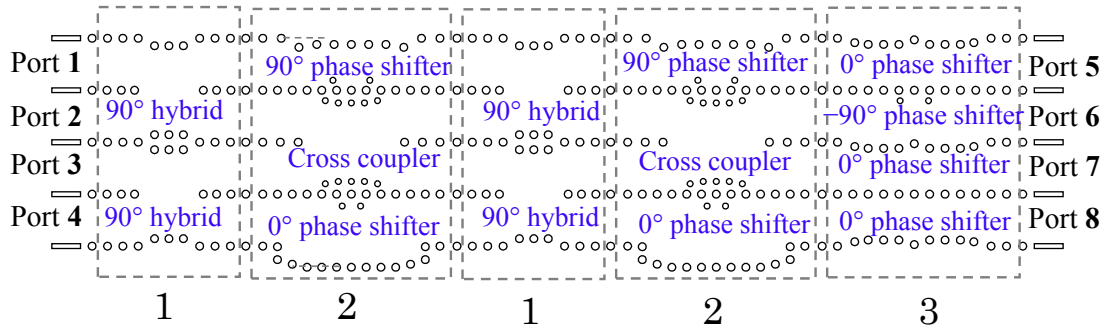
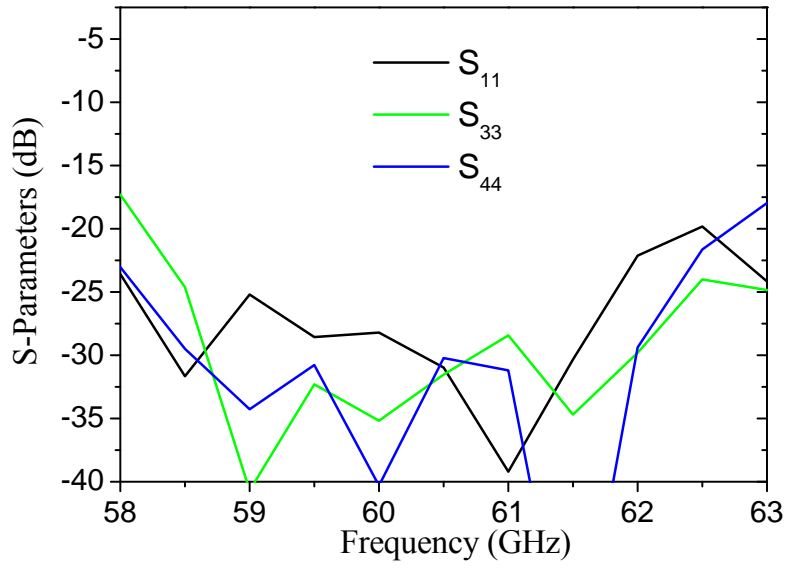
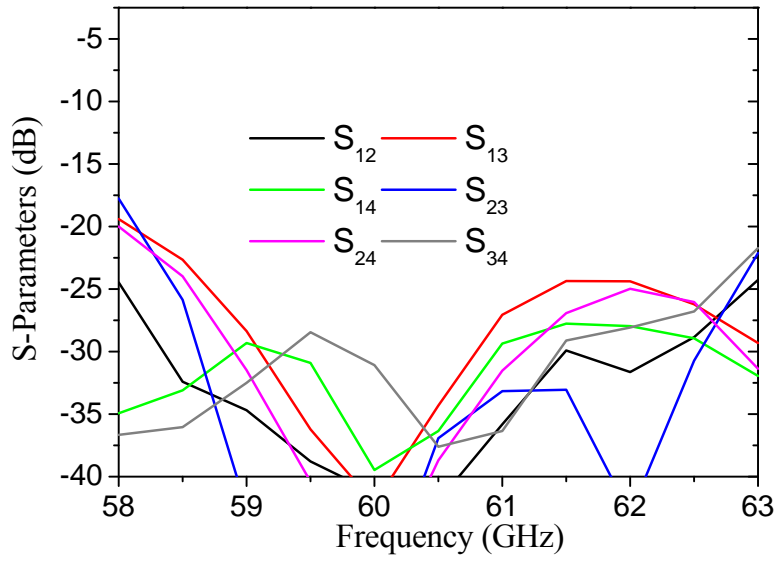


Fig. 4.3 Structure of the OAM beam-switching circuit.



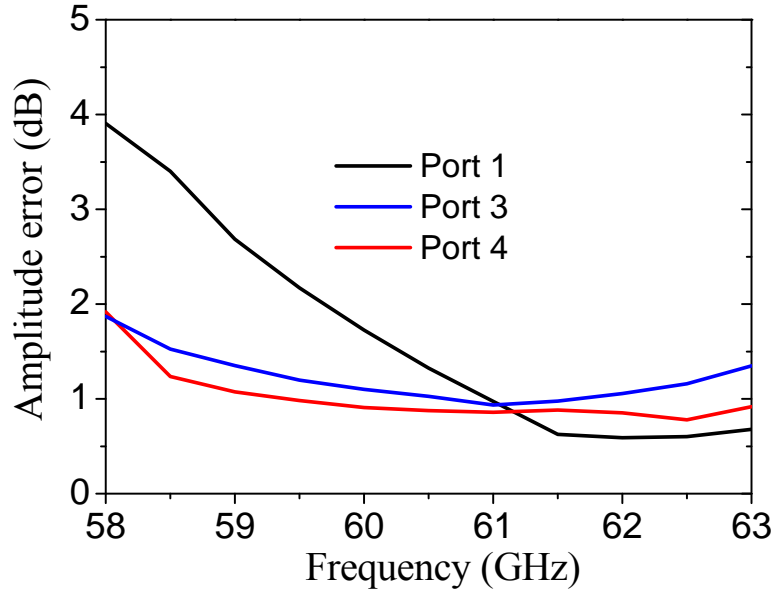


(a)

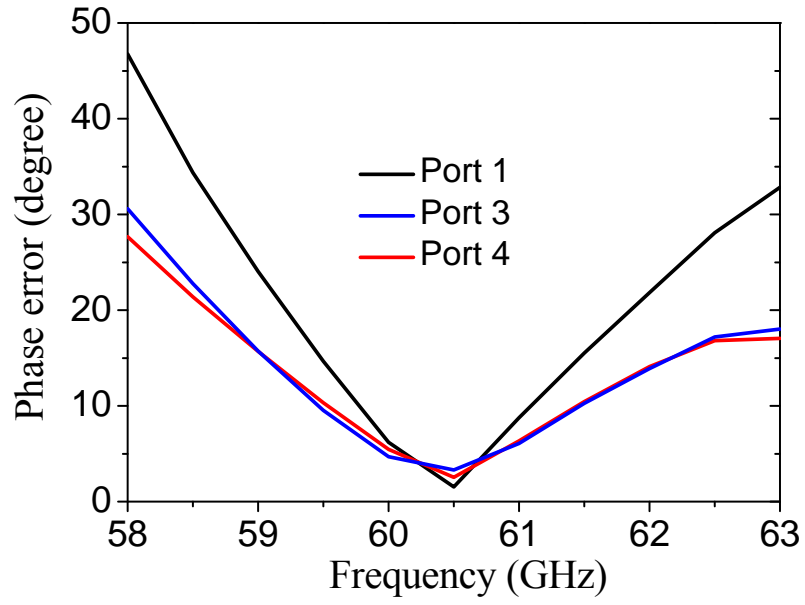


(b)

Fig. 4.4 Simulated results of the OAM beam-switching circuit. (a) Reflection.  
(b) Isolation.



(a)



(b)

Fig. 4.5 Simulated amplitude and phase errors of the OAM beam-switching circuit.

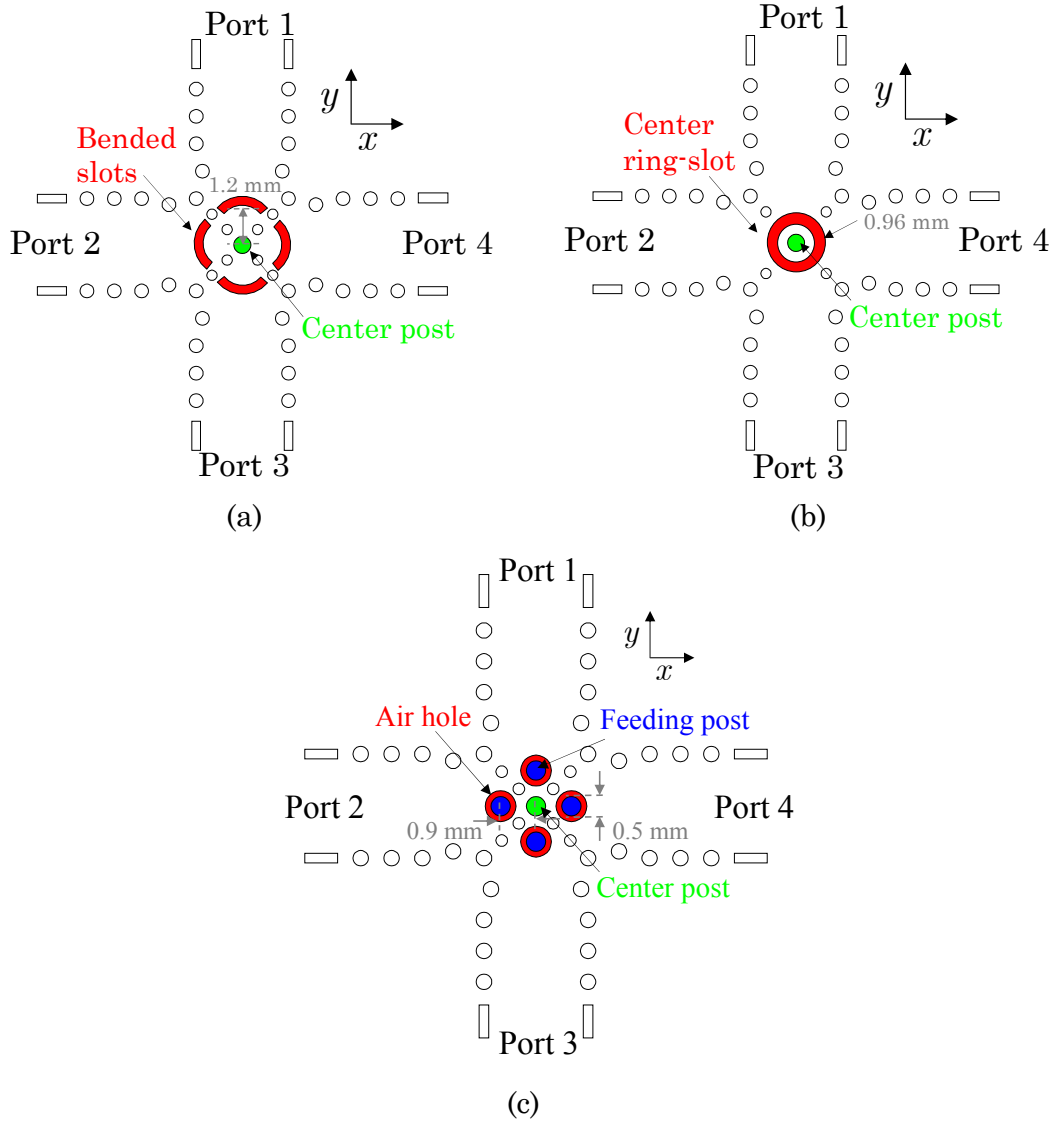


Fig. 4.6 Feeding circuit for RLSA. (a) Bended slots. (b) Center ring slot. (c) Open posts.

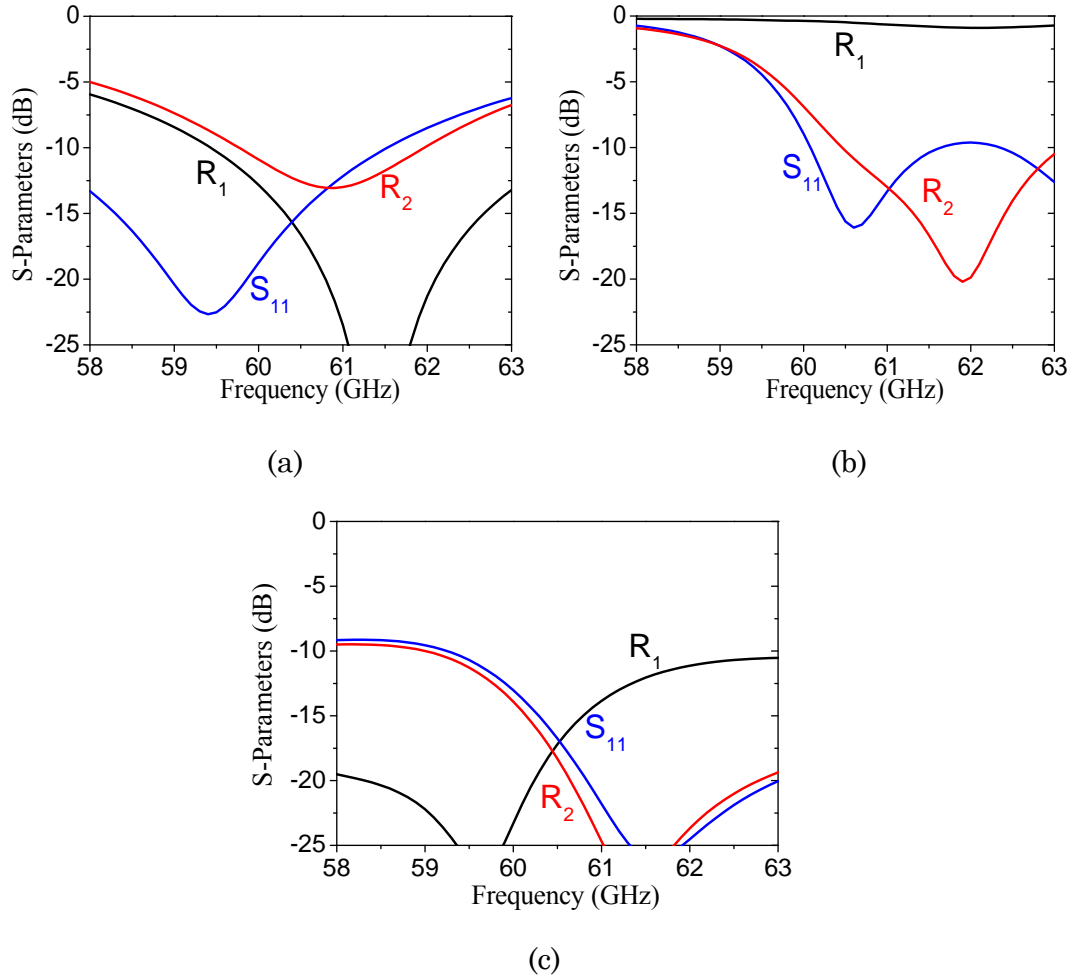


Fig. 4.7 Simulated reflection coefficients of the feeding circuit for RLSA. (a) Bended slots. (b) Center ring slot. (c) Open posts.

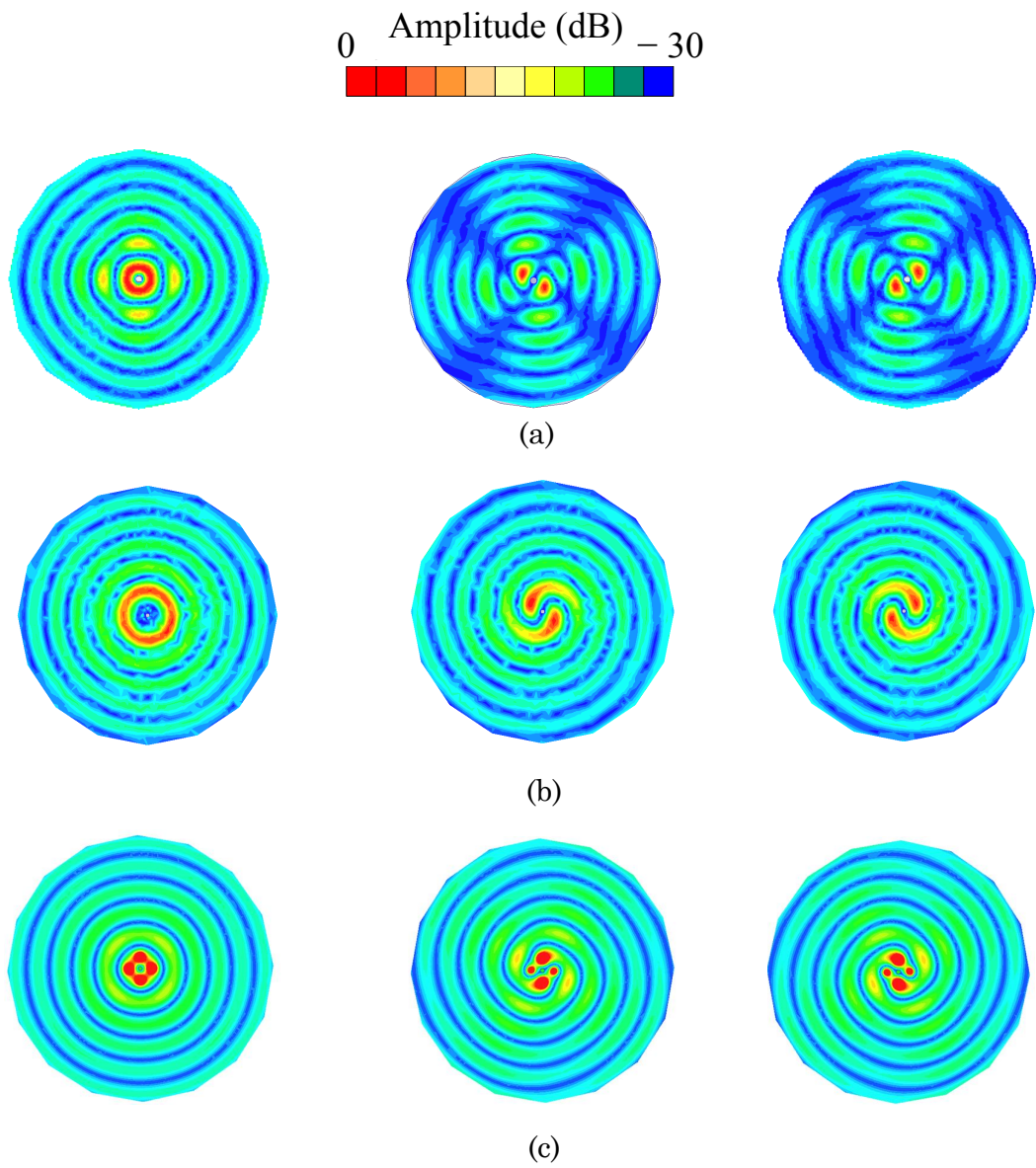


Fig. 4.8 Amplitude distribution of operation modes inside the PPW (from left to right are modes 0,  $-1$  and  $+1$ , respectively). (a) Bended slots. (b) Center ring slot. (c) Open posts.

TABLE 4.2

SUMMARY OF THREE TYPES OF FEEDING CIRCUIT

	Field uniformity	S-parameter	Fabrication complexity
<b>Bended slots</b>	☹️	😊	😊
<b>Centered ring slot</b>	😊	☹️	😊
<b>Open posts</b>	😊	😊	☹️

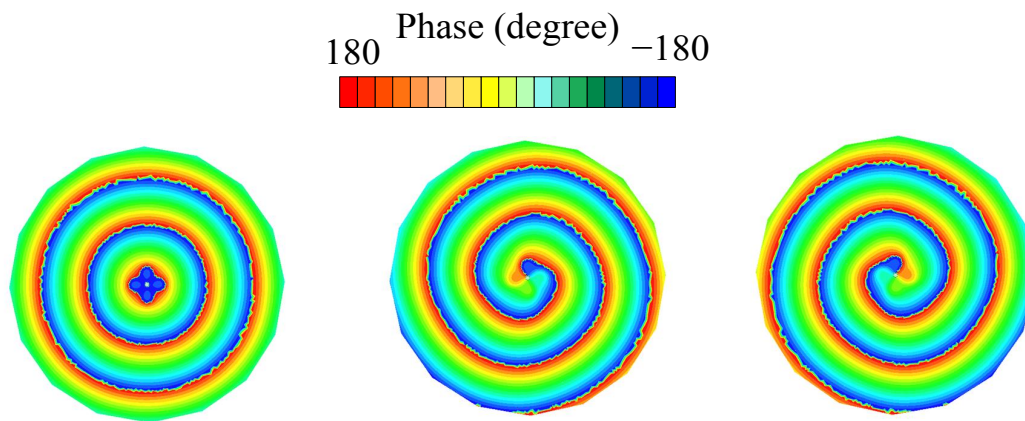


Fig. 4.9 Phase distribution of operation modes inside the PPW using open posts (from left to right are modes 0,  $-1$  and  $+1$ , respectively).

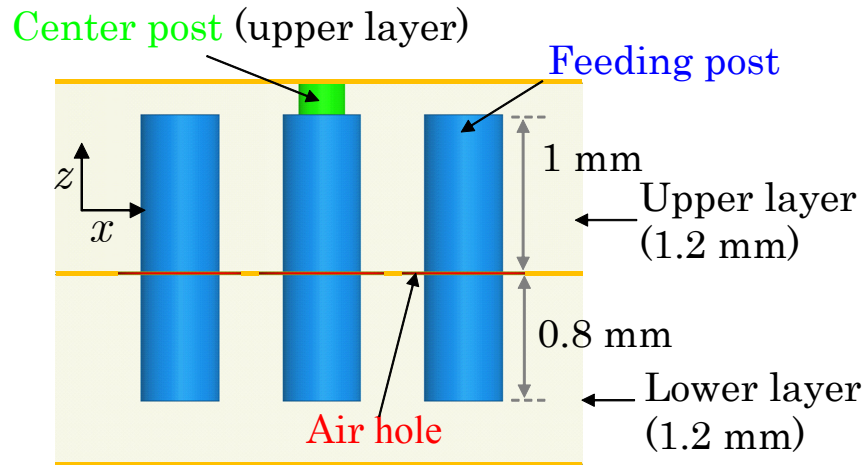


Fig 4.10 Cross section of the open posts.

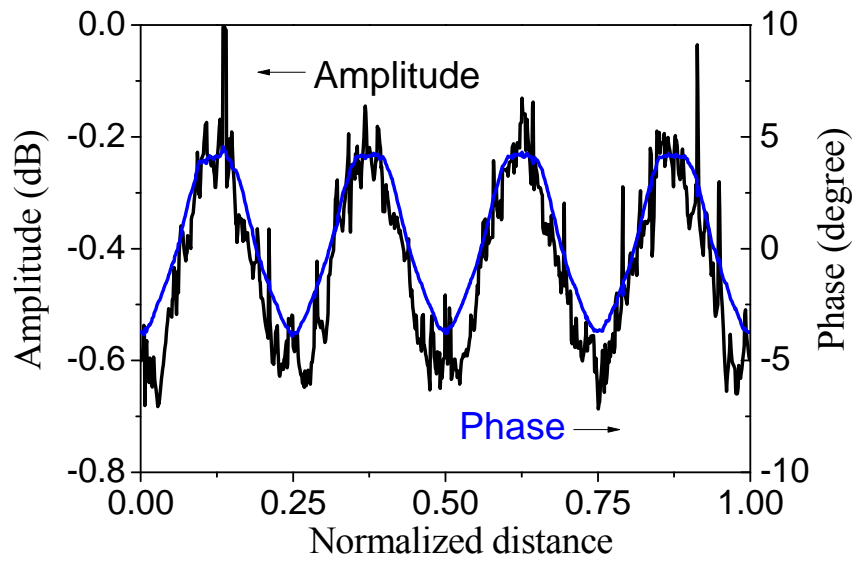
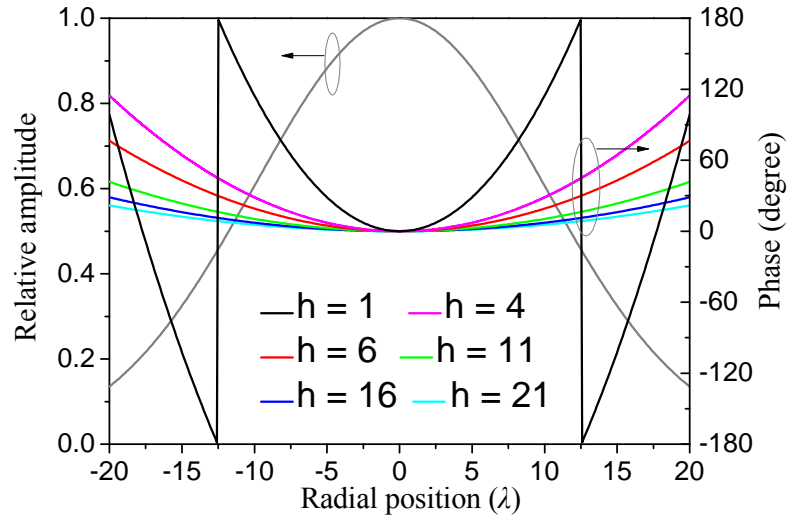
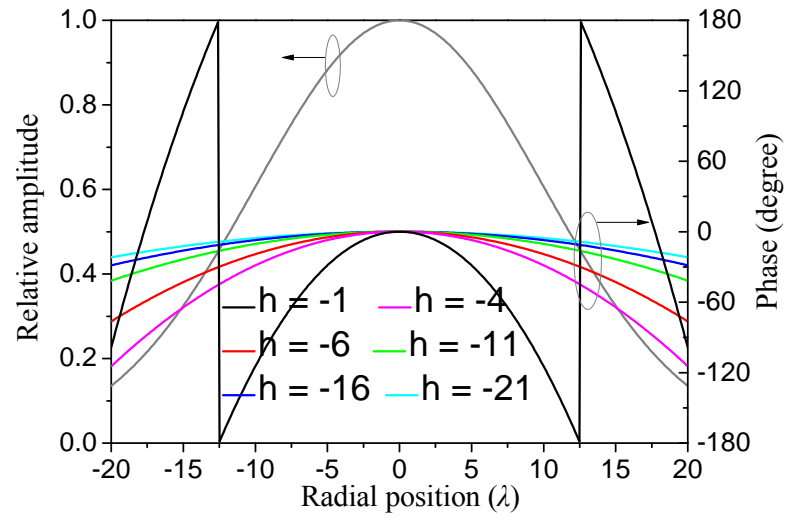


Fig. 4.11 Simulated circumferential field distribution of the mode 0 using open posts.



(a)



(b)

Fig. 4.12 Calculated aperture amplitude and phase distributions. (a) Convex lens. (b) Concave lens.



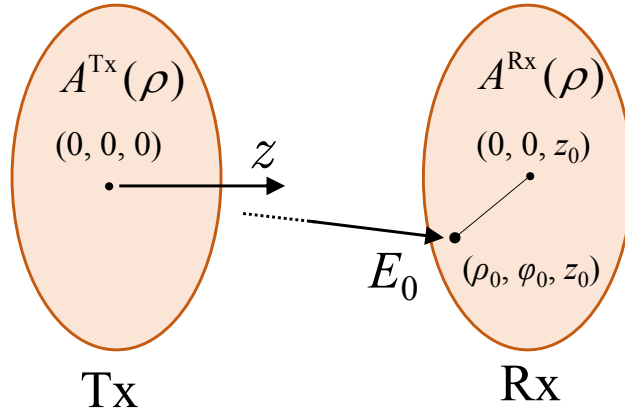
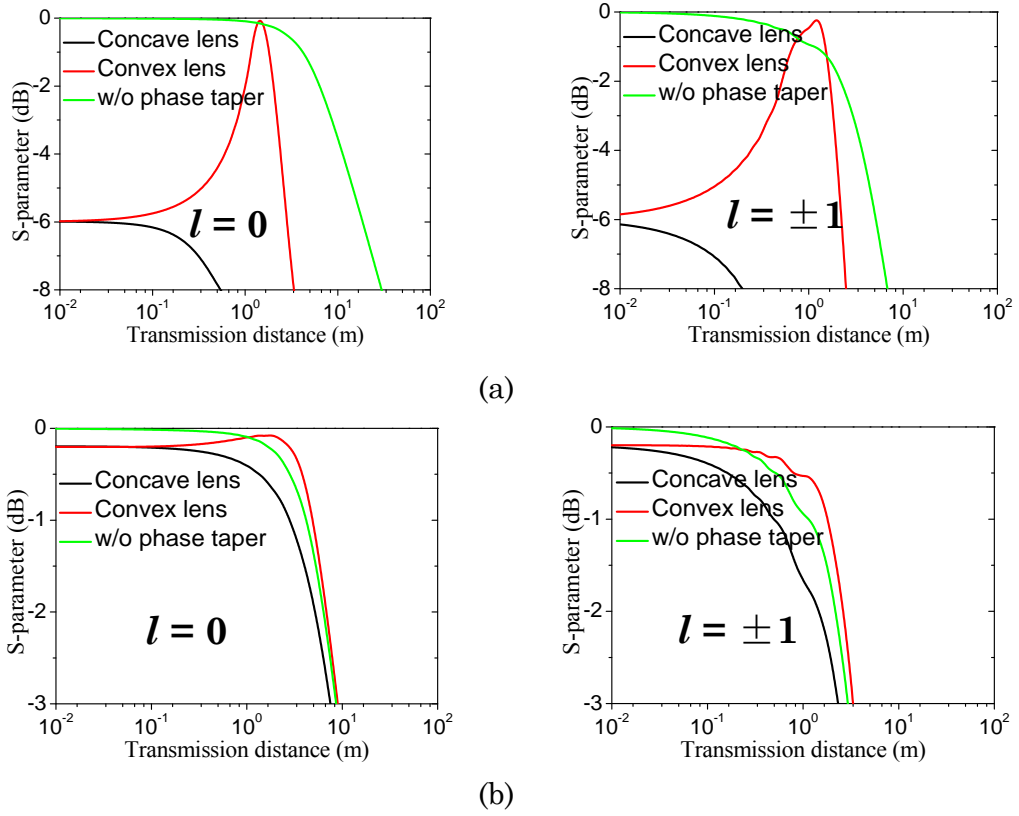
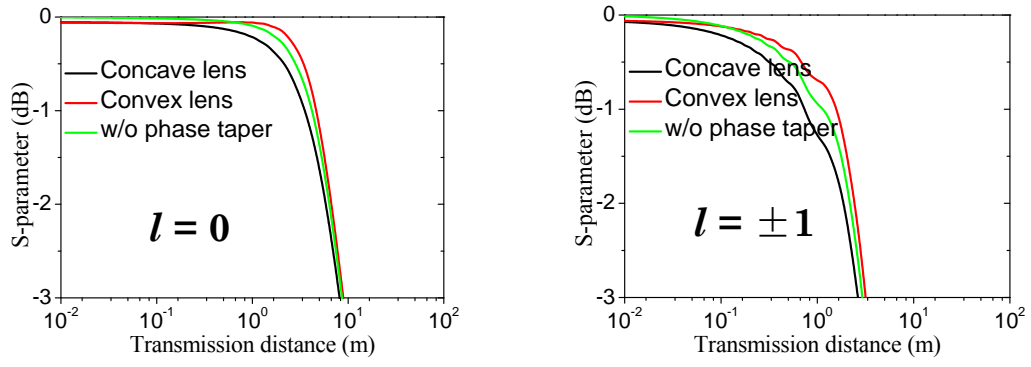


Fig. 4.13 Analysis model of the transmittance between Tx and Rx antennas in a cylindrical coordinate.





(c)

Fig. 4.14 Calculated transmittance for different  $h$  value under different OAM-mode states. (a)  $h = 1$ . (b)  $h = 11$ . (c)  $h = 21$ .

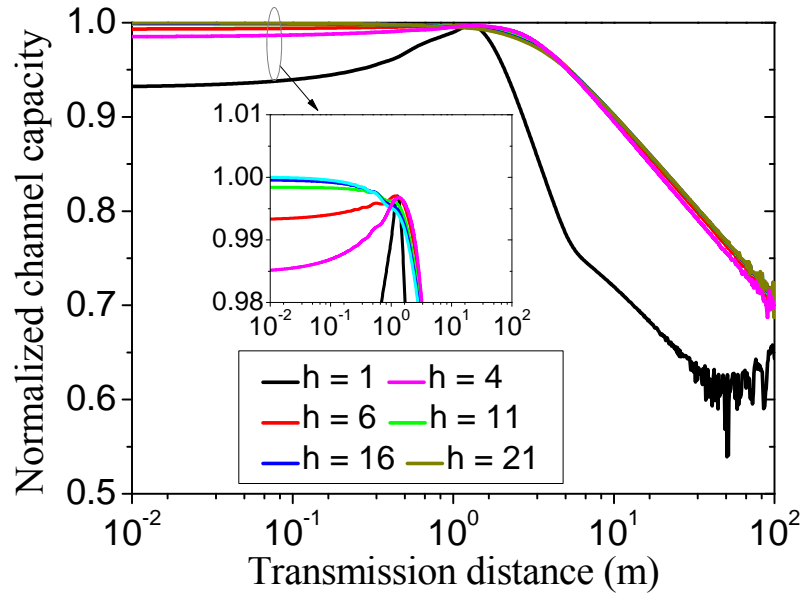
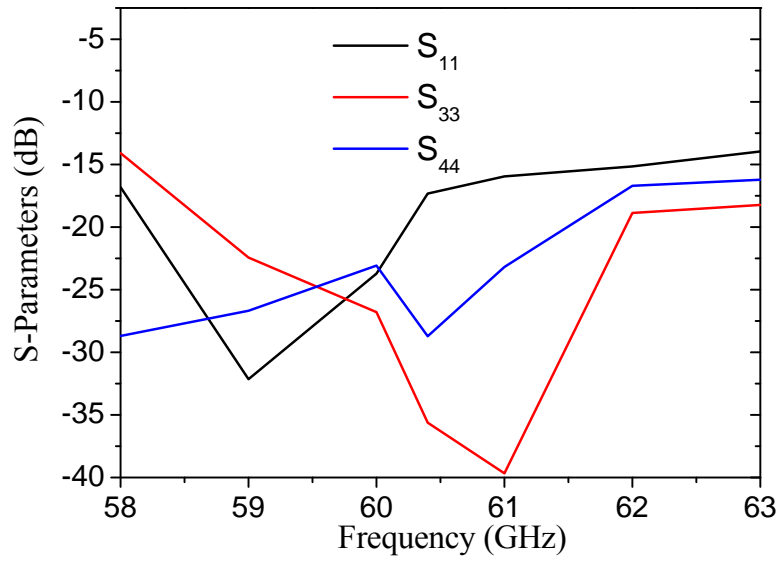
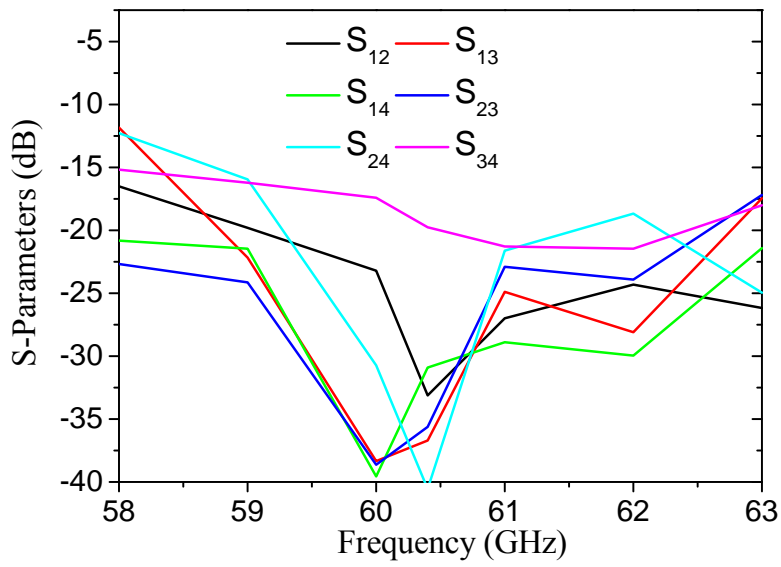


Fig. 4.15 Calculated channel capacity based on the aperture distribution using Gaussian amplitude taper and convex-lens phase taper.



(a)



(b)

Fig. 4.16 Simulated results of the full antenna structure. (a) Reflection. (b) Isolation.

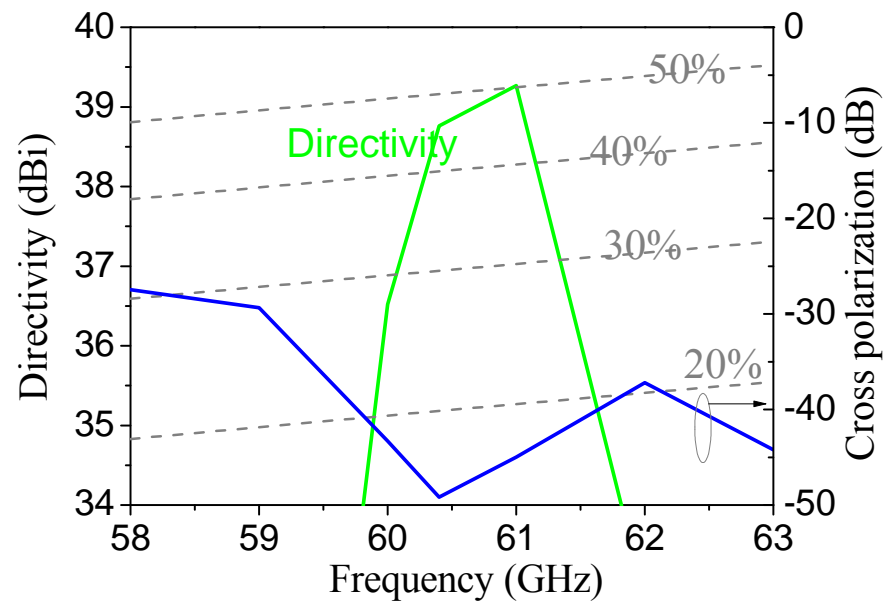


Fig. 4.17 Simulated directivity and cross-polarization of Port 1 in the bore-sight.

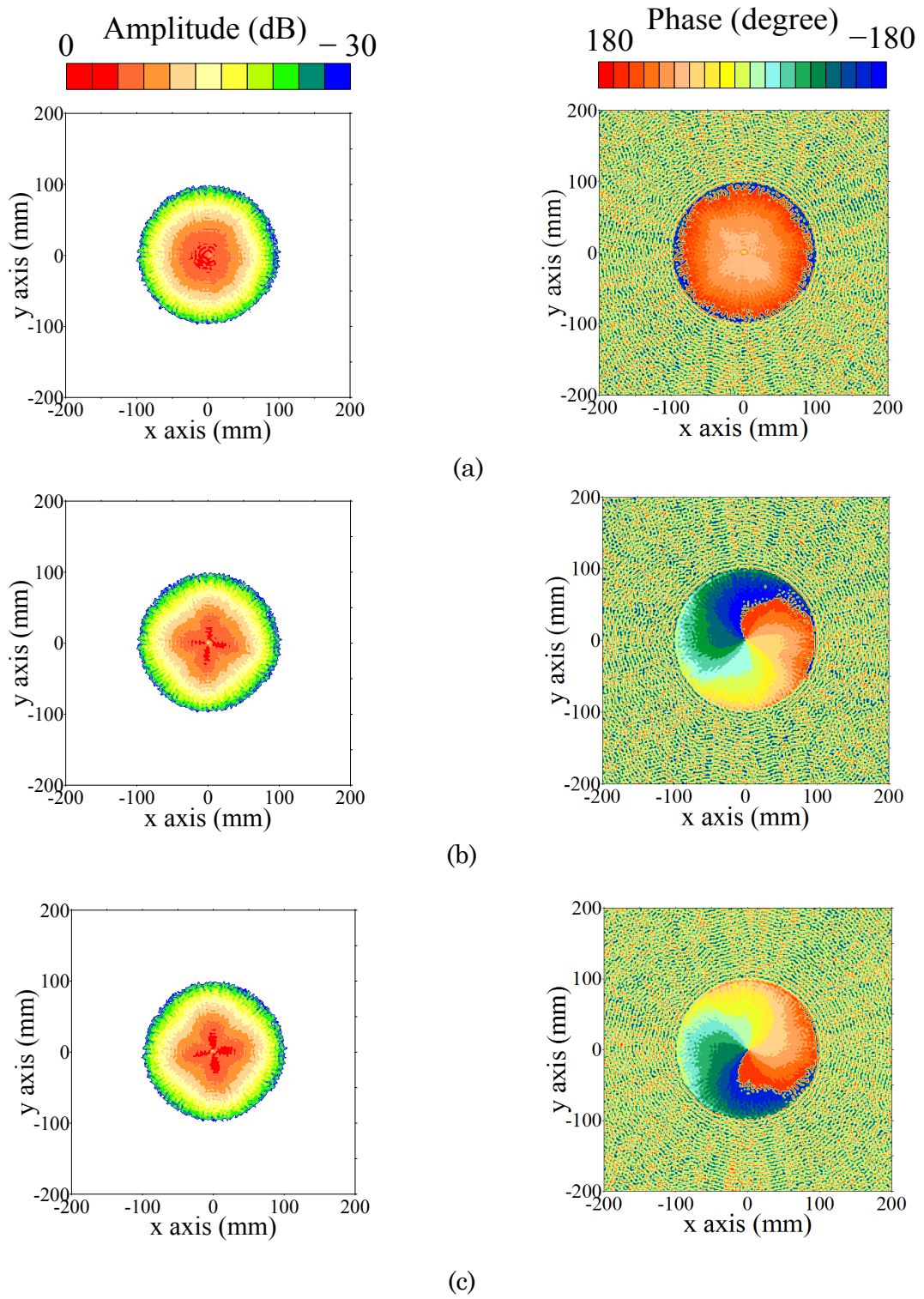


Fig. 4.18 Simulated E-field distribution on the antenna aperture at 60.4 GHz. (a) Port 1. (b) Port 3. (c) Port 4.

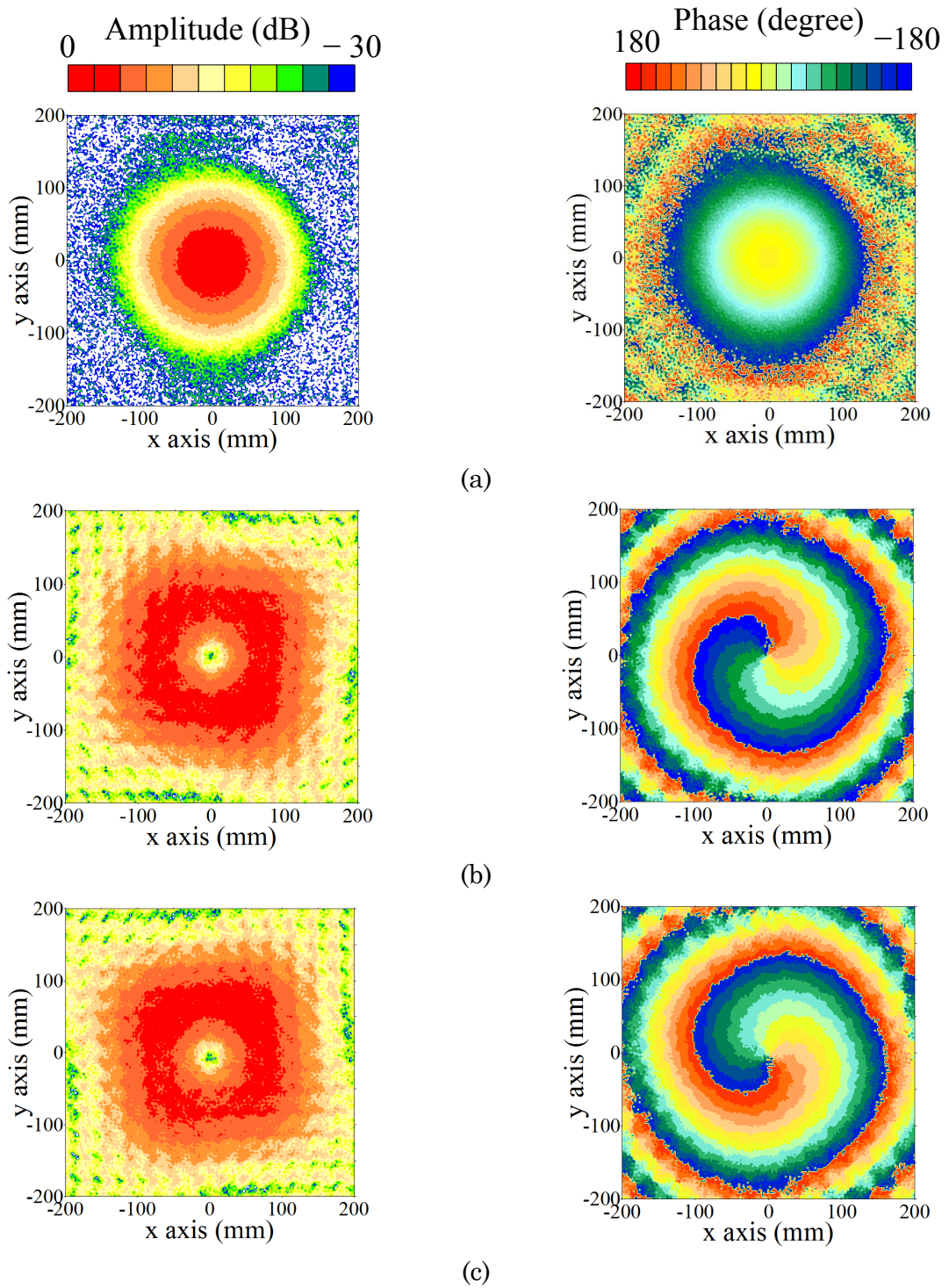


Fig. 4.19 Simulated E-field distribution on the reception plane at 60.4 GHz.  
(a) Port 1. (b) Port 3. (c) Port 4.

# Chapter 5    Conclusions

## 5.1    Summary of Preceding Chapters

To cope with this challenge in booming wireless applications that require Gbps and higher data speeds, this study makes efforts on the functional-circuit integration to waveguide slot array antennas in the millimeter-wave band. To be specific, the integration of filtering functionalities for E-band point-to-point communication, the incorporation of monopulse processing capability for E-band monopulse tracking, and the simultaneous generation of multiple orbital angular momentum (OAM) modes for V-band OAM-mode multiplexing, have been investigated. Different functional circuits associated with different integration scenarios have been studied. It has been verified that by properly designing the functional circuit and then optimally integrating with the feeding circuit, the antenna can work very well with specific functionality.

Chapter 1 reviews the application background and the state-of-the-art design techniques of waveguide slot array antennas for the millimeter-wave applications. It is shown that the traditional millimeter-wave waveguide antennas are mainly used for radiation without implementing any other functionality in their feeding networks. Consequently, the feasibility of integrating functional circuit to waveguide slot array antennas for different millimeter-wave wireless applications has been introduced.

Chapter 2 presents the plate-laminated waveguide filters in diffusion bonding technology for the first time and shows their uses in the integration with a corporate-feed slot array antenna for E-band ultra-high capacity point-to-point communications. First, a single cavity resonator model is studied and the measured high unloaded quality of 2121 at 79.07 GHz indicates its potential in the design of low-loss filters. Consequently, a sixth-order T-

shaped cavity bandpass filter that is comprised of ten cavity resonators is developed. It exhibits an insertion loss of 0.4 and 0.3 dB at 78.5 GHz at two output ports, a 3-dB fractional bandwidth of 20.5% as well as a small in-band amplitude/phase difference. Then, a fourth-order bandstop filter based on a band-rejection element is presented. It provides a high rejection level of 55 dB at 78.5 GHz, while an insertion loss of 0.44 and 0.28 dB at 73.5 and 83.5 GHz. The architectures of the proposed filters show attractive compatibility properties for integration. Finally, the proposed filters are fully integrated into a corporate-feed circuit of a  $16 \times 16$ -element slot array antenna without an interconnection circuit. With the seamless integration, the proposed building blocks demonstrate well-preserved high efficiency (only a low loss is introduced by the filters) and unchanged radiation characteristic (low side-lobe level, low cross polarization, and high directivity) in the designed passband, as well as specified band-stop performance.

Chapter 3 presents the design and characterization of an E-band  $16 \times 16$ -slot monopulse array antenna with full-corporate-feed fabricated by the diffusion bonding of laminated copper plates. The antenna is multi-layered, and consists of vertically-interconnected radiating elements, a corporate-feed circuit and a comparator. It has four input ports for different excitations. Sum and difference beams in different cut-planes for monopulse operation can be generated. The antenna has a quasi-planar profile, and a total size of  $13.31 \lambda_0 \times 13.31 \lambda_0 \times 1.52 \lambda_0$  ( $\lambda_0$  is the wavelength at the design frequency of 78.5 GHz). The antenna demonstrates a wide operation bandwidth of 17.2 (70–87.2) GHz for  $VSWR < 2$ . At 78.5 GHz: 1) for the sum beam, there is a 32.6-dBi realized gain (83% antenna efficiency) and a 33.3-dBi directivity (95% aperture efficiency); 2) for the difference beams in the E-, H-, 45°, and 135°-planes, the null depths are –53.0, –58.0, –57.8, and –65.6 dB, respectively. Across the full operation band where the sum main-beam and difference null are able to consistently point at the boresight, the antenna also demonstrates



excellent performance in terms of high gain, high efficiency, high isolation, low cross-polarization, and distinguished monopulse capability.

Chapter 4 presents the feasibility of simultaneously generating multiple OAM modes by using a radial line slot antenna (RLSA) which is fed by an OAM beam-switching circuit network. The OAM beam-switching circuit is placed at the lower layer and it is based on a post-wall waveguide structure. It has four input ports and it can launch different progressive phase states in the RLSA parallel plate waveguide. The RLSA is fed by the OAM beam-switching circuit through four open posts which are concentric to the RLSA center. Considering the application background of V-band non-far region communication, a Gaussian amplitude taper and a convex-lens phase taper have been applied on the antenna aperture. The effect of the aperture phase-taper on the channel capacity in OAM-mode multiplexing has also been investigated. The simulated results show that, at the design frequency, three OAM-modes are generated maintaining an acceptable rotational symmetry.

## 5.2 Future Prospects

In chapter 2, future work could include the integration of the proposed passive building blocks and the active circuits to realize the full E-band transceiver front-end module. This could concentrate on the design of high-performance transitions between the waveguide and planar transmission line associated with an optimal integration offering monolithic fabrication. It is also hoped that the success of this study in the filter design could justify continued investigation with more complex structures and functionalities (elliptic and self-equalized, and others) using diffusion bonding technology.

In chapter 3, the corporate-feed circuit and the comparator are arranged in different layers. Further work could include the one-body integration of the corporate-feed circuit and the comparator in order to reduce the thickness of the antenna.

In chapter 4, the antenna will be fabricated and measured to verify the design concept. Also, the OAM beam-switching circuit could be improved by reducing the amplitude and phase errors in a wider bandwidth.

# List of Publications

## 1. Journal Papers

- [1] X. Xu, M. Zhang, J. Hirokawa, and M. Ando, “E-band plate-laminated waveguide filters and their integration into a corporate-feed slot array antenna with diffusion bonding technology,” *IEEE Transactions on Microw. Theory and Techn.*, vol. 64, no. 11, pp. 3592–3603, Nov. 2016.
- [2] X. Xu, J. Hirokawa, and M. Ando “Plate-laminated waveguide monopulse slot array antenna with full-corporate-feed in the E-band,” *IEICE Trans. on Commun.*, vol. E100-B, no. 4, pp. 575–585, Apr. 2017.

## 2. International Conferences

- [1] X. Xu, J. Hirokawa, and M. Ando, “A Waveguide slot array antenna with integrated T-shaped filters in the corporate-feed circuit,” in *Proc. of International Symposium on Antennas and Propagation (ISAP)*, Session S3.1.2, pp.45-46, Hobart, Tasmania, Nov. 2015.
- [2] X. Xu, J. Hirokawa, and M. Ando, “Double-layered plate-laminated waveguide monopulse comparator in E-band,” in *IEEE International Symposium on Antennas and Propagation (APSURSI)*, Fajardo, Puerto Rico, pp. 1703–1704, June 2016.
- [3] X. Xu, J. Hirokawa, and M. Ando, “An E-band slotted waveguide monopulse array antenna with corporate-feed using diffusion bonding of laminated plates,” in *Proc. of International Symposium on Antennas and Propagation (ISAP)*, POS1-12, pp.308–309, Ginowan, Okinawa, Oct. 2016.
- [4] X. Xu, D. Mori, A. Mazzinghi, A. Freni, J. Hirokawa, M. Ando and K. Araki, “A 60-GHz RLSA fed by OAM beam-switching circuit carrying

three OAM modes,” in *IEEE International Symposium on Antennas and Propagation (APSURSI)*, San Diego, California, July 2017. (to appear)

### **3. Technical Reports on Antennas and Propagation, IEICE Japan**

- [1] X. Xu, J. Hirokawa, and M. Ando, “Design of a T-shaped bandpass filter integrating in the corporate-feed waveguide of a waveguide slot array antenna,” *IEICE Tech. Rep.*, vol. 115, no.12, AP2015-3, pp.9-12, Apr. 2015.
- [2] X. Xu, J. Hirokawa, and M. Ando, “A corporate-feed slotted waveguide monopulse array antenna covering the full E-band using diffusion bonding of laminated plate,” *IEICE Tech. Rep.*, vol. 116, no. 82, AP2016-34, pp. 13–16, June 2016.
- [3] X. Xu, J. Hirokawa, A. Mazzinghi and A. Freni, “Design of simultaneous generation of three OAM modes by using a RLSA fed by a waveguide circuit in the 60-GHz band,” *IEICE Tech. Rep.*, vol. 116, no. 82, AP2017-77, pp. 49–52, Aug. 2017.

### **4. National Convention Records of IEICE Japan**

- [1] X. Xu, J. Hirokawa, and M. Ando, “Integration of a T-shaped bandpass filter in a corporate-feed waveguide slot array antenna,” in *Proc. IEICE Gen. Conf.*, B-1-67, Kyoto, Mar. 2015.
- [2] X. Xu, J. Hirokawa, and M. Ando, “A double-layer waveguide monopulse comparator covering the 71–86 GHz Band,” in *Proc. IEICE Gen. Conf.*, B-1-53, Sendai, Sep. 2015.